Torsion Pendulum Searches for Macroscopic Spin-Interactions as a Window on New Physics

William A. Terrano

A dissertation
submitted in partial fulfillment of the
requirements for the degree of

Doctor of Philosophy

University of Washington

2015

Reading Committee:

Eric G. Adelberger, Chair

Blayne R. Heckel, Chair

David B. Kaplan

Program Authorized to Offer Degree:
Department of Physics

University of Washington

Abstract

Torsion Pendulum Searches for Macroscopic Spin-Interactions as a Window on New Physics

William A. Terrano

Co-Chairs of the Supervisory Committee:
Professor Eric G. Adelberger
Department of Physics

Professor Blayne R. Heckel
Department of Physics

The interactions of intrinsic particle spin offer a powerful window into important aspects of new physics, such as hidden high energy symmetries and CP-violation. This dissertation describes a new spin 20-pole torsion pendulum made with alternating high and low spin-density magnets. We operated the pendulum 4.1 mm from a spin source and 2.0 mm from a mass source, reaching the thermal noise level of the torsion fiber in all of our experiments. This allowed us to probe electron spin dipole-dipole and monopole-dipole interactions to greater sensitivities and over shorter distances than any previously test. We found no evidence of new interactions. Our monopole-dipole experiments set new constraints for exchange boson masses of $\sim$ 1- 500 μeV. Our dipole-dipole experiments set new constraints for all interaction lengths, down to 10^{-15} of electromagnetic strength at infinite range.

TABLE OF CONTENTS

LIST OF FIGURES

LIST OF TABLES

Chapter 1

THE PHYSICS OF EXOTIC SPIN-DEPENDENT INTERACTIONS

This thesis describes experiments that probed for macroscopic interactions coupled directly to the fundamental spin of the electron. Such interactions can take many forms, as enumerated by Dobrescu and Mocioui [1]. In this work we focus on the monopole-dipole (Eq. 1.1) and dipole-dipole (Eq. 1.2) interactions.

$$V_{\vec{\sigma}\cdot\vec{r}} = \frac{\hbar g_{\rm s} g_{\rm p}}{8\pi m_{\rm e} c}\left[(\hat{\boldsymbol{\sigma}}\cdot\hat{\boldsymbol{r}})\left(\frac{1}{r\lambda}+\frac{1}{r^2}\right)\right]e^{-r/\lambda}\ . \tag{1.1}$$

$$\begin{aligned} V_{dd} = \ & - \ \frac{g_{\rm p}^2\hbar^2}{16\pi m_{\rm e}^2 c^2 r^3}\left[(\hat{\boldsymbol{\sigma_1}}\cdot\hat{\boldsymbol{\sigma_2}})\left(1+\frac{r}{\lambda}\right)\right. \\ & - \ \left.(\hat{\boldsymbol{\sigma_1}}\cdot\hat{\boldsymbol{r}})(\hat{\boldsymbol{\sigma_2}}\cdot\hat{\boldsymbol{r}})\left(3+\frac{3r}{\lambda}+\frac{r^2}{\lambda^2}\right)\right]e^{-r/\lambda}\ ; \end{aligned} \tag{1.2}$$

where $g_{\rm s}$ is the monopole coupling strength, $g_{\rm p}$ is the dipole coupling strength and λ is the Yukawa range of the interaction, with $\lambda = \hbar/(m_{\rm b}c)$ when $m_{\rm b}$ is the mass of the exchange boson mediating the interaction. Of all the possible spin-interactions, these are particularly interesting because the monopole-dipole interaction is sensitive to new sources of CP-violation and the dipole-dipole interaction can be the signature of a hidden high-energy symmetry.

1.1 The Monopole-Dipole Interaction and CP-violation

CP-symmetry lies at the heart of one of the outstanding mysteries in science, the fact that we live in a universe dominated by matter. Consisting of charge-conjugation, C, and parity-inversion, P, a combined CP-transformation connects a particle with the mirror-image of its anti-particle. Sakharov [2] showed that the laws of physics must violate CP-symmetry in

order to distinguish baryons from anti-baryons in the early universe and produce the baryon dominated universe we live in.

$K^\circ - \bar{K}^\circ$ oscillation [3], Kaon decay [4],[5] and B-meson decay [6],[7] all exhibit CP-violation. The electroweak quark-mixing matrix fully describes these observations, providing a single explanation for all the known cases of CP-violation. This is inadequate for the purposes of baryogenesis, however, as no current model can produce the observed baryon to photon ratio using only the CP-violation contained in the quark mixing matrix.

Identifying additional sources of CP-violation remains the focus of intense experimental efforts. Traditional accelerator based searches for CP-violation are extending to higher energies at the Large Hadron Collider [8],[9] and greater precision at dedicated B-factories [10]. A large variety of electric-dipole-moment searches [11],[12],[13] have achieved fantastic sensitivities to CP-violating processes. Up to this point, no experiment has found evidence for beyond-the-standard-model CP-violation.

This motivates us to search for other, less well-tested, sources of CP-violation. We do this by identifying and probing macroscopic interactions that are inherently CP-violating. Any interaction that violates time-reversal symmetry, T, also violates CP-symmetry by the CPT theorem that states that all physical laws must be invariant under a combined CPT inversion. Position vectors, $\hat{r}$, change sign under parity-inversion. Spins $\hat{\sigma}$ are angular momenta and so are invariant under parity-inversion, P, but change sign time-reversal, T. The product $\hat{\boldsymbol{\sigma}} \cdot \hat{\boldsymbol{r}}$ is therefor odd under parity and time-reversal and the monopole-dipole interaction given in Eq. 1.1 is T and CP-violating. The existence of a monopole-dipole interaction would be evidence of a new CP-violating exchange boson.

1.2 The Dipole-Dipole Interaction as a Probe of High-Energy Symmetries

The study of symmetries has been essential to our understanding of the physical world whether it be Maxwell completing the classical laws of electromagnetism or Noether's theorem identifying conserved quantities with the symmetries of a system. Identifying hidden symmetries has been just as important, for instance the hidden SU(2) and SU(3) symmetries of the standard model. Hidden symmetries are symmetries of the system or theory that are not readily apparent in the particular configuration that the system adopts. Nambu

and Goldstone demonstrated that hidden symmetries, also known as spontaneously broken symmetries, must give rise to new massless, pseudoscalar bosons called Nambu-Goldstone bosons. If the broken symmetry is not exact, the Nambu-Goldstone bosons are not massless and are typically called pseudo-Goldstone bosons. The exchange of a pseudoscalar boson between two fermions mediates a dipole-dipole interaction of the form of Eq. 1.2, so as long as the new pseudo-Goldstone boson couples to standard model fermions and is light enough it will mediate a new macroscopic spin-coupled force. The pions and the meson octet are the pseudo-Goldstone bosons of the broken SU(2) and SU(3) symmetries of the standard model, respectively.

1.2.1 Nambu-Goldstone Boson Couplings

In the case of a hidden, exact, symmetry, the Nambu-Goldstone boson interactions must preserve the symmetry to which they are related. The Hamiltonian describing the behavior of the Nambu-Goldstone boson must therefore be invariant under the transformation of the Nambu-Goldstone field $\phi \rightarrow \phi + a$, so only derivatives of ϕ can appear in the Hamiltonian. This disallows mass terms, $\frac{1}{2}m^2\phi^2$, and scalar Yukawa interactions, $\phi\bar{\psi}\psi$ where ψ is a standard-model fermion that might serve to probe for ϕ. The lowest dimension interactions permitted by the symmetry that connect the Nambu-Goldstone bosons with observable standard-model particles are:

$$\frac{\partial_\mu}{F}\phi\bar{\psi}\gamma^\mu\psi \tag{1.3}$$

$$\frac{\partial_\mu}{F}\phi\bar{\psi}\gamma^\mu\gamma_5\psi \tag{1.4}$$

where F is the scale at which the spontaneous symmetry breaking occurs.

Integrating these equations by parts gives:

$$\phi\frac{\partial_\mu}{F}\bar{\psi}\gamma^\mu\psi \tag{1.5}$$

$$\phi\frac{\partial_\mu}{F}\bar{\psi}\gamma^\mu\gamma_5\psi \tag{1.6}$$

The interaction in Eq. 1.5 vanishes as it is the derivative of the ψ current, which is conserved. This leaves Eq. 1.6 as the lowest dimension operator coupling the new Nambu-Goldstone boson with the observable universe. Applying Dirac's equation $(i\gamma^\mu\partial_\mu - m_\psi)\psi = 0$

to Eq. 1.6 allows us to rewrite it in the form of a standard pseudoscalar Yukawa interaction

$$\phi \frac{m_\psi}{F} \bar{\psi} \gamma^\mu \gamma_5 \psi \tag{1.7}$$

with the pseudoscalar coupling constant $g_{\rm p} = \dfrac{m_\psi}{F}$ determined by the mass of the probe fermion and the symmetry breaking scale. Clearly, when looking for symmetries broken at very high energy scales, we must probe for very weak dipole-dipole interactions.

1.2.2 Pseudo-Goldstone Boson Mass

If the theory also contains terms explicitly breaking the hidden symmetry, the coupling strength in Eq. 1.7 is still valid but the Nambu-Goldstone boson acquires a mass. If the explicit symmetry breaking scale of the effective Lagrangian is Λ, the the mass of the pseudo-Goldstone is [14]

$$m_{\rm p} = \frac{\Lambda^2}{F}$$

so that high symmetry breaking scales F tend to produce lighter Goldstone bosons.

1.2.3 Conjectured Pseudo-Goldstone Bosons

Ringwald [15] gives a nice review of conjectured symmetries and their associated Nambu-Goldstone, as well as other mechanisms for producing light pseudo-scalar bosons, sometimes referred to as axions or axion-like-particles. Examples that have attracted theoretical attention include:

- *Axions*, $A(x)$ are Nambu-Goldstone bosons that couple to the CP-violating component of the QCD gluon fields $\dfrac{\alpha_s}{8\pi} G_{\mu\nu} \tilde{G}^{\mu\nu}$. This term replaces the QCD theta parameter $\theta_{\rm QCD}$ with the dynamical quantity $A(x)/f_{\rm A}$ which drives the strong CP-violation parameter to 0 and explains why there is no observed CP-violation in QCD despite instanton effects that produce exactly this CP-violating term.

- *Majorons* are the Nambu-Goldstone bosons produced by the breaking of global lepton number symmetry at a high energy scale $f_{\rm L}$. A see-saw mechanism between the heavy

Majorana-type mass $M_{\rm M} = xf_{\rm L}$ and the typical electroweak scale, $f_{\rm W}$, of the Dirac-type mass $M_{\rm D} = yf_{\rm W}$ can then naturally produce the small observed masses of the standard model active neutrinos.

- *Familons* are the Nambu-Goldstone bosons arising from the breaking of global family symmetry.

- *Closed string axions* are modes predicted by string theory. The number $n_{\rm ax}$ depends on the topology of the compactified manifold.

- *Accidental pseudo-Goldstone Bosons* are the Nambu-Goldstone bosons arising from the breaking of accidental $U(1)$ symmetries that are the low energy remnants of exact discrete symmetries.

By probing directly for a pseudo-Goldstone boson we are not looking at the properties of any specific symmetry but rather a general feature of all hidden symmetries. Thus searches for a new dipole-dipole interaction are sensitive to generic hidden symmetries, including ones that have not been considered, as long as they couple to the relevant fermion.

1.2.4 Nambu-Goldstone Bosons and Cold Dark Matter

Pseudo-Goldstone bosons are also interesting because they make very good cold dark matter candidates [16]. Vacuum realignment mechanisms and the decay of topological defects can produce them in great numbers in the early universe with very small coupling constants and low masses that make them cold and very long lived.

1.3 The Dipole-Dipole Interaction and Extensions of General Relativity

The theory of general relativity describes gravity as an effect of the curvature of space-time. Shortly after the development of general relativity, Levi-Civita [17] discovered that a complete description of curved space-time requires not only a curvature tensor but also a torsion tensor, defined as the anti-symmetric component of the familiar affine connection.

Since that time several lines of argument suggest that the torsion term should exist in general relativity and couple to the intrinsic spin of particles. These arguments generally revolve around making general relativity more compatible with quantum theories.

- *Angular Momentum Conservation* – Without torsion, general relativity does not conserve total angular momentum. Instead it conserves only orbital angular momentum, as spin does not exist in the theory [18]

- *Poincaré invariance* – To make general relativity Poincaré invariant (Lorentz invariant and translationally invariant), it must include a torsion term [19]

- *String theory* – To have a consistent string theory, there must be three fields [17]: a scalar field, gravity and the Kalb-Ramond field [20]. The Kalb-Ramond field turns out to be a torsion field [21].

The symmetry properties of torsion and spin mean that a torsion field produces an infinite-range, dipole-dipole interaction between the spins of two particles just like Eq. 1.2, with all of the Yukawa factors equal to one [17].

1.4 Spin-Interactions in Astrophysics

New spin-interactions can also have astrophysical impacts. The most prominent is as an additional cooling mechanism for hot plasmas such as stars and supernovas. Stellar plasmas can emit pseudoscalars through the Compton process $\gamma + e \rightarrow e + \phi$, bremsstrahlung $e + Z\,e \rightarrow Z\,e + e + \phi$, atomic recombination and dissociation $e + Z \rightarrow (e, Z) + \phi$, and pair annihilation $e^+ + e^- \rightarrow \gamma + \phi$ [22]. For these processes to cool the plasma, the plasma must have enough energy to produce the new bosons and the bosons must be able to escape the plasma. Roughly speaking, this means that the kinetic energy of the fermions that radiate the new bosons must be larger than the mass of the new boson, so the temperature of the plasma must be few $\times\, T_\psi \gtrsim m_{\rm b}$, and the coupling strengths of the bosons must be less than that of the photons $g_{\rm p}^2/4\pi = \alpha_{\rm p} \lesssim \alpha$ so they can transport energy through the plasma. The coupling strength can not be too weak either, or the effect of the boson emission on the cooling rates

would be imperceptible to us. The constraints on new pseudo-Goldstone bosons from these considerations follow.

- *Solar cooling* – For the sun, the pseudoscalar luminosity is $L_{\rm p} = \alpha_{\rm p}\, 6.0 \times 10^{21} L_{\odot}$ [22].
  - Since the sun is halfway through it's life cycle, $L_{\rm p}$ can not be much larger than $L_{\odot}$, so conservatively we find $\alpha_{\rm p} \lesssim 1.5 \cdot 10^{-22}$ or $g_{\rm p}^2 \lesssim 2 \cdot 10^{-21}$. This corresponds to a symmetry breaking scale $F \gtrsim 10^7$ GeV.
  - In order to match helioseismology sound-speed profiles [23] a new energy loss channel should not exceed 20% of $L_{\odot}$ implying $\alpha_{\rm p} \lesssim 3 \cdot 10^{-23}$ or $g_{\rm p}^2 \lesssim 4 \cdot 10^{-22}$ and $F \gtrsim 2.5 \cdot 10^7$ GeV, although helioseismology models currently disagree with observed solar metallicities [24].

- *Stellar cooling* Avoiding excessive cooling of white dwarf stars and delayed ignition of helium burning in globular clusters suggests $\alpha_{\rm p} \lesssim 1 \cdot 10^{-26}$ or $g_{\rm p}^2 \lesssim 1 \cdot 10^{-25}$ and $F \gtrsim 10^9$ GeV [22], although the systematics involved in such arguments are completely unknown. In fact, the fits to white dwarf cooling times and luminosity functions improve assuming a coupling of $g_{\rm p}^2 \sim 1 \cdot 10^{-26}$ [25].

- *Helioscopes* Attempts to directly detect pseudo-Goldstone bosons produced in the sun achieve sensitivities corresponding to $F \gtrsim 10^7$ GeV.

All of these techniques, which involve looking for pseudo-Goldstone bosons produced in hot, dense plasmas, yield very tight constraints. However a number of models have been proposed in which the conditions found in astrophysical plasmas greatly suppress the production of the pseudo-Goldstone bosons [26],[27],[28],[29],[30]. In this case laboratory experiments such as the one described in this thesis provide the best constraints.

Chapter 2

TECHNIQUE FOR PROBING SHORT-RANGE SPIN-DEPENDENT INTERACTIONS

2.1 General Principles of our Spin Experiments

Searches for monopole-dipole and dipole-dipole interactions require spin-polarized test bodies because their effects are highly suppressed in traditional fifth-force searches using unpolarized materials. The difficulty is that spin-polarized particles also source magnetic fields that would constitute an enormous background. A number of experimental strategies have been exploited to suppress this background.

Sensitive tests for exotic spin-coupled interactions between protons date to 1979, when Ramsey [31] compared his measurements of H_2 rotational and vibrational states to the theoretically predicated values and constrained new proton-proton tensor interactions, which would modify the spectrum.

The most sensitive search for an exotic spin-coupled interaction between neutrons used optically pumped ^{3}He as the source of polarized neutrons and the polarization of the potassium electrons in a ^{3}He-K co-magnetometer as the detector[32]. The bias field applied to the co-magnetometer exactly canceled the magnetic field of the polarized ^{3}He nuclear spins on the potassium electrons. In this configuration, the ^{3}He spins adiabatically followed small changes in the external magnetic field so the potassium electrons experienced no magnetic fields that could rotate their polarizations. A non-magnetic interaction between the ^{3}He spins in the co-magnetometer and the polarized neutron source would change the relative orientations of the ^{3}He spins and the magnetic field and rotate the measured polarization orientation of the potassium electrons.

This thesis describes experiments searching for new spin-coupled interactions involving electrons. In 1991, Wineland [33] measured one of the hyperfine transitions^{9}Be$^+$ ions in the presence of a magnetic field. To constrain non-magnetic spin interactions they compared

the transition frequency when electron spins sourced the magnetic field to the transition frequency when the currents in a super-conducting solenoid sourced the magnetic field. Other experiments have looked for an induced spin-polarization in a sample that is separated from a permanent magnet by superconducting shields. The superconducting shields block magnetic fields but have no effect on spin fields. The most sensitive such test, performed by Chui and Ni in 1993[34], used a paramagnetic salt (terbium flouride) as the detector.

We use torsion pendulums with spin-polarized components that will experience a torque in the presence of new spin-interactions. We eliminated the external magnetic field by assembling the pendulums from closed magnetic loops. If the closed magnetic loop consisted of only a single material, the spins would also form a closed loop. Both spin-dependent interactions V_{dd} and $V_{\vec{\sigma}\cdot\vec{r}}$ couple derivatively and must vanish for closed loops of spin, as shown in explicitly in Eq. 2.7 and the discussion that follows it. Fortunately, magnetic materials vary in the fraction of their total magnetization produced by spin-polarized electrons, a ratio known as the spin fraction. By constructing the closed magnetic loops from two magnetic materials with different spin fractions and but equal magnetizations, we can produce pendulums and attractors with large spin-contrasts and extremely small external magnetic fields.

2.2 Description of the Short-Range Spin Experiments

Our instrument combined the previously developed Eot-Wash group technique [35] for making high spin-density assemblies having extraordinarily low external magnetic field with the high-multipole, planar geometry pendulum and rotating attractor pioneered in the Eot-Wash probes of short-range gravity [36].

The key element of our instrument, shown in Fig. 3.1, was a spin-ring containing alternating segments of high and low spin density materials inside of a μ-metal magnetic shield. This formed a spin 20-pole with a negligible external magnetic field. One such spin-ring was the active element of a torsion pendulum (Sec. 3.2.1) positioned just above a rotating attractor. Figure 2.1 shows a photograph of a spin-ring. A virtually hermetic magnetic shield enclosed the entire pendulum and minimized residual magnetic couplings to the pendulum. We probed for dipole-dipole interactions (V_{dd}, Eq. 1.2) using an attractor consisting of a

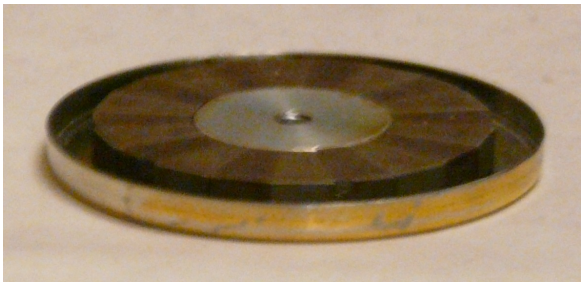

Figure 2.1: A photograph of our prototype spin ring, sitting in the bottom half of a μ-metal can used as a magnetic shield.

second 20-pole spin-ring similar to the one in the pendulum. Thin metal shims above and below each magnet segment largely canceled the gravitational 20-pole of the attractor spin-ring generated by the difference in mass densities of the high and low spin density materials (Sec. 3.2.3). We probed for monopole-dipole interactions ($V_{\vec{\sigma}\cdot\vec{r}}$, Eq. 1.1) and characterized the gravitational backgrounds in our dipole-dipole work by replacing the spin-ring attractor with a gravity-ring (Sec. 3.2.4) of the same dimensions that had no spin but a 20-pole mass distribution. The pendulum and attractors each contained 4 tungsten rods that provided a continuous gravitational calibration signal.

We inferred the torque, τ, applied to the pendulum by the rotating attractor by decomposing the pendulum's twist angle, $\theta = \tau/\kappa$, into components that varied harmonically at frequencies $n\omega$ where ω was the attractor rotation frequency. The calibration signal occurred at 4ω, while a signal due to a new spin interaction would appear at 10ω. Placing our science signal at a high harmonic of the attractor rotation rate eliminated systematics that did not occur at exactly that frequency, or change when we varied the attractor rotation rate. This included systematics involving lab-fixed or slowly varying torques as well as the large and challenging class of systematics produced by the attraction rotation system, which primarily appear at 1ω and 2ω. Taking data at multiple pendulum-attractor separations validated that the instrument and our major systematics behaved as expected.

2.3 High and Low Spin Density Materials

We used a ferromagnet, Alnico, for the high spin-density segments and a rare-earth magnet, $SmCo_5$, for the low spin-density segments. The magnetization of Alnico comes almost entirely from aligned electron spins and has an estimated spin fraction of 0.95 [37](pp 30-45), [38](Appendix A). $SmCo_5$ has roughly equal spin and orbital contributions to its magnetic moment that combine to an estimated spin fraction of 0.5 ± 0.1 [37](pp 30-45), [38](Appendix A). The total magnetic moment of the samarium ion is very small because its orbital and spin components nearly cancel so that the ferromagnetic cobalt lattice generates essentially the entire magnetization of the material. Each of the five cobalt atoms has two spins for a total $S = 10\hbar/2$. The samarium 3^+ ion has a large spin moment, $S = 5\hbar/2$, directed opposite to its large orbital moment $L = 5\hbar$ and the spin moment of the cobalt lattice, so the spins of the samarium ions cancel about half the spin moment of the cobalt lattice while having almost no effect on the magnetization of the material.

It is the spin-density difference between Alnico and $SmCo_5$ that converts new spin-interactions into torques on our pendulum. Previous experiments with an Eot-Wash spin-dipole pendulum directly measured the Alnico-$SmCo_5$ spin-density difference [37](pg. 80), [38]. The pendulum used in that experiment had a net angular momentum $\vec{J} = \vec{L} + \vec{S}$ which experienced a torque in the lab frame due to the Coriolis effect of the earth's rotation. Since the pendulum had no net magnetic moment and the spin g-factor is very nearly equal to 2, $\vec{M} = \vec{L} - 2\vec{S} = 0$ and the angular momentum on the pendulum was equal to and opposite the spin moment of the pendulum $\vec{J} = -\vec{S}$. Thus the size of the observed "gyrocompass" torque corresponds directly to the total number of aligned spins on the pendulum $N_p = (9.78 \pm 0.26) \times 10^{22}$. The spin-dipole pendulum contained equal volumes of Alnico and $SmCo_5$ magnetized to the same degree and oriented in opposite directions so $N_p = N_{Alnico} - N_{SmCo}$. We can convert this back to a spin fraction difference $r_{Alnico} - r_{SmCo} = 0.44 \pm .01$ using the formula for the spin-density of a material $\rho_s = \dfrac{r_\mathrm{s} \cdot M}{4\pi\mu_\mathrm{B}}$ where ρ_s is the spin-density of the magnet, r_s is the spin fraction of the magnet, M is the magnetization of the magnet and $\mu_\mathrm{B} = 9.27 \times 10^{-21}$ ergs/G is the Bohr magneton in Gaussian. Claire Cramer determined the $SmCo_5$ magnetization, $M = 9.6 \pm 0.02 \times 10^3$ G,

by passing a stack of $SmCo_5$ magnets through an induction coil [37](pg. 29). Combining everything, and taking into account the factor of 0.65 for the octagonal shape of the magnet pucks[38], these results give the spin-density difference between Alnico and $SmCo_5$ at this magnetization to be $\Delta\rho_s = 3.61 \pm 0.08 \times 10^{22}\,\mathrm{spins/cm^3}$ with cgs base units substituted in place of Gauss, $\mathrm{G} \equiv \mathrm{g}^{1/2}\ \mathrm{cm}^{-1/2}\ \mathrm{s}^{-1}$. This agrees with rough numbers extracted from fits to scattering experiments [37](pp 30-45), [38](Appendix A), but is a more reliable and directly relevant result.

2.4 Does Magnetic Shielding Screen the New Spin-Interactions?

We make extensive use of high permeability material, called μ-metal, to attenuate magnetic effects in our experiments due to the small, $\mathcal{O}(10\,\mathrm{G})$, leakage fields from our spin-rings with $\mathcal{O}(10^4\,\mathrm{G})$ internal fields. The high permeability means that the electron spins in the shields easily change orientation to cancel magnetic fields. A new spin-interaction will also, to some degree, align the electron spins in the μ-metal and shield the new spin-interaction. This effect is negligible in our experiments because we are looking for interactions with couplings to electron spin 5-7 orders of magnitude less than the magnetic coupling. The spin-field will therefore be 5-7 orders of magnitude less effective than a magnetic field at aligning the spins in the μ-metal , and the effective "spin permeability" of the material is 5-7 orders of magnitude less than its magnetic permeability. The typical magnetic permeability of μ-metal is $\mathcal{O}(5 \cdot 10^5)$ so its "spin permeability" is $\mathcal{O}(1)$ or less. The permeability of free space is 1, so μ-metal material does not does not attenuate the hypothesized, weakly-coupled, spin-field.

2.5 Fourier-Bessel Calculations of Short-Range Signals from Gravitational and Spin Interactions

Standard expansions in spherical harmonics do not converge for planar, high-multipolarity geometries in close proximity. To efficiently calculate the torques in these experiments we used an expansion suggested to us by George Bertsch.

The heart of all of our calculations of the expected torque is a cylindrical separation of variables we call the Fourier-Bessel expansion. We can separate the Yukawa potential in

cylindrical coordinates $\vec{r} = (r, \theta, z)$ where the z axis is vertical:

$$G(\vec{r}, \vec{r}') = \frac{e^{-\mu|\vec{r}-\vec{r}'|}}{4\pi\,|\vec{r}-\vec{r}'|} = \frac{1}{4\pi}\sum_{l=-\infty}^{\infty} e^{il(\theta-\theta')}\int_0^\infty \mathrm{d}k\ k\ J_l(kr)\,J_l\big(kr'\big)\,\frac{e^{-\sqrt{k^2+\mu^2}(z_>-z_<)}}{\sqrt{k^2+\mu^2}}. \quad (2.1)$$

The energy is the integral of Eq. 2.1 over the source densities of the attractor and pendulum, labeled $n_1(\vec{r})$ and $n_2(\vec{r})$ respectively. Since the attractor is entirely below the pendulum, we can identify $z_> = z_2$ and $z_< = z_1$ and separate the energy integral into portions that depend only on the attractor and only on the pendulum ($I_{1,l}$ and $I_{2,l}$ respectively):

$$U = -\frac{g_1 g_2}{4\pi}\sum_{l=-\infty}^{\infty}\int_0^\infty \frac{\mathrm{d}k\ k}{\sqrt{k^2+\mu^2}}\ I_{1,l}\ I_{2,l} \quad (2.2)$$

$$\begin{aligned} I_{1,l} &= \int \mathrm{d}^3 r\ n_1(\vec{r})\ e^{-il\theta}\,J_l(kr)\ e^{+\sqrt{k^2+\mu^2}z} \\ I_{2,l} &= \int \mathrm{d}^3 r\ n_2(\vec{r})\ e^{+il\theta}\,J_l(kr)\ e^{-\sqrt{k^2+\mu^2}z} \end{aligned} \quad (2.3)$$

This expansion has a nearly analytic solution, as detailed in [39], allowing rapid calculations of the Newtonian ($\mu = 0$) and Yukawa interactions between the pendulum and attractor. We divide our source densities into layers consisting of m identical sectors (wedges) of a right circular toroid equally spaced in θ. The wedges have inner and outer radii r_i and r_c, thickness t and angular width 2β. The midplanes of the wedges are at a vertical position h and their bisector is offset in θ from $\theta = 0$ by θ_0. The wedges all have mass density ρ, and spin density ρ_s. If the geometry we are calculating contains alternating sectors of different densities ρ^a and ρ^b, the net torque can depend only on the density difference $\Delta\rho = |\rho^a - \rho^b|$ between the sectors, since by symmetry anything that is completely uniform in θ can produce no torque. The Fourier-Bessel formulation respects this fact by having the layers with densities ρ^a and ρ^b produce torques with opposite signs because of the π/m difference in their starting phases θ_0^a and θ_0^b.

The θ and z integrals can be done by hand

$$I^s_{\binom{1}{2},l} = \frac{m\rho}{m_e}\frac{2\sin(l\beta)}{l}\,e^{\mp il\theta_0}\sinh\left(\frac{t\sqrt{k^2+\mu^2}}{2}\right)\,\frac{2\,e^{\pm\sqrt{k^2+\mu^2}h}}{\sqrt{k^2+\mu^2}}\int_{r_i}^{r_c}\mathrm{d}r\,r\,J_l(kr) \quad (2.4)$$

and the integral over r has a convenient and rapidly converging series expansion, leaving only the k integral of Eq. 2.2 to integrate numerically.

The monopole-dipole potential (Eq. 1.1) and dipole-dipole potential (Eq. 1.2) have derivative expressions that allow us to make use of the same cylindrical expansions for $G(\vec{r},\vec{r}') = e^{-\mu|\vec{r}-\vec{r}'|}/4\pi\,|\vec{r}-\vec{r}'|$

$$V_{\vec{\sigma}\cdot\vec{r}} = -\frac{g_s^1 g_p^2}{8\pi m_e}\,(\hat{\sigma}_2\cdot\nabla)\,\frac{e^{-\mu r}}{r}; \tag{2.5}$$

$$V_{dd}(r) = -\frac{g_p^1 g_p^2}{16\pi m_e^2}\,(\hat{\sigma}_1\cdot\nabla)\,(\hat{\sigma}_2\cdot\nabla)\,\frac{e^{-\mu r}}{r}. \tag{2.6}$$

Since the spin-density variation in our sources is azimuthal, $\hat{\sigma}$ points in the $\hat{\theta}$ direction and we can replace $\hat{\sigma}\cdot\nabla$ with $\frac{1}{r}\frac{\partial}{\partial\theta}$. This cancels a factor of r in the r integral and brings down a factor of $\mp il$ from the θ integral. Remembering the factor of $1/2m_e$ and using ρ_s as the spin density, the integrals for derivatively coupled sources are:

$$I^p_{\binom{1}{2},l} = \mp\frac{im\rho_s}{2m_e} 2\sin(l\beta)\,e^{\mp il\theta_0}\sinh\left(\frac{t\sqrt{k^2+\mu^2}}{2}\right)\,\frac{2\,e^{\pm\sqrt{k^2+\mu^2}h}}{\sqrt{k^2+\mu^2}}\,\int_{r_i}^{r_c}\mathrm{d}r\;J_l(kr). \tag{2.7}$$

The r integral in Eq. 2.7 is slightly different but also has a convenient series expansion

$$\int_0^z dt\,J_\nu(t) = 2\sum_{k=0}^{\infty} J_{\nu+2k+1}(z). \tag{2.8}$$

We used these results to extend our Fourier-Bessel implementation (`FBESSELN`) of Newtonian and Yukawa interactions to include the monopole-dipole and dipole-dipole interactions.

Equation 2.7 has some features worth commenting on. First, it shows that derivatively coupled potentials like the monopole-dipole and the dipole-dipole vanish for any closed loop of spin. If we choose the coordinate system of our loop so the spins point along $\hat{\theta}$, a closed loop of spins corresponds to Eq. 2.7 with $\beta = \pi$, and the factor of $\sin(l\beta)$ is zero for all terms in the expansion. The Yukawa and gravitational integrals do not vanish because $\sin(l\beta)/l = \beta$ for the $l = 0$ term. Secondly, it shows that the monopole-dipole interaction is orthogonal to the gravitational and dipole-dipole interactions. The monopole-dipole potential contains one derivatively coupled source (Eq. 2.7) and one Yukawa (Eq. 2.4) source while the gravitational potential, contains two Yukawa sources and the dipole-dipole potential contains two derivatively coupled sources, so for the same sets of sources

the monopole-dipole interaction has an additional factor of i and a corresponding $\pi/2 \times 1/m$ phase shift.

We want to find the amplitude of each harmonic component of the torque. The j^{th} harmonic of the torque, τ_j is given by

$$\tau_j = -\frac{d}{d\theta} U_{mj}(\phi). \tag{2.9}$$

where ϕ is the relative angle between the attractor and pendulum. Since the derivative of sine (cosine) lags behind sine (cosine) by $\pi/2$, the torque components become:

$$\tau_j = mj\, U_{mj}(\phi - \pi/2Nl). \tag{2.10}$$

The actual magnet segments in our pendulum and attractor were trapezoidal and formed an annular polygonal-prism. In order to use the Fourier-Bessel expansion, we modeled the segments as $360°/m$ sectors of a cylindrical annulus with an inner radius equal to the inscribed radius (r_i) of the polygon and an outer radius corresponding to the circumscribed radius (r_c) of the polygon. This is a very good approximation at our symmetry number of $m = 10$. We also approximated the tungsten rods as sectors of annuli. Appendix A.2 describes how we chose the dimensions of a sector to best approximate the cylinders.

2.6 Optimization of the Active Element Geomtery

The optimal size and shape for the pendulum and attractor is a balancing act between more active material and a thicker, less sensitive fiber. The torsion constant κ of a thin fiber of diameter d grows as d^4 while the mass it can support only grows as its cross-sectional area or d^2. The thermal noise grows as $\sqrt{\kappa}$ where Q is the loss of and the deflection angle that must be resolved falls as $1/\kappa$. This scaling would suggest making the pendulum as small as possible. However, the need for a mirror to return the autocollimator beam and machining practicalities mean there will always be some passive mass that must be supported, constituting a 'minimal' pendulum. The torque on the pendulum due to new forces would increase as we imagine adding active mass to our 'minimal' pendulum. Eventually, the reduction in torque-sensitivity from the thicker fiber required to hold the heavier pendulum outweighs the increase in torque from additional active material. The optimal point depends not only

on the 'minimal' pendulum and the geometry of the active mass, but also the magnetic shielding and the mounting structure which constitute passive mass that scales with the active mass.

To select a design, we calculated the torque τ due to a new dipole-dipole interaction (Eq. 1.2) for a large number of feasible attractor-pendulum geometries. We estimated the total mass of the pendulum in each geometry and found the torsion constant κ of the thinnest fiber that would support that pendulum. This yielded the angular deflection signal τ/κ which, combined with the expected $\sqrt{\kappa}$ torque-noise dependence of the fibers, gave us an idea of the optimum pendulum and attractor geometry for probing dipole-dipole interactions. Based on these considerations, we chose a design with a smallest magnet dimensions of 3 mm, the smallest that we thought would be reasonable to work with. The optimized design had an estimated mass of 38.6 g of which 22.2 g were the magnets and 5.5 g the shields for an active to passive mass ratio of 1.35. The pendulum as constructed weighed 59.8 g of which 22.2 g were magnets, 4.0 g were the 4 tungsten calibration rods and 18 g were shields for an active to passive mass ratio of 0.78.

Chapter 3

DETAILED DESCRIPTION OF THE MARK I INSTRUMENT

3.1 Overview of the Torsion Balance Infrastructure

We performed these experiments using the torsion balance infrastructure and data analysis system developed for the short-range gravity experiments by C.D. Hoyle [36], Dan Kapner [40] and Ted Cook [39] successively. The pendulum and attractor operated in a vacuum of 10^{-6} Torr to reduce viscous damping noise. The pendulum hung from an 85 cm long, 28 μm diameter tungsten fiber with a prehanger that damped the swing and bounce modes of the fiber. Motorized stages moved the top of the fiber suspension in X, Y and Z, and rotated it about the fiber axis, with the position measured and recorded by micrometers. A stepper motor mounted to a rotary feed-thru below the vacuum can rotated the attractor assembly. A rotary encoder with 2^{11} pulses/revolution continuously monitored the turntable angle. We fed back the motor-drive voltage to lock the rotary encoder signal to a crystal oscillator. An autocollimator measured the pendulum twist by reflecting a laser spot off of a mirror mounted on the pendulum and detecting its return spot on a position-sensitive photo-detector. We monitored the pendulum-to-screen capacitance continuously through all of our data.

3.2 Pendulum & Attractor

3.2.1 Spin-Pendulum

Figures 3.1 and 3.2 show mechanical drawings and a photograph, respectively, of the spin-pendulum used in the work described in this thesis.

The pendulum hung from a #4-40 screw crimped to the torsion fiber. The fiber screw screwed into the the spring-loaded top hat leveling system designed and built by Dan Kapner [40]. A cube with four mirrored surfaces like the one used by Ted Cook [39] reflected the laser spot used to monitor the pendulum twist angle. A post below the mirror cube further

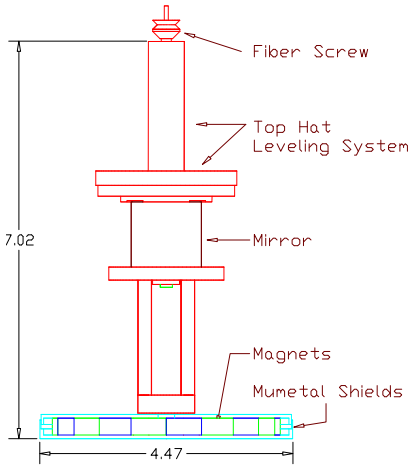

(a) Side view of the pendulum with the μ-metal shields cut away to show the magnet sections.

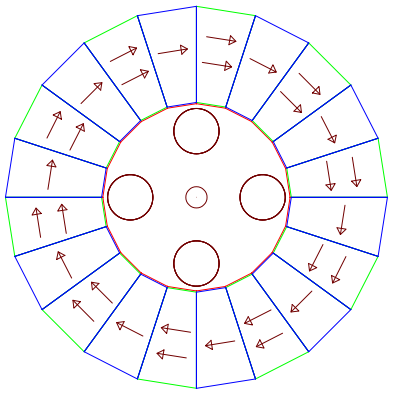

(b) Top view of the pendulum ring showing the magnet ring, centering-fixture and tungsten calibration rods. Arrows indicate the spin content of the Alnico (green) and $SmCo_5$ (blue) magnets.

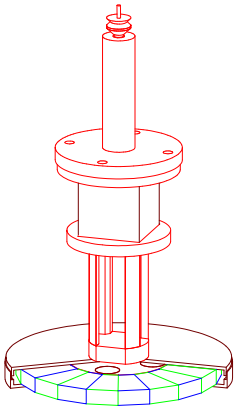

(c) Isometric view of the pendulum with the μ-metal shields cut away to show the magnet sections.

Figure 3.1: Mechanical drawings of the spin-pendulum

separated the active elements of the spin-pendulum from the suspension point to reduce pendulum wobble. A threaded pin connected the post to the leveling system and clamped the mirror cube between them. A 0.76 mm thick μ-metal can hermetically enclosed the active elements of the pendulum. Figure 3.3 shows the active elements of the pendulum. A 1 cm circle inscribed and a 2 cm circle circumscribed the 3 mm thick 20-sided polygon formed by the magnets. A 20-sided aluminum centering-fixture aligned the magnets relative to each other and to the rest of the pendulum. Four holes on a 1.4 cm bolt circle in the centering-fixture positioned four 4.76 mm diameter, 3 mm tall tungsten rods used for gravitational calibration. A screw passed through the centering-fixture and a small hole in the upper μ-metal can to connect the active elements with the pendulum body.

3.2.2 Spin-Attractor

Figure 3.4 shows drawings of the first generation spin-attractor assembly. The attractor spin-ring was the same as the pendulum spin-ring except that the attractor magnets were 4.17 mm thick. The alignment of the magnets and tungsten rods used a centering-fixture similar to that in the pendulum, with a 6.35 mm hole in the middle that fit on a centering pin on the turntable. The attractor calibration rods were the same in shape and location as those in the pendulum, except they were 4.67 mm tall. Annuli cut from 0.25 mm thick μ-metal lay directly on the upper and lower surfaces of the attractor spin-ring and provided an immediate flux return for magnetic leakage fields. Gravitational compensation disks above and below the μ-metal annuli partially nulled the gravitational 20-pole of the attractor. More detail on the compensation scheme is given in Section 3.2.3. A 0.76 mm thick μ-metal can enclosed this entire assembly aside from a hole for the centering pin. Figure 3.5 shows the spin-attractor in various stages of assembly.

3.2.3 Gravitational Compensation of the Spin-Attractor and Spin-Pendulum

The difference in mass density between $SmCo_5$ and Alnico would produce a gravitational torque at the same 10ω frequency as the spin signal. The densities given by the suppliers were 8.3 g/cm^3 for $SmCo_5$ and 7.37 g/cm^3 for Alnico. The resulting gravitational 10ω

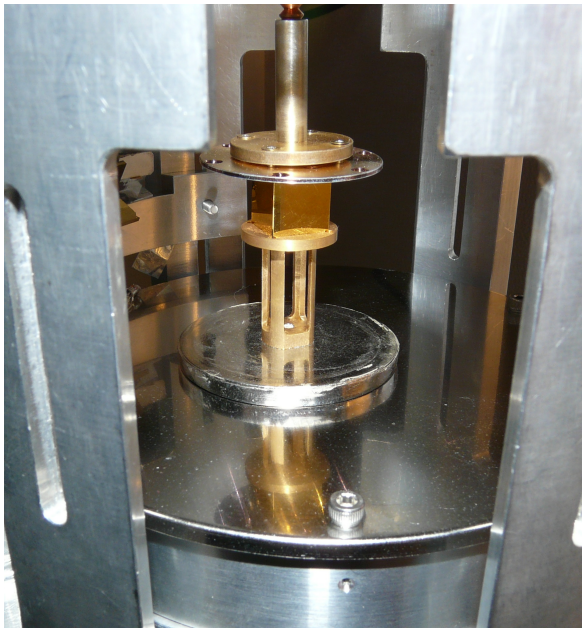

Figure 3.2: Photograph of the spin-pendulum sitting in the apparatus

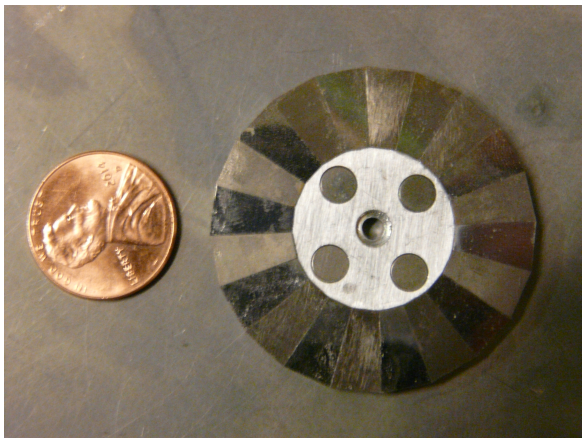

Figure 3.3: Photograph of the active elements of the spin-pendulum. The penny is for scale.

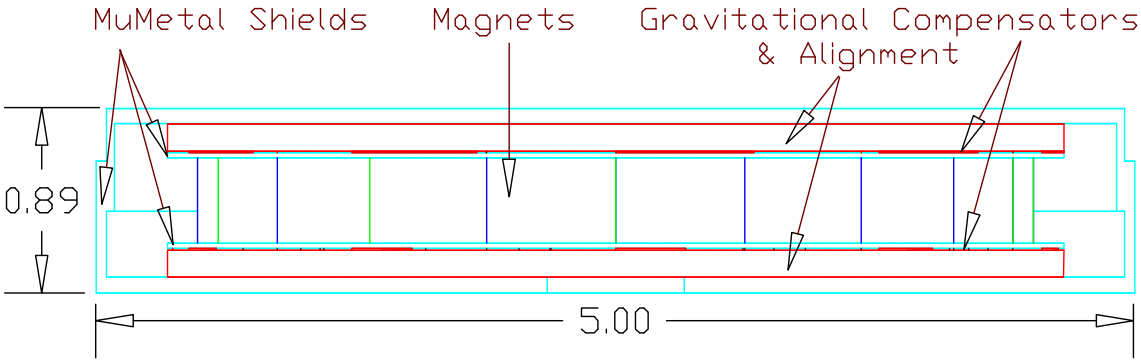

(a) Side view of the attractor with the μ-metal shields cut away to show the attractor assembly.

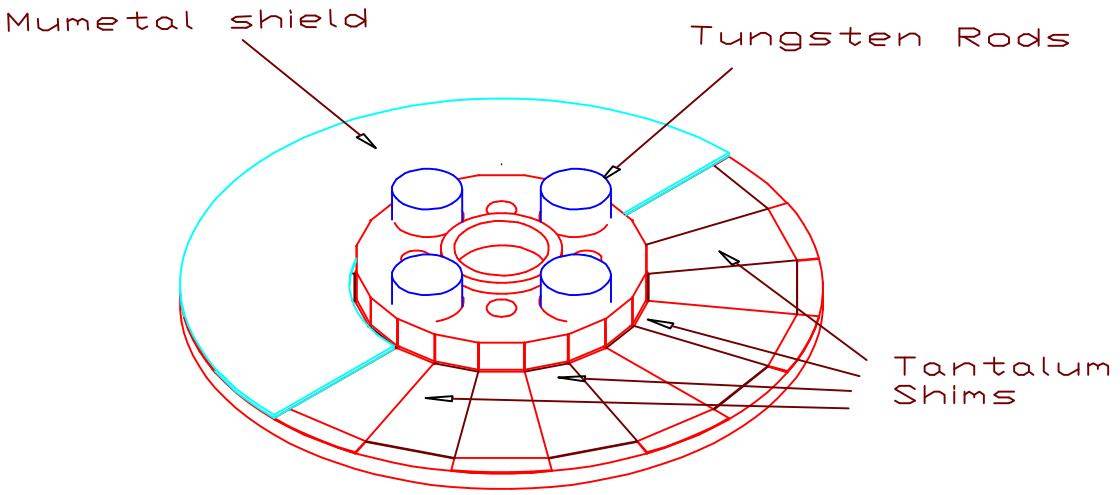

(b) View of the lower half of the attractor assembly. The μ-metal shield is cut away to show the inlayed tantalum shims underneath. The shims are the same size as the magnets and do not extend all the way to the outer radius of the alignment disk. The spin-ring (See figure 3.1b) sits on top of the μ-metal shield, aligned to the shims by the centering-fixture. A matching set of shield and compensators, held by the other half of the centering-fixture, sit on top of the magnets. With the upper and lower halves in place, the tungsten rods are flush with the centering-fixture on both above and below. Figure 3.5 makes this clear by showing the attractor at various stages of assembly

Figure 3.4: Mechanical drawings of the spin-attractor

(a) Compensator disks with shims glued in and mounted on centering-fixtures.

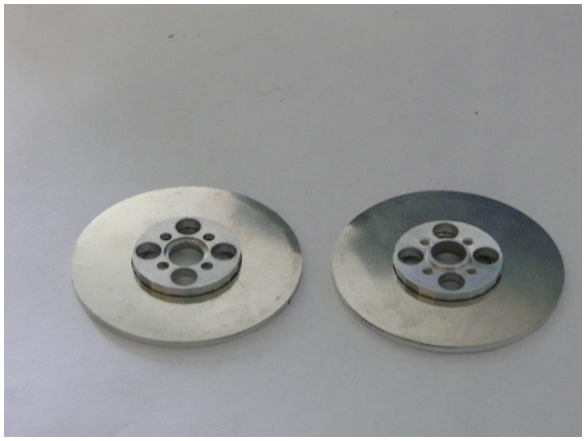

(b) μ-metal annuli in position on the compensator disks.

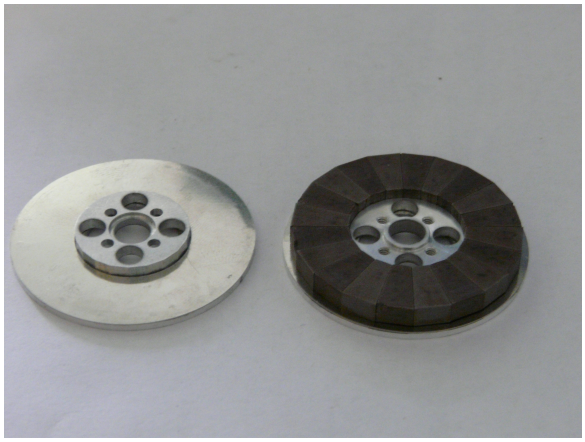

(c) Attractor spin-ring mounted with the centering-fixture aligning it with the compensator disk below the μ-metal annulus.

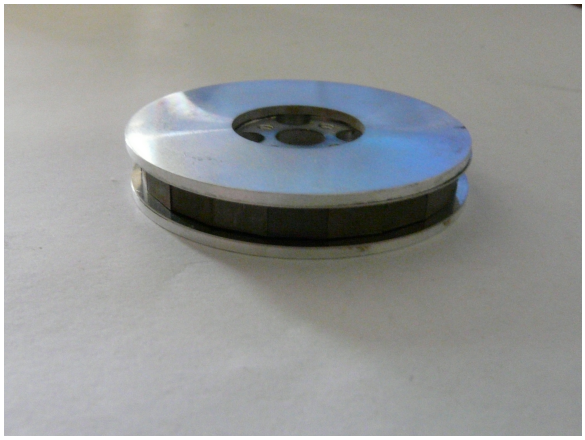

(d) Second compensator disk and μ-metal annulus placed on top of the attractor.

Figure 3.5: Photographs showing the step-by-step assembly of the spin attractor.

signal would be well above our noise level and would contribute a significant systematic background. Thin, high-density foils placed directly above and below the Alnico segments evened out the effective mass difference between neighboring segments and reduced the expected gravitational torque by a factor of 10 and pushed it below our sensitivity, shown in Fig. 3.6.

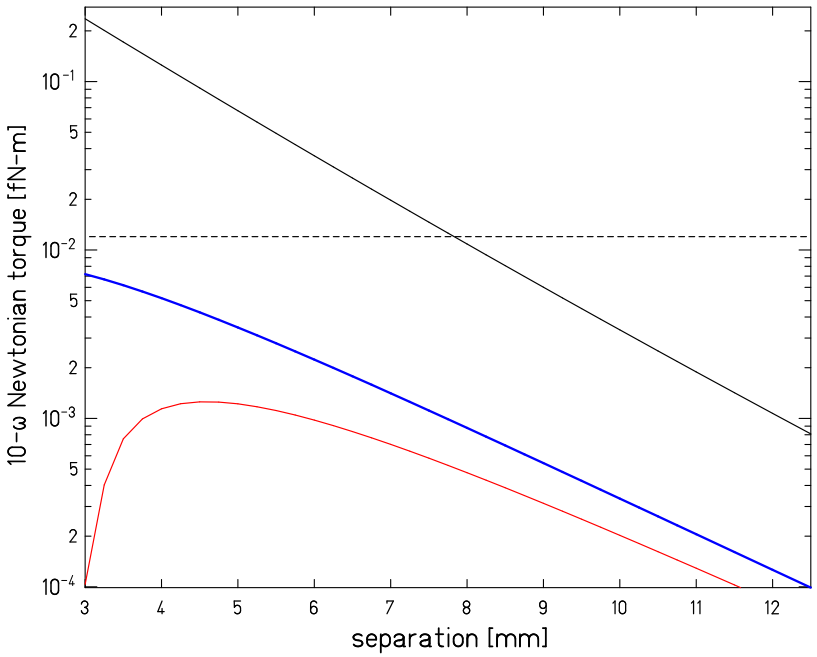

Figure 3.6: Calculations of the gravitational torques on the pendulum as a function of pendulum-attractor vertical separation, with and without the gravitational compensation system. The dashed line shows the torque sensitivity we reached in our data taken with the spin attractor. We took data at 6.1 mm, 6.9 mm and 7.6 mm. The black line shows the calculated torque produced by an uncompensated attractor. The red line shows the calculated torque using the design values of all the component masses. The heavy blue line shows the calculated gravitational torque on the pendulum using the measured masses for all components.

We used special compensation-disks to position the high-density shims. We chose this scheme because it allowed a high-μ annulus to lie on the magnets and provide an direct flux

return (see Sec. 3.2.2). The compensation-disks consisted of 1.27 mm thick aluminum disks inlayed with 10 tantalum wedges that were of the same trapezoidal shape as the magnet wedges and 0.076 mm thick (see Fig. 3.4b). These sat outside (above and below) the first layer of magnetic shielding on the attractor, with the shims inlayed on the side facing the magnets. The grooves milled in the disks to position the tantalum shims also mated with grooves in the upper and lower surfaces of the centering-post and mechanically aligned the compensators both radially and azimuthally. Figures 3.4 and 3.5 demonstrate how the attractor assembly fit together. The total gravitational compensation system therefore consisted of 0.076 mm of tantalum (16.7 g/cc) placed 0.254 mm above and below each Alnico magnet and 0.076 mm of aluminum (2.7 g/cc) at the same position above and below each $SmCo_5$ magnet. We did not compensate the pendulum to avoid the added mass and volume of the alignment disks.

We tuned the compensation system by adjusting the precise thickness of the attractor ring given the commercially available shim thicknesses and densities. After making the attractor we calculated the expected torques again using the measured masses of the components. Appendix A.1 gives details how we adjusted the model to match the measured component masses. Figure 3.6 shows the calculates gravitational torques as a function of pendulum-attractor separation with and without the compensator shims in place, and the effect that the difference between the anticipated and actual masses of the components had on the quality of the cancelation. Smartscope measurements showed that the magnets could shift by $\pm 0.17^\circ$ relative to the centering-post and compensation-shims. The effect of such misalignments of the compensators is remarkably small, as shown in Figure A.1.

3.2.4 mass attractor

The mass attractor had the same shape and dimensions as the spin attractor but had alternating wedges of copper and vacuum in place of the alternating wedges of $SmCo_5$ and Alnico in the spin-rings. We used this attractor in our search for monopole-dipole interactions and to center the pendulum above the attractor rotation axis without confusion from magnetic effects. We also validated our calculations of the gravitational background in

our dipole-dipole experiment using this attractor. We used the same tungsten rods that we used in the spin-attractor, so the tungsten rods extended 0.51 mm above the copper wedges in this design. Figure 3.7 shows a photograph of the mass attractor on the turntable, with the tungsten rods removed.

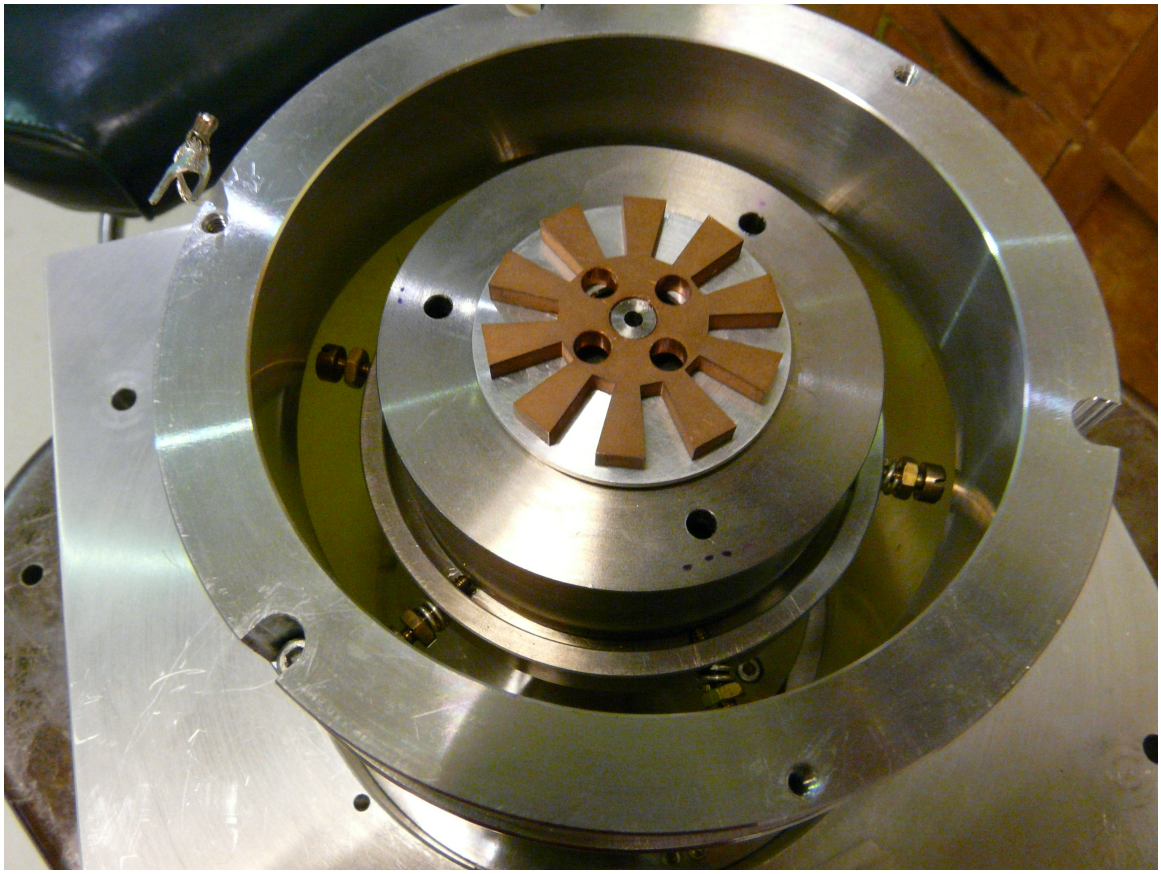

Figure 3.7: Photograph of the mass attractor on the turntable. The tungsten rods sat in the cylindrical holes.

3.3 Details of the Spin Rings

3.3.1 Construction

We cut the Alnico and $SmCo_5$ pieces to shape on an electric discharge machine. Achieving the saturation field needed to magnetize the $SmCo_5$ magnets (3×10^6 A/m) ourselves would

be a challenge, so we cut the $SmCo_5$ segments from commercially magnetized materials. Alnico magnets are magnetically soft, and the Alnico segments magnetized easily in the field of the spin-rings. We assembled the spin-rings on a sheet of μ-metal to control the highly magnetic components. We then tuned the fields of the individual magnets to minimize the external magnetic field.

3.3.2 Mass Measurements

The standard way of measuring the mass of an object is to measure the vertical force f_z on the object and then use the relationship $f_g = mg$ to extract the mass. This requires assuming that the vertical force f_z is entirely gravitational. The possibility of additional, magnetic, contributions to f_z makes mass measurements of magnetized materials challenging.

To weigh the magnets, we sandwiched each magnet segment between two 5.2 cm $\times$ 5.2 cm $\times$ 0.076 cm μ-metal plates with the magnetization of the segment parallel to the plates. This significantly attenuated the magnetic contribution to f_z. We looked for magnetic contamination of our measured weights by weighing each magnet in four configurations. We looked for a magnetic coupling to lab-fixed objects such as iron in the table by weighing each magnet at two heights (3.91 cm and 7.62 cm) above the balance. We looked for couplings to fields that do not vary spatially, such as the earth's field, by flipping the magnet-shield stack over and reweighing it at both heights. The masses of the magnets showed no evidence of position- or orientation-dependent magnetic effects.

Table C.3 lists all the mass measurements taken of the pendulum $SmCo_5$ magnets. The instrumental uncertainty of our balance was $\sim 50\mu$g. The average "mass" difference between the two orientations of the magnets was 80μg, with a standard-deviation of the sample of 115μg. The magnet masses were 80μg less, on average, when weighed 7.62 cm above the balance than when weighed 3.91 cm above the balance with a sample standard deviation of 70μg. The results of these systematic checks were similar for all the other sets of magnets. With only marginally resolved position or orientation dependence in our measurements, we used the average of the measurements at all positions and orientations as the mass for each magnet.

3.3.3 Magnetic Field Measurements

We measured the external magnetic fields of the attractor and pendulum components by rotating them on a turntable near a stationary, rigidly-mounted magnetic field probe. This allowed robust measurements of the magnetic fields produced by our components without contributions from absolute offsets and drifts in either the probes or the ambient magnetic field. We used an Alphalab single-axis giant-magneto-resistance probe to measure small residual fields between 10 μG and 2 G. The GMR probe saturates at 2 G so we used a F.W. Bell single-axis Hall effect probe to measure stronger fields. We could mount the probes to measure all three ($\hat{r}, \hat{\theta}$ and $\hat{z}$) components of the magnetic field. A National Instruments Analog-to-Digital converter fed our Data Acquistion computer (DAQ) which recorded the output voltages of the probes as a function of time and encoder angle. We set the calibration coefficients for the DAQ so that the probe output voltages mapped to the magnetic fields displayed by the probes. Linear translation stages allowed the probe to move reproducibly along three axes with 2.5 cm of travel. A μ-metal box enclosed the entire apparatus. Figure 3.8 shows a photo of the setup.

3.3.4 Magnet Selection

We cut 24 $SmCo_5$ magnets for the pendulum and 15 $SmCo_5$ magnets for the attractor from a single block of magnetized $SmCo_5$. We measured the magnetization strength of each $SmCo_5$ magnet by mounting each one in a chuck on the turntable with its magnetization pointing in the radial direction. We placed the Hall-effect probe 3.8 cm away and oriented to measure the radial field. We measured each piece for several (5-10) rotations of the turntable and used the peak-to-peak magnetic field readings as a proxy for the magnetization strength. We selected the 10 $SmCo_5$ magnets for the pendulum and for the attractor from that had the smallest spread in peak-to-peak magnetic field. The spread in the magnetic field readings was 2.9% for the full set of pendulum magnets and 1.4% for the subset actually used in the pendulum ring. The spread was 1.6% for the full set of attractor magnets and 0.7% for the subset used in the attractor ring.

We cut 16 Alnico magnets for the pendulum and 11 Alnico magnets for the attractor,

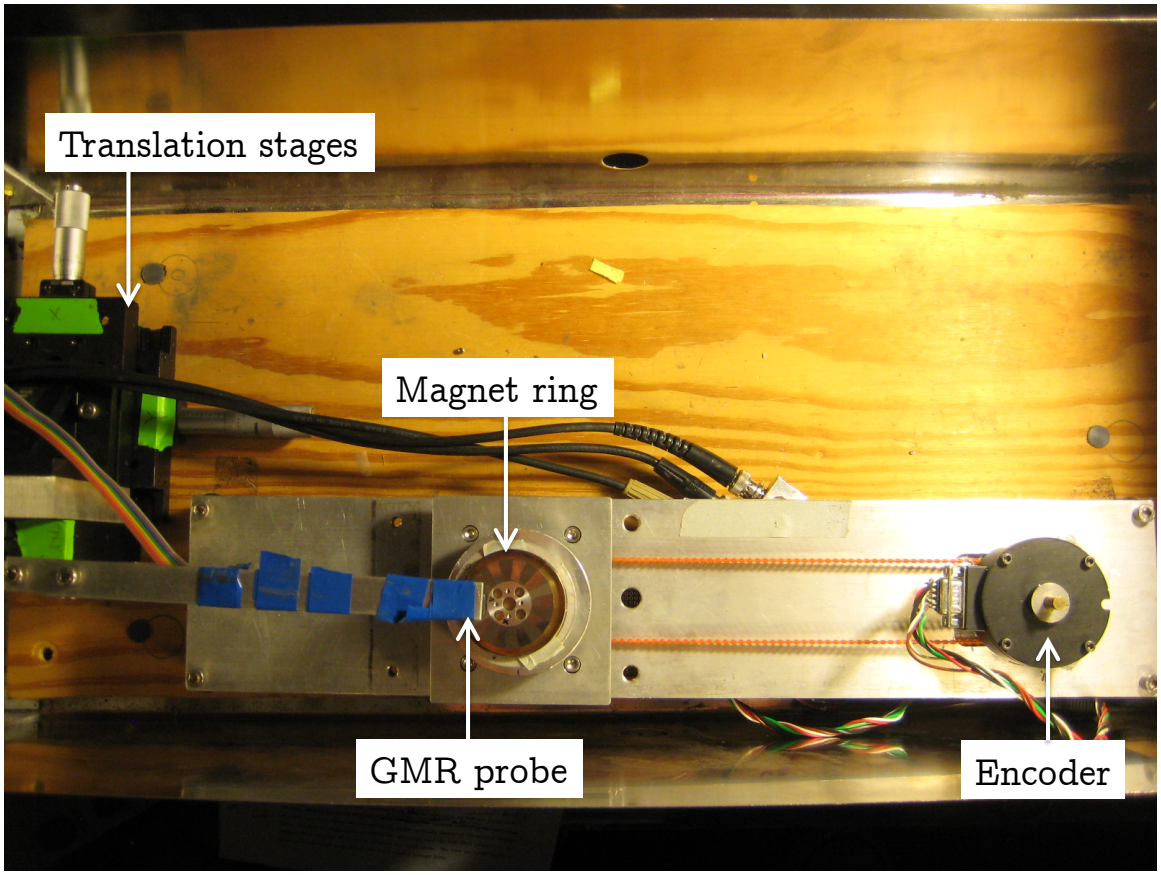

Figure 3.8: A picture of the magnetic measurement setup. This photo shows the GMR probe installed above a magnet ring. The magnet ring sits on a turntable rotated by a drive belt (orange). The encoder measures the angle that the drive shaft has turned. The stepper motor that turns the shaft is not visible underneath the encoder. The translation stages on the left move the probe location reproducibly in three directions.

and used the 10 of each with the smallest spread in mass. See Section 3.3.2 for details about the mass measurements.

Appendix C.1 contains specifics about the magnets used in the attractor and their arrangement, and Appendix C.2 contains specifics about the magnets used in the pendulum and their arrangement.

3.3.5 Leakage Fields

We measured the leakage magnetic fields of the spin-rings by mounting the probe above the ring so that the magnet elements passed directly beneath the probe as the turntable rotated. We could measure the azimuthal and radial magnetic fields at many positions by moving the probe horizontally in x and y. Mounting the probe vertically measured the vertical leakage fields. All field readings taken outside the spin-rings directly used the Hall-effect probe.

With the spin-rings assembled, we tuned the magnetization the segments by placing them in a large external magnetic field. A set of magnet-iron arms returned the flux from two powerful NdFeBo magnets through a small gap and concentrated the field to a region the size of one magnet segment. A slot cut in each arm fit over the spin-rings and allowed us to magnetize the individual magnet segments in situ. We could vary the magnitude of the magnetic field in the gap between 300 G and 1360 G with steps of about 60 G by connecting the two arms of the flux with different combinations of thin iron shunts that returned a portion of the flux. See Figure 3.9 for an example of how this tuning procedure altered the leakage magnetic field of the spin-rings.

When we first assembled the ring, the residual azimuthal magnetic field was 100 G peak-to-peak over one full rotation of the ring at a point 3.8 mm above the rings. Iteratively tuning the magnetization of the ring ultimately reduced the residual magnetic field down to 8 G peak to peak at the same location (Figure 3.10).

3.4 Magnetic Effects

Our torsion balance has the torque-sensitivity to constrain new dipole-dipole interactions down to $\mathcal{O}(10^{-14})$ below magnetic strength. The spin-contrast in our spin-rings produces a 20-pole spin-field with the quantity of polarized spins that would produce a magnetic

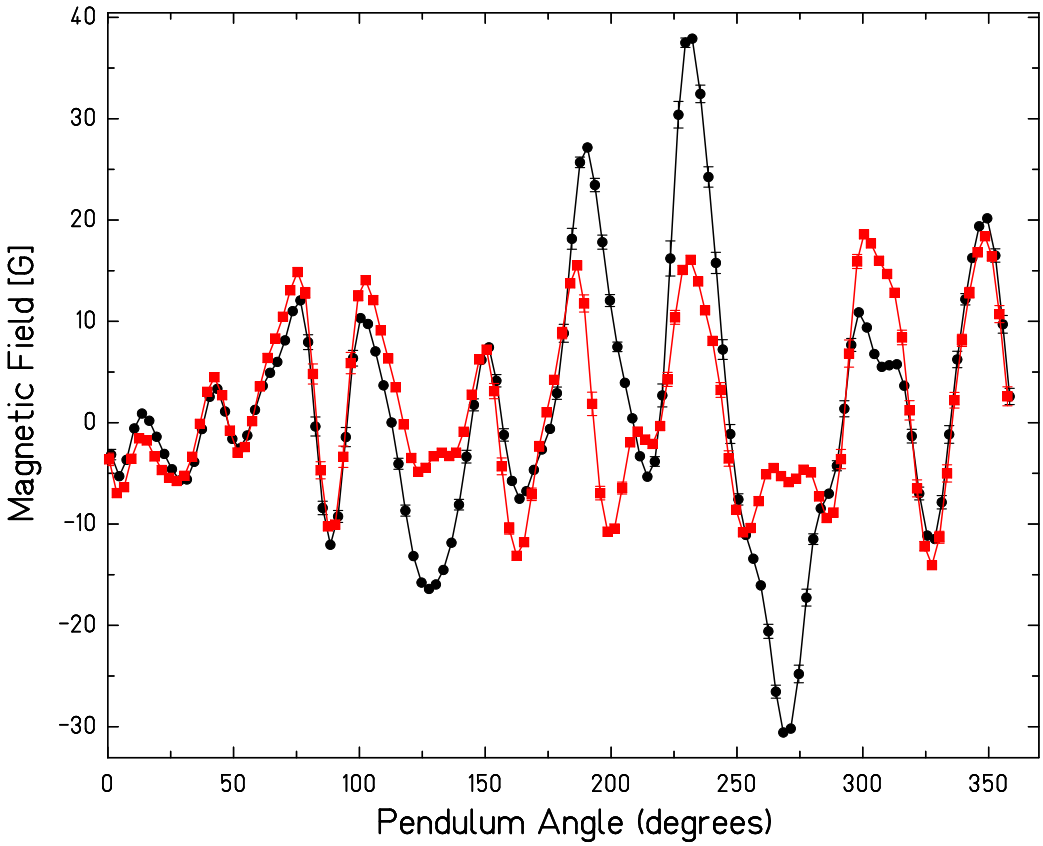

Figure 3.9: The effect of a single cycle of our iterative magnetization technique as applied to the pendulum ring. The black circles [`tst-wash run2154`] show the magnetic leakage field at the start of this iteration. We applied an external magnetic field in the same direction as the field in the ring to enhance the magnetization of A3 (at 190°) and A13 (at 220°), and against the field of the ring to reduce the magnetization of A9 (at 275°). The red squares [`run2155`] show the magnetic leakage field after this round of tuning.

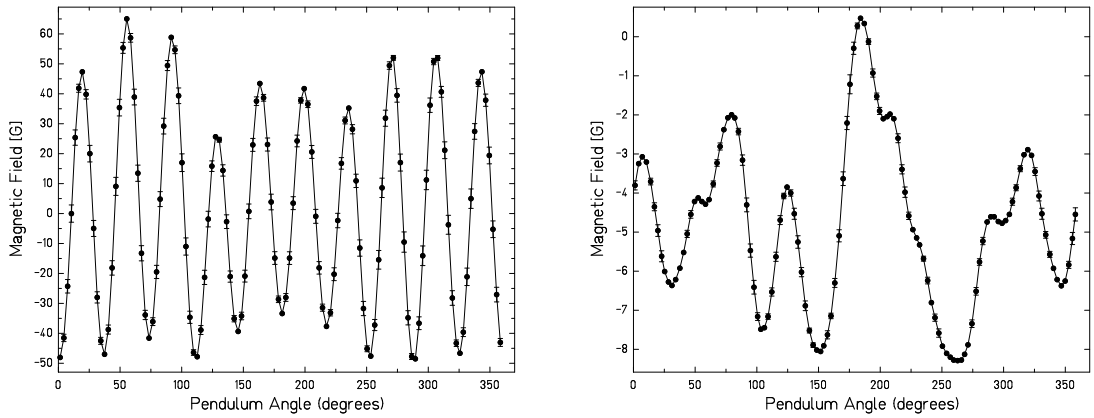

Figure 3.10: The azimuthal magnetic field measured 3.8 cm above the pendulum ring before (left, `[tst-wash run2150]`) and after (right, `[tst-wash run2467]`) repeatedly tuning the magnetization of the magnets.

20-pole of 5×10^3 G. The torque on the pendulum depends on the product of the field from the pendulum and the field from the attractor, so the 10ω magnetic leakage fields must be $\mathcal{O}(10^{-7})$ smaller than the spin-field, or $\mathcal{O}(500\,\mu\text{G})$ in order to not constitute a significant background for our measurement.

3.5 Magnetic Isolation of the Pendulum

We surrounded each spin-ring with cans made from a pair of circular 0.76 mm μ-metal thick disks hot swaged on a lathe to form cups, pictured in Figure 3.11. The inner edge of one cup and outer edge of the other were turned down on a lathe to make a tight fit as shown in Figure 3.12. The fit between the cups remained very good following the annealing procedure required to restore their magnetic properties after swaging. Putting the spin-rings in the cans reduced the peak-to-peak residual field roughly 3 mm above the magnets from 8 G down to ~ 10 mG. Figure 3.13 shows the trace of the magnetic field a little over 2 mm outside the pendulum can.

The spin-attractor had additional 0.25 mm thick μ-metal annuli sitting directly on the surface of the magnets to provide a direct flux return while still allowing mechanical align-

Figure 3.11: A photograph of the μ-metal can which enclosed the pendulum active elements.

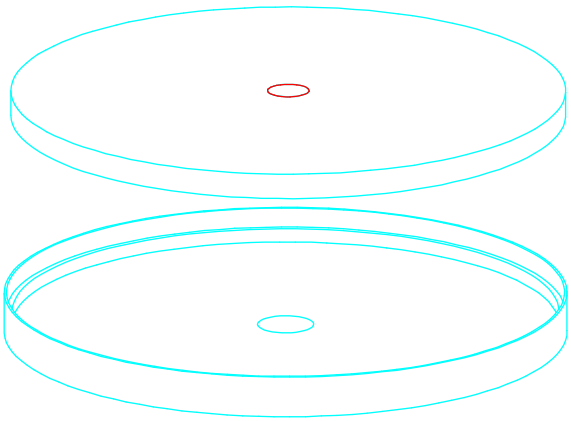

Figure 3.12: Mechanical drawing of the pendulum cans. The upper can fit into the cut out section of the lower can. The hole in the upper can allows a #4-40 screw to attach the spin-rings to the pendulum apparatus. A 0.25 mm deep alignment circle cut in the lower can centers the screw head and spin-rings on the shielding cans.

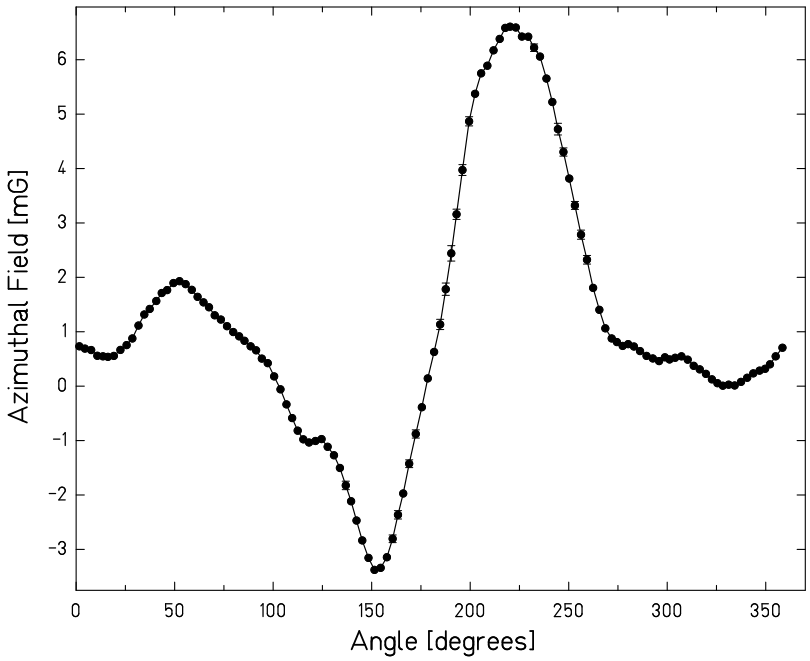

Figure 3.13: Trace of the azimuthal magnetic field strength measured by the GMR probe 2 mm above the pendulum ring in its can [`tst-wash run2679`].

ment of the gravitational compensation disks with the centering-fixture, as shown in Fig. 3.4.

A 1.27 mm thick, cylindrical, μ-metal 'house' entirely enclosed the pendulum on the sides and from above except for a hole in the top for the fiber and another in the side for optical access to the pendulum. A flange on the base of the 'house' bolted to a μ-metal screen separating the pendulum and attractor to form a complete μ-metal circuit around the pendulum. We used a single layer of 0.25 mm thick μ-metal as the screen with the gravitational-attractor and a multi-layer μ-metal screen with the spin-attractor. The screen we used with the spin-attractor consisted of a stack of 5 layers of 0.25 mm thick μ-metal disks with the top 4 layers separated by 0.2 mm thick aluminum foils and the bottom layer separated by 1 piece of 0.15 mm thick stainless steel. We used a stainless steel layer so we could add another layer of μ-metal without waiting for more aluminum shim to arrive. Figure 3.14 shows the enclosure.

We wrapped Metglas around the screen mount to encircle the attractor and bearing but this showed no appreciable effect on the magnetic coupling. With the full shielding in place, the magnetic field variation at the pendulum location over a full rotation of the spin-attractor was below the $< 2\mu$G sensitivity of our GMR probe.

3.5.1 Effectiveness of the Multilayer Screen

The multi-layer screen separating the pendulum from the attractor was essential in pushing the 10ω magnetic coupling between the pendulum and attractor below our torque sensitivity. By far the largest magnetic effect in our data was the interaction between the residual magnetic dipole of the attractor and the residual magnetic dipole of the pendulum. This produced a large 1ω twist on the pendulum and provided a straightforward diagnostic of the magnetic coupling between the pendulum and attractor. Our science signals were a thousand times smaller than the very large 1ω twist, so reducing the 1ω coupling was essential. Splitting the screen into multiple thin layers with small spaces between them was significantly more effective in reducing the 1ω twist than increasing the thickness of the high-μ screen. Table 3.1 shows the details of these results. Figure 3.15 shows a comparison

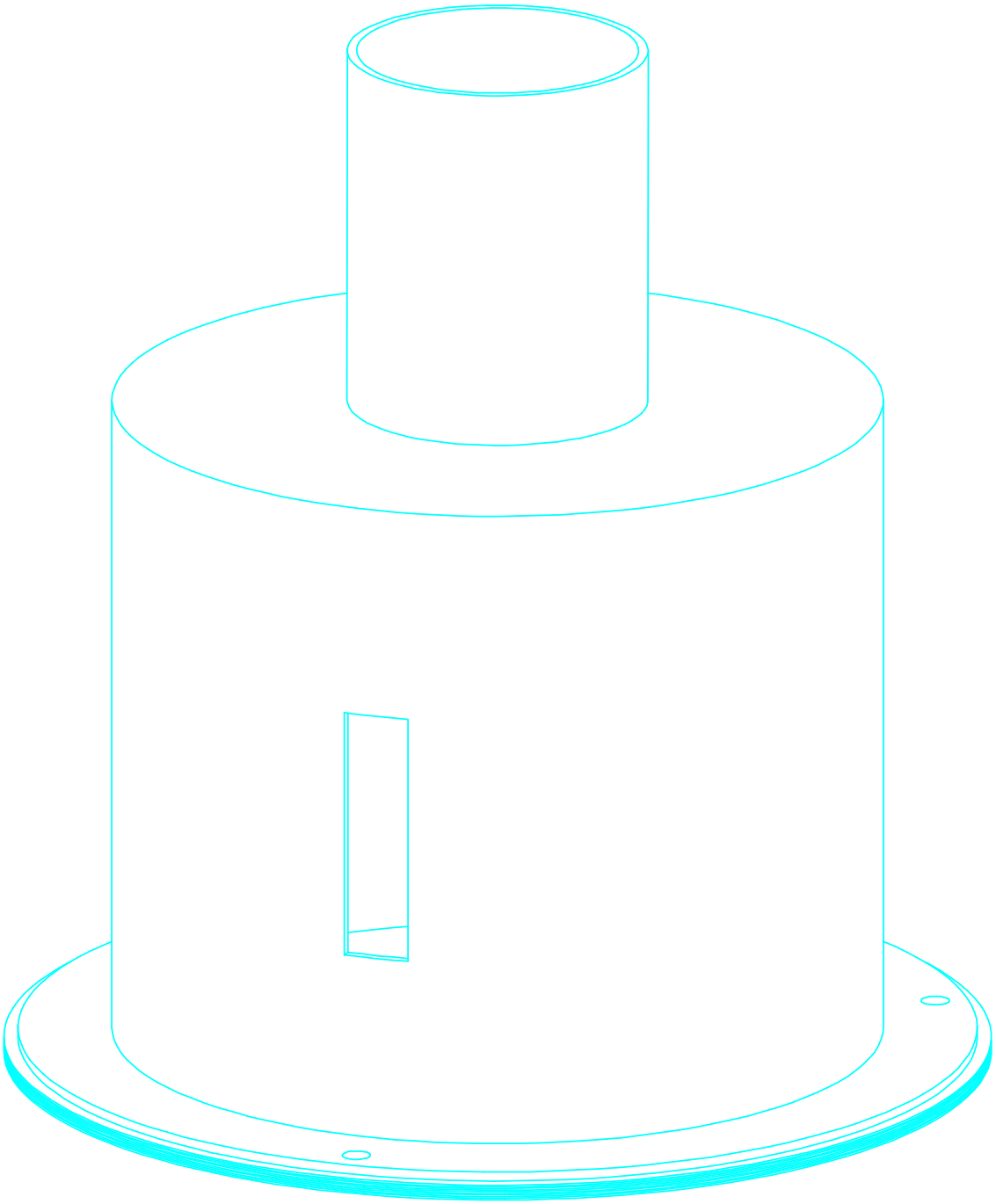

Figure 3.14: Drawing of the μ-metal "house" on top of the multi-layer screen. The house and screen are connected by screws in the outer rim. A metal shroud around the fiber extends down into the hole in the top of the "house".

of two power spectra, one (`run4223`) taken with a single 1.27 mm solid μ-metal screen and the other (`run4421`) with a 5-layer μ-metal screen with the same total amount of μ-metal and the same pendulum-to-attractor separation.

Table 3.1: The effect of different screen configurations on the attractor-pendulum magnetic coupling. Z_{sep} is the distance in mm between the closest surfaces of the pendulum and attractor spin-rings. The signals are in torque units [fN-m]. The column labeled High ω is the average of the 7,11,13, and 14ω torques. This is was our conservative estimate of a magnetic background at 10ω, as described in section 4.3.2.

Screen Configuration	Z_{sep}	Run	1ω	High ω
0.76 mm thick shield	6.1	4214	2410	0.65
1.27 mm thick shield	6.1	4223	2295	0.35
5×0.25 mm thick shields and 0.2 mm gaps	6.1	4419-21	24.16	0.022
1.27 mm thick shield	6.9	4231	1271	0.19
1.27 and 0.76 mm thick shields and 0.25 mm gap	6.9	4233	147	0.076
5×0.25 mm thick shields and 0.2 mm gaps	6.9	4425,4416	12.72	0.016

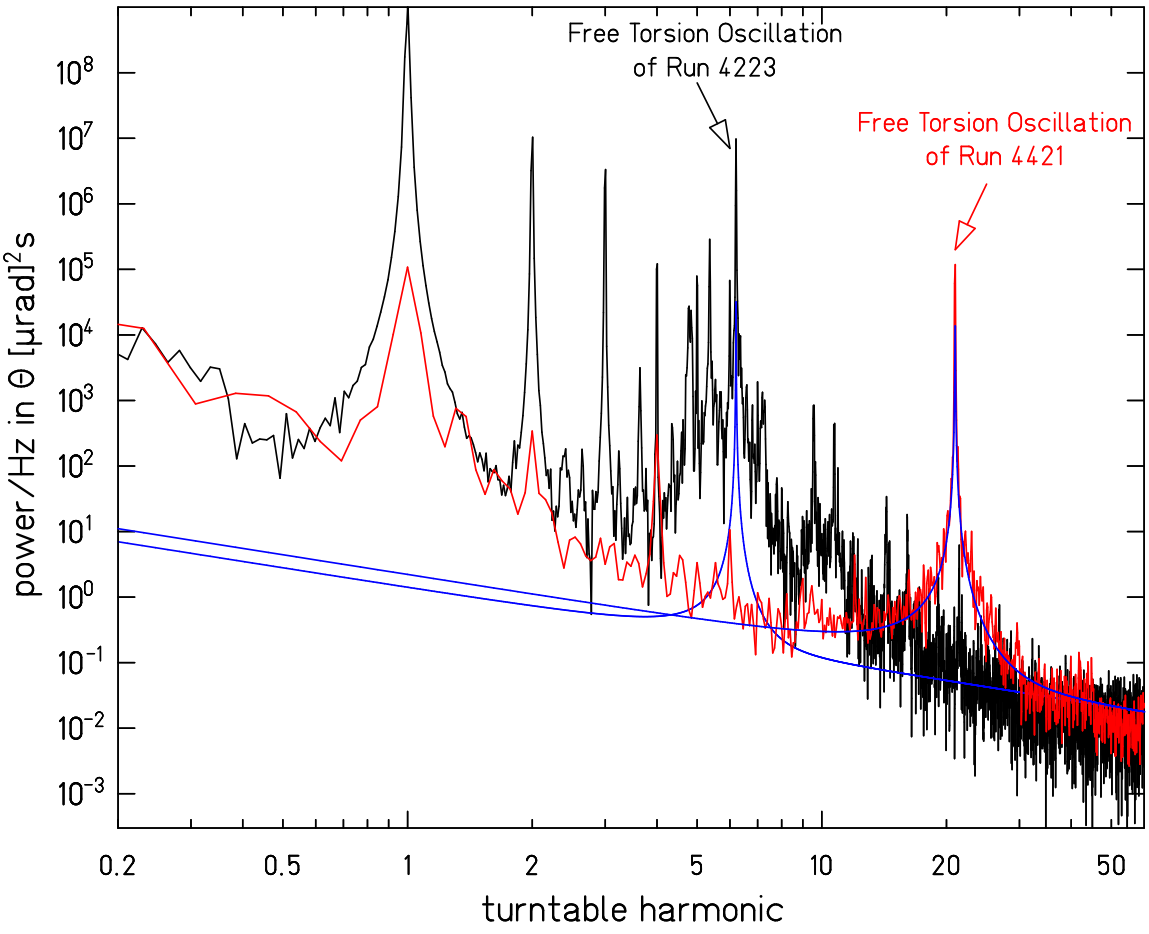

Figure 3.15: Power spectra of two runs with the same total separation and amount of μ-metal between the pendulum and attractor. The black curve shows the power spectrum of `run4223` which had a 1.27 mm thick μ-metal screen. The red curve shows the power spectrum of `run4421`, taken with a screen made from 5 layers of 0.254 mm thick μ-metal sheets separated by 0.20 mm spacers. The attractor rotation rate differed between the two runs, so the free torsion peak came at 7ω in `run4223` and 21ω in `run4421`

.

Chapter 4

EXPERIMENTAL PROCEDURE

4.1 Alignments and Calibrations of the Mark I Instrument

The spin interactions probed in these experiments increase in strength as the distance between spins decreases (Eqs. 1.1,1.2). In order to maximize our sensitivity to new forces, we positioned the pendulum, attractor, and screen to minimize the average separation of the spin-polarized elements over the course of a full attractor revolution.

This means the attractor should be as perpendicular to and centered on the rotation axis of the bearing as possible. The screen should be as close to and as parallel to the attractor as possible. The suspension axis of the pendulum should align with the rotation axis of the attractor, and the pendulum ring should be as parallel to the screen as possible.

We aligned the attractor and screen using the SmartScope measuring machine shown in Figure 4.1, and we aligned the pendulum suspended in the apparatus. Our alignment errors were mostly of order of tens of μm, and were negligible compared to the overall pendulum-attractor separations of $\sim 6\,$mm for the spin-attractor data and $\sim 2\,$mm for the gravitational-attractor data.

4.1.1 Attractor

The attractor rings sat on a titanium mounting cup attached to the turntable bearing via a kinematic mount with 5 degrees-of-freedom [39](p. 70). We adjusted the kinematic mount to align the attractor symmetry axis with the axis of the bearing.

4.1.1.1 Leveling

Three pairs of push-pull screws tipped the cup relative to the bearing axis. We measured the vertical distance to the upper surface of the attractor with a stationary spring-loaded dial-indicator at a fixed position directly above the attractor and 1.5 cm horizontally offset

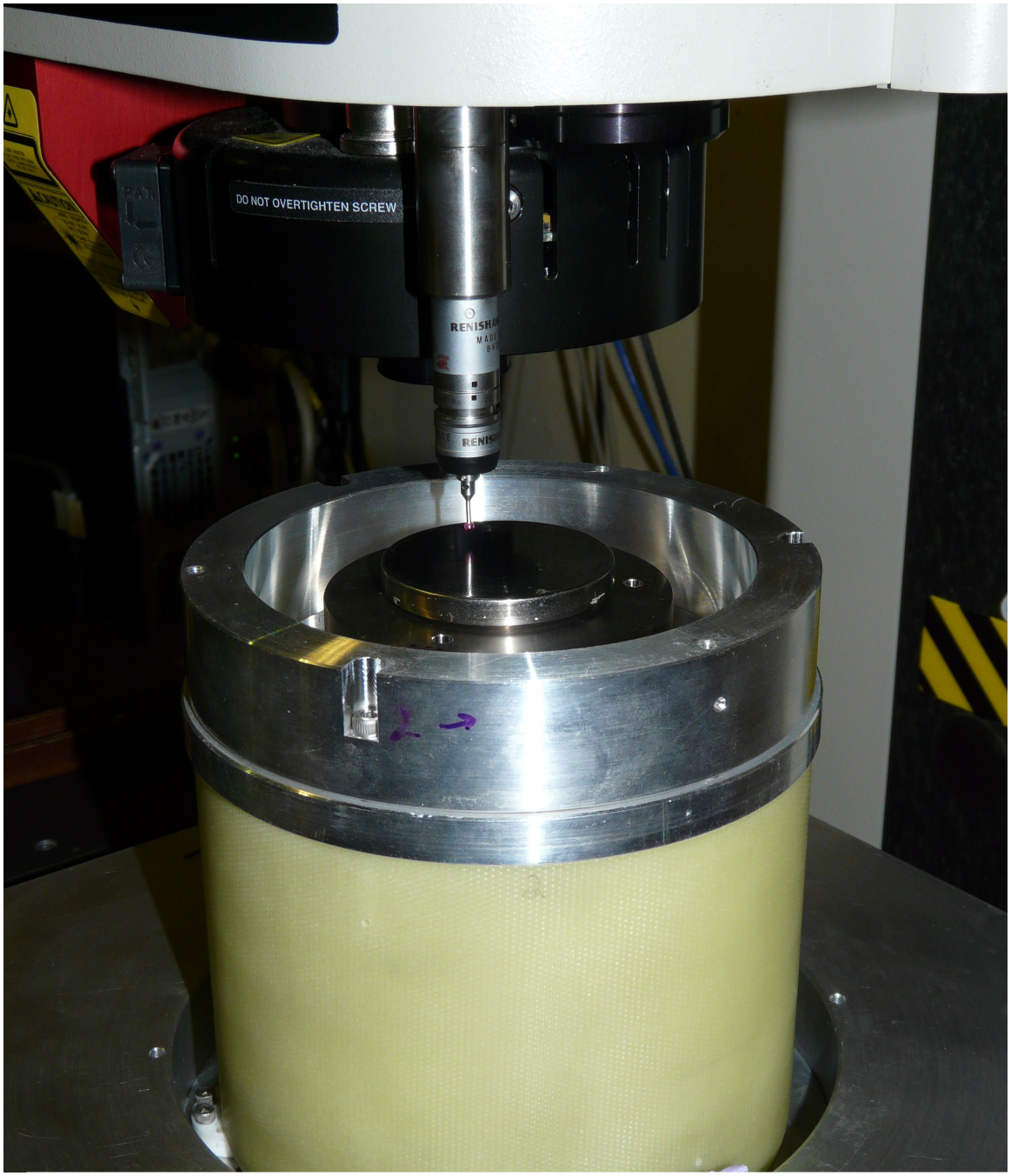

Figure 4.1: Photograph of the spin attractor mounted on the SmartScope for alignment.

from its center. After leveling, the distance measured by the dial indicator varied by less than 30 μm total over a full rotation of the attractor bearing.

4.1.1.2 Centering

We centered the attractor by looking at the edge of the mounting cup under the smartscope camera while rotating the bearing by hand. We translated the cup using a second set of 3 push-pull screws until its total runout was less than 35 μm. A centering pin on the cup mated to a centering hole in the attractor guaranteed that the attractor and cup had the same axis.

4.1.2 Screen

We installed the μ-metal screen and checked the attractor-screen capacitance following each round of aligning the attractor. We lowered the overall height of the attractor using the leveling screws until the attractor and screen were not in electrical contact and we adjusted the spring-loaded screen mount [39](p. 75) until we achieved a final attractor-screen capacitance of 150 pF with a 1.4 pF amplitude 1-ω component, as seen in `run4415`. There is about 72 pf of stray capacitance in the cables so this corresponds to an overall separation of about 150 μm. Using the measured attractor tip angle of about 1 mrad relative to the bearing axis, the 1.4 pF 1ω component corresponds to a tip of the screen of about 2 mrad relative to the bearing axis.

4.1.3 Spin Pendulum

4.1.3.1 Leveling

We leveled the pendulum using the technique described in Dan Kapner's Ph. D. thesis [40](p. 29). Briefly, as shown in Figure 4.2, we placed two electrically-isolated semicircular plates, called a split-capacitor, below the spin-pendulum. We gave the pendulum a very large twist amplitude and measured the capacitances between the pendulum and each plate. When the bottom of the pendulum was perpendicular to its suspension axis, the difference in the capacitance measured to each plate does not vary as the pendulum twists. Adjusting

the tension of screws on to a wave-washer sitting between the pendulum top-hat and the mirror cube allowed us to tip the bottom of the pendulum until it was level with the split-capacitor.

We read the split-capacitor in on DAQ channels `diff_quad` and `sum_quad`. With two of the four screws completely tightened, the split capacitor `diff` signal was 250 bits for a full pendulum revolution on a `sum` signal of 610 bits (`run4399`). The top-hat leveling system did not have the range to level the spin- pendulum any further. We measured the residual tilt of the pendulum by placing weights along two orthogonal axes on the pendulum until the `diff` signal was largely nulled. Placing 2 g at a radius of 1.42 cm along the first axis and 3 g at 1.25 cm along the second axis reduced the pendulum tilt by 85%, down to a `diff` signal of 35 bits (`run4410`). Then, by using the mass ($M = 59.8$ g) of the pendulum, the height ($h = 6.82$ cm) of the pendulum suspension point above its center of mass, and the net moment arm ($\ell = 4.7$ g cm) of the weights that leveled the pendulum, we calculated the tilt angle $\theta_{tilt} = \ell/Mh$ of the pendulum with no weights on it to be 11 mrad. This corresponds to a 0.17 mm variation in the average z-position of the spin segments. This variation is our largest mis-alignment, and we neglect it relative to our typical mean separations of ~ 7 mm.

4.1.3.2 Centering

We centered the pendulum in X and Y using our mass attractor to avoid confusion from magnetic effects associated with the spin attractor. We used both the 4-ω signals from the tungsten rod interactions and 10-ω signals from the magnet to copper-wedge interactions for centering. We found the X and Y phi-top position that maximized the gravitational torque on the pendulum by iteratively maximizing along X and then along Y until the process converged. Each scan consisted of 4 to 5 roughly 10000 second-long runs from which we extracted the 4-ω and 10-ω torques. We fit the torques to a parabola against phi-top position to identify the torque-maximizing position of phi-top. This procedure centered the pendulum to within ~ 20 μm of the attractor rotation axis. This is of the same order as the error in aligning the spin and mass attractors to the rotation axis (section 4.1.1.2).

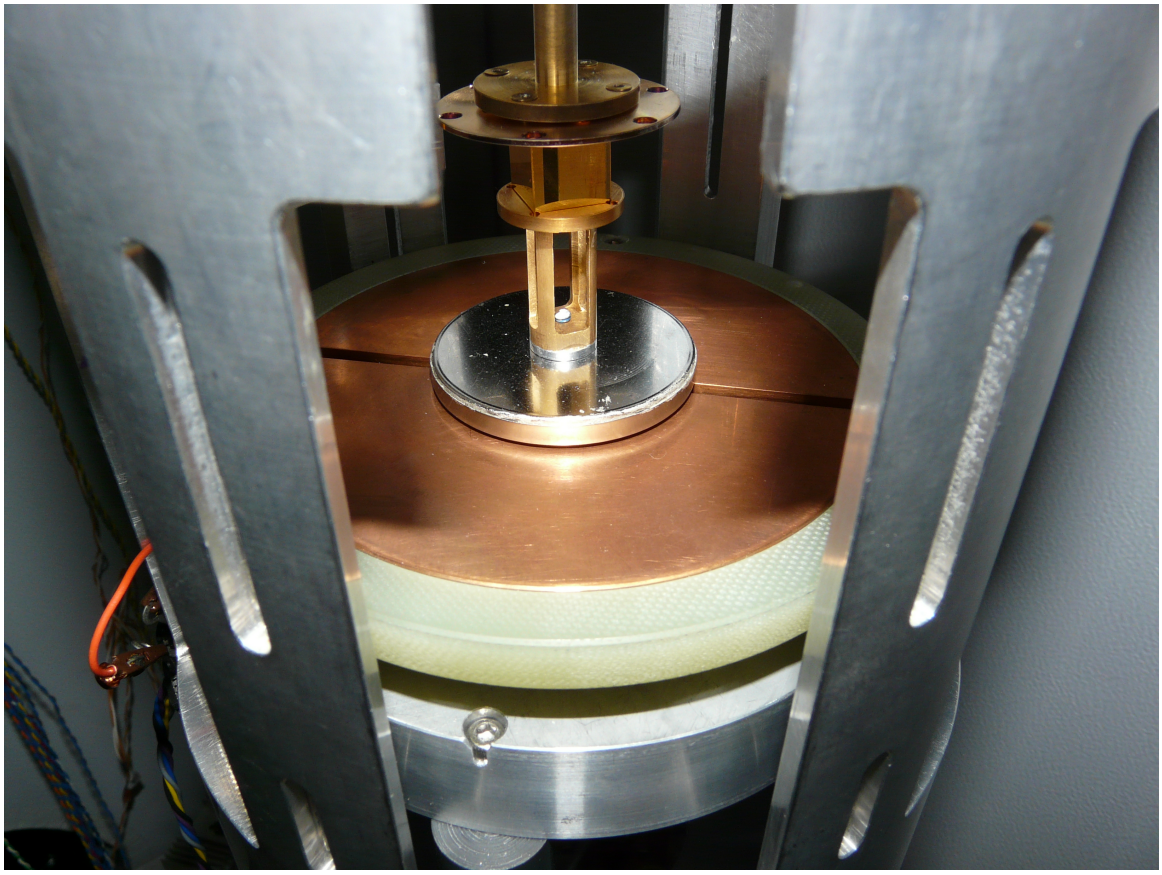

Figure 4.2: Photograph of the pendulum above the split-capacitor. When the bottom of the pendulum is perpendicular to the fiber, the difference in the capacitance measured to each of the plates is independent of the twist angle of the pendulum. The four screws near the top of the pendulum allowed us to tip the bottom of the pendulum relative to its suspension axis.

4.1.4 Determining the Pendulum to Attractor Separation

We determined the distance between the pendulum and attractor by fitting a capacitance scan (consisting of capacitance values measured at a large number of pendulum Z_{mic} positions) to an electrostatic model of the pendulum system. We used a finite-element package implemented in COMSOL to make the electrostatic models of capacitance as a function of pendulum position and a program called `FITCAP32` to fit the idealized electrostatic model to the capacitance scan with adjustable Z-offset, overall normalization, stray capacitance term, and a term proportional to the second derivative of the model that can account for pendulum "bounce" or "tip". The capacitance scan data provided two independent measures of the pendulum-to-screen parallelism, one based on where the edge of the pendulum first touches the screen, which shows up as a slope change in the capacitance scan, and the other derived from the size of the term proportional to the second derivative of the capacitance in the fit of the capacitance scan, called the "bounce" correction in `FITCAP32`. Alternatively, this provides two different options for fitting the capacitance scan: (1) letting the "bounce" correction float to the value giving the best fit to the electrostatic model, or (2) fixing the value of the "bounce" correction based on the estimated tip of the pendulum. We estimated the tip of the pendulum from where the capacitance scan has a kink and set the "bounce correction" as half of the Z distance between the lowest point on the rim of the pendulum and the center its bottom surface, as shown in Figure 4.3.

4.1.4.1 Distance to the Mass Attractor

We established the gravitational-attractor to pendulum separation by mapping Z_{mic} to the pendulum-screen separation and using optical metrology to determine the distance from the top of the screen to the top of the attractor.

Our optical-microscope measurements with an showed that the tops of the tungsten rods were 0.68 mm below the top of the screen, and the top of the copper surface was 1.23 mm below the top of the screen. This 0.55 mm distance between the top of the tungsten and the top of the copper agrees with the 0.51 mm distance that we expected from the difference in copper and tungsten thicknesses (Sec. 3.2.4) to within 40 μm.

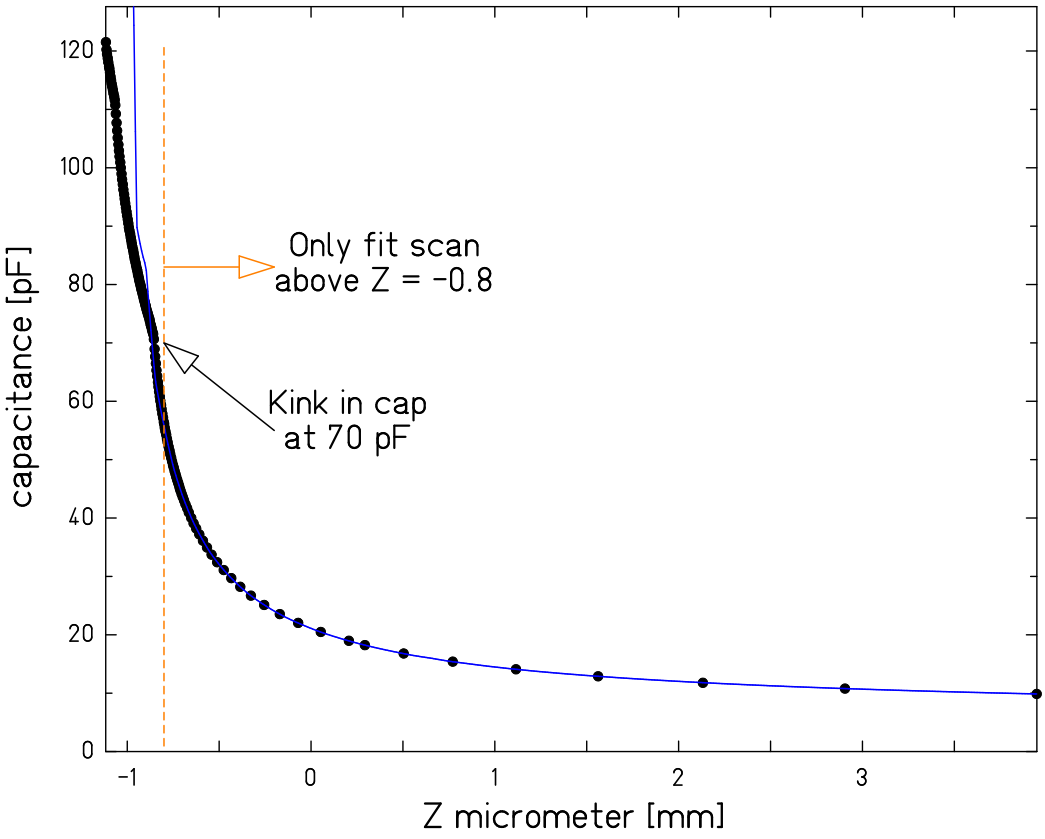

Figure 4.3: A capacitance scan from the pendulum to the attractor. As expected, the capacitance rose as the inverse of the distance between the pendulum and the attractor for large separations. At 58 pF the capacitance had a kink and no longer followed $1/Z$. We interpret this as being the point where the edge of the pendulum touched the attractor. The fit to this capacitance scan told us that at a capacitance of 58 pF the center of the bottom surface of the pendulum was 250 μm above the attractor, so we set the "bounce correction" in `FITCAP32` to half of that, 125 μm.

We fitted the electrostatic model of the pendulum and screen contained in `spfoil.ans` to the capacitance scan `sg1z.dat`. A loss of power reset the $Z_{\rm mic}$ between data-taking and the capacitance scan, so we matched the capacitance measured during each data run to the results of the capacitance fit to find the pendulum-screen separation of that run. The $Z_{\rm mic}$ and measured capacitance of all the various data runs were consistent with each other and the capacitance scan if we used a $Z_{\rm mic}$ + 0.08 mm for the pendulum to screen separation. The pendulum had 0.76 mm of μ-metal shielding on its lower surface, so the distance between the bottom of the magnets to the top of the tungsten was

$$Z_{\rm mic} + 0.68 + 0.08 + 0.76 = Z_{\rm mic} + 1.52\,{\rm mm}$$

and the distance between the bottom of the magnet to top of copper separation

$$Z_{\rm mic} + 1.23 + 0.08 + 0.76 = Z_{\rm mic} + 2.07\,{\rm mm}$$

4.1.4.2 Distance to the Spin-Attractor

We removed the μ-metal screen that normally separates the attractor and the pendulum, and measured the attractor-pendulum capacitance at 41 different pendulum heights. We fitted the capacitance versus Z-micrometer ($Z_{\rm mic}$) data, contained in `attrz.dat`, to the electrostatic model of capacitance versus attractor-pendulum separation contained in `pendattr.ans`. We found that the outer-shields of the pendulum and attractor would touch at $Z_{\rm mic}$ = -0.6 mm.

We determined the actual distance between the spin-rings by adding the total thicknesses of the intervening shields and compensators to the $Z_{\rm mic}$ offset. We found the intervening thickness by adding the measured total thickness of the pendulum and attractor pucks, subtracting the measured thickness of the spin-rings and halving the result. The pendulum shields added 0.77 mm and the attractor assembly added 2.29 mm to the distance between spin-rings, for a total distance between the spin-rings during data-taking of

$$Z_{\rm sep} = Z_{\rm mic} + 3.66\,{\rm mm}$$

4.1.5 Measuring the Free Torsion Constant of the Fiber

We used the calculated rotational moment of the pendulum, $I = 114$ g·cm^2, and its measured free torsional period, T, to find the free torsion constant of the fiber $\kappa = I(2\pi/T)^2$. Appendix B contains details of rotational moment calculation. We extracted the torsional period of the pendulum from data taken with the attractor stationary, as shown in Fig. 4.4. We measured the free torsional period when the pendulum was far from the screen and pendulum-screen interactions were small. Table 4.1 lists the torsion period measured with the pendulum 2.5 mm and 3.2 mm above the screen, showing that at these separations interactions between the pendulum and screen had only a small effect on the torsion constant of the pendulum.

Table 4.1: Measured torsion periods of the Mark I fiber in seconds.

Run	Torsion Period [s]	Capacitance [pF]	Distance above Screen [mm]
4284	197.24 ± 0.01	12.6	2.5
4294	197.14 ± 0.01	11.5	3.2

Our estimate of the free torsion constant from the pendulum's period and moment of inertia was $\kappa = 114\,\mathrm{g\,cm^2}\,(2\pi/197.2\,\mathrm{s})^2 = 0.116$ ergs/rad, in reasonable agreement with the expected value of 0.125 ergs/rad for a typical 1.1 mil fiber.

4.2 Data Taking Procedures

Our data taking, data reduction and analysis procedures were similar to those described in the theses of Dan Kapner [40] and Ted Cook[39]. We measured the twist on the pendulum at a number of different heights above the rotating attractor and analyzed the data in terms of harmonics of the attractor rotation rate.

4.2.1 Data Taking

Before taking data we centered the pendulum on the detector and damped its free torsion amplitude to $\lesssim 2\mu$rad. The attractor turntable rotated at 4141 s/rev, corresponding to

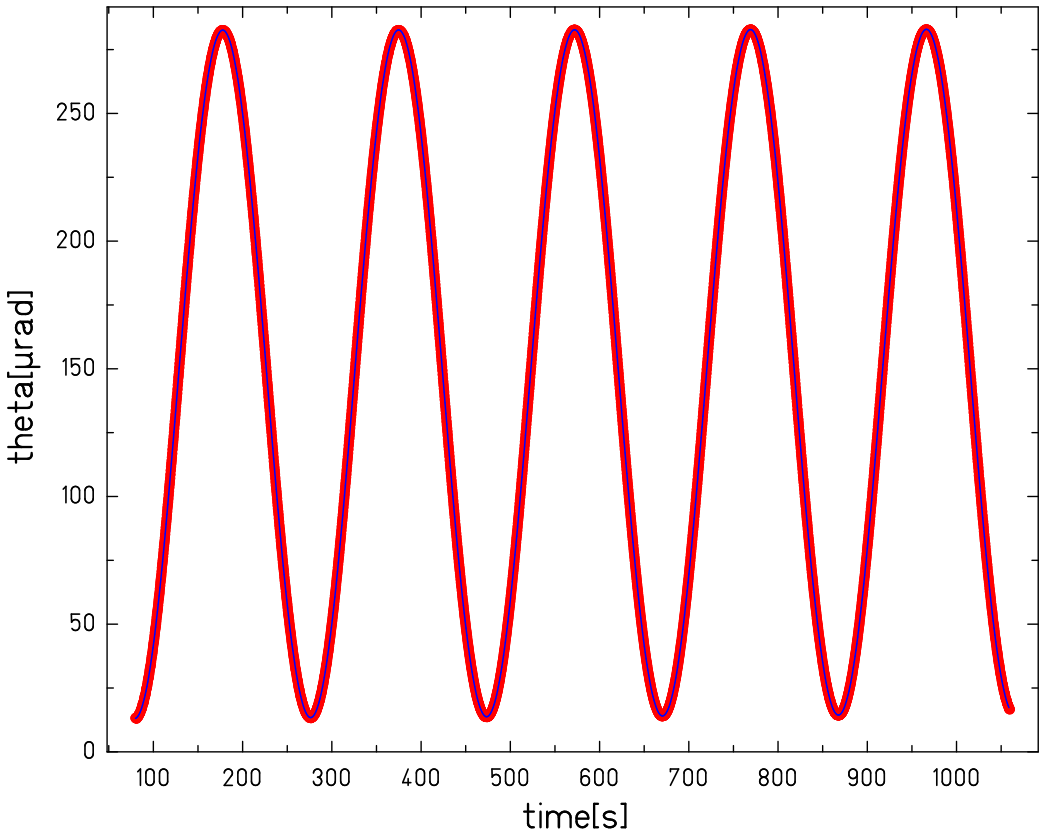

Figure 4.4: A plot of the twist of the pendulum in `run4294` (thick) and a fit to the data (thin). Fitting this data to a sinusoid gave us the torsion period of the pendulum and combined with the moment of inertia, the restoring force on the pendulum. Fitting the residuals of the sinusoid mapped the non-linearities in our read-out system.

21 times the pendulums torsion period. This was as fast as we could reliably hold the turntable rotation-rate in feedback because of excessive friction between the turntable and the spring-loaded push pin that provided electrical contact to the attractor. We read all of our sensors into our Data Acquisition System computer (DAQ) with a sampling period of ∼3.29 seconds, corresponding to exactly 1260 samples per revolution. We recorded the turntable control signal and "once-around marker", 2 AGI tilt meters, a capacitance meter, 10 temperature sensors of which two were in vacuum, and 4 autocollimator signals.

We chopped the laser light in the autocollimator at 141.26 Hz. We took the outputs from the two sides of the split photo-diode monitoring the return position of the laser spot and converted them into sum and difference signals. We fed the sum and difference signals into lock-in amplifiers locked to the same frequency generator that controlled the chopping of the laser light and recorded the in-phase and quadrature components of the sum and difference signals. We call the in-phase sum signal Σ and the in-phase difference signal Δ. We determined the pendulum twist from the Δ/Σ ratio, and corrected the twist conversion for diff-sum feed-thru and detector non-linearities. We mapped the detector response following each data run by taking a short calibration run with the attractor stationary. We gave the pendulum a kick so that its free oscillation covered the same portion of the detector as the data run. Figure 4.4 shows an example of the pendulum twist, $\theta(t)$ during such a run. By assuming $\theta(t)$ was a pure sinusoid plus a linear drift term, we were able to map the non-linearities in our read-out system by fitting $\theta(t)$ with an $\mathcal{O}(\Delta/\Sigma)^3$ polynomial. Calibration runs with significant drift or swing produced unreliable calibrations and were not usable as demonstrated in Figure 4.5.

We extracted the effective torsion constant of the pendulum during each run from the torsional period measured during these calibration runs, and used the effective torsion constant measured after each run to convert the measured pendulum twist into a torque on the pendulum.

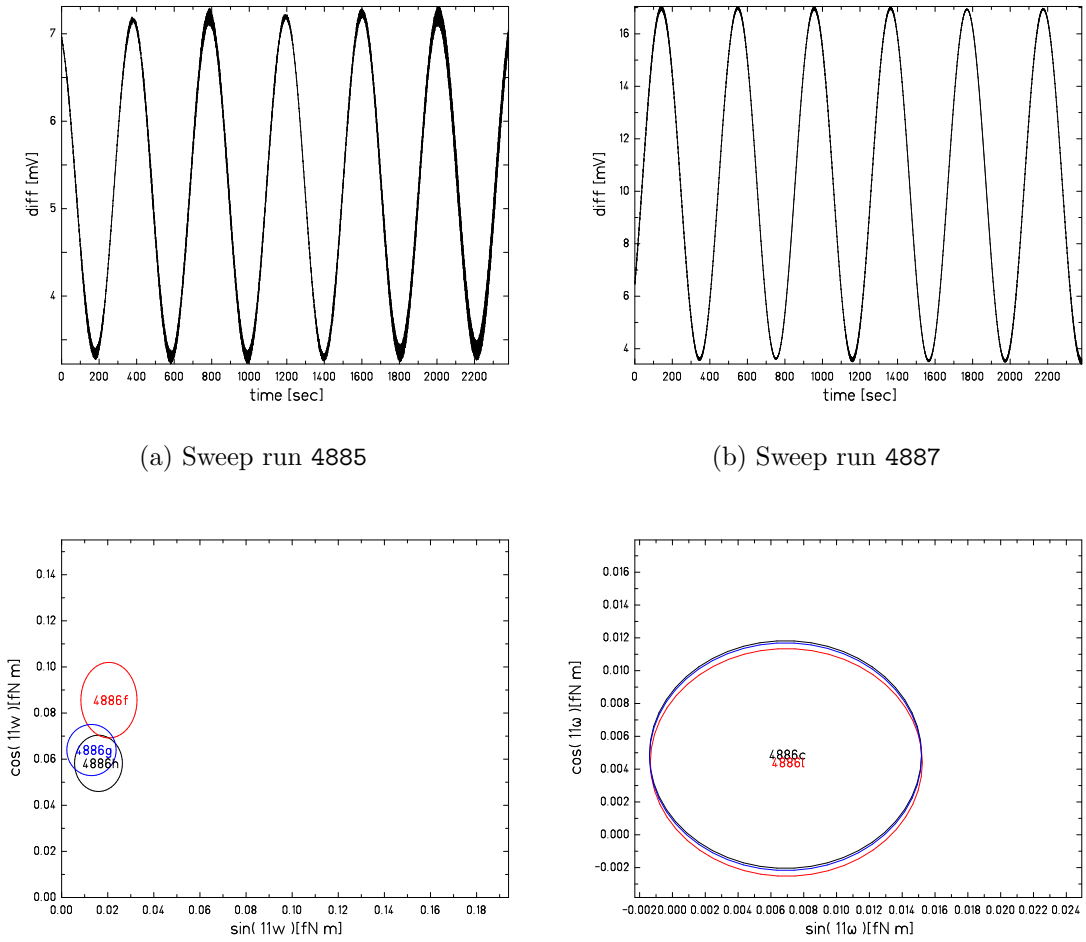

(a) Sweep run 4885

(b) Sweep run 4887

Figure 4.5: The effects of the calibration qualtiy on the 11ω torque extracted from run 4886. The 11ω torque was particularly sensitive to the calibration because detector non-linearities will generate an 11ω signal from the large 4ω gravitational signal and the large 7ω free-torsion oscillation. Upper plots: Sweep run 4885 (Left) was unreliable, as the fitted harmonics of science run 4886 depended on minor changes in how we extracted calibration coefficients from the sweep run. It had a large swing amplitude and covered roughly 75% of the detector used by the data run. The calibrations determined from sweep run 4887 (Right) were much more stable, so we take these to be the correct calibrations. Sweep run 4887 had much less swing and covered twice as much of the detector as the data run. (Bottom) The three fits to the sweep runs consisted of: using a linear drift term and a cubic polynomial in Δ/Σ to (1) fit the entire sweep run; (2) just the first half of the sweep run; and (3) fitting the entire sweep run with a cubic drift term and a quartic polynomial in Δ/Σ.

4.2.2 Data Reduction

We cut our data runs into segments containing exactly one full attractor rotation, very nearly 21 torsion oscillations. We fitted every sensor in each cut to a quadratic drift term plus sines and cosines of the first fourteen harmonics of the turntable rotation rate:

$$s_i(t) = c_0 + c_1 t + c_2 t^2 + \sum_{n=1}^{n=14} \left(a_n \sin(n\omega t) + b_n \cos(n\omega t)\right)$$

We averaged the fitted values of all the cuts from a given run with even weighting and used the variance of the fitted values across the cuts divided by the square root of the number of cuts as the statistical uncertainty. We took the weighted average of all the runs at a given pendulum position to obtain our final results. For analysis we typically converted these Cartesian harmonic components into amplitude and phase $A_n \sin(n\omega t + \delta_n)$ after combining all of the relevant runs. The error bars in quoted in this thesis correspond to 1-σ confidence intervals through-out.

A 4-pt torsion filter removed the drift and free torsion oscillation from our pendulum twist data [39]. Figure 6.4 shows the effect the filter has on our signal frequencies. An attenuation correction applied to the twist data corrected for the effects of the torsion filter, pendulum moment of inertia and electronic time constants on the fitted harmonics of the inferred twist angle.

4.2.2.1 Data Quality Cuts

We checked for bad data by looking for cuts whose fit to the twist datat had anomalously large chi-square per degree of freedom. Our Mark I data contained a total of 203 cuts and our chi-square criteria eliminated 13 consecutive cuts at the beginning of `run4391`.

4.3 Types of Systematic Effects

4.3.1 Gravitational Systematics

Our pendulum and attractors all had mass 20-poles that would induce 10ω gravitational torques on the pendulum at our science frequency. We estimated the magnitude of these by measuring and modeling the mass distribution of our system and using the Fourier-Bessel

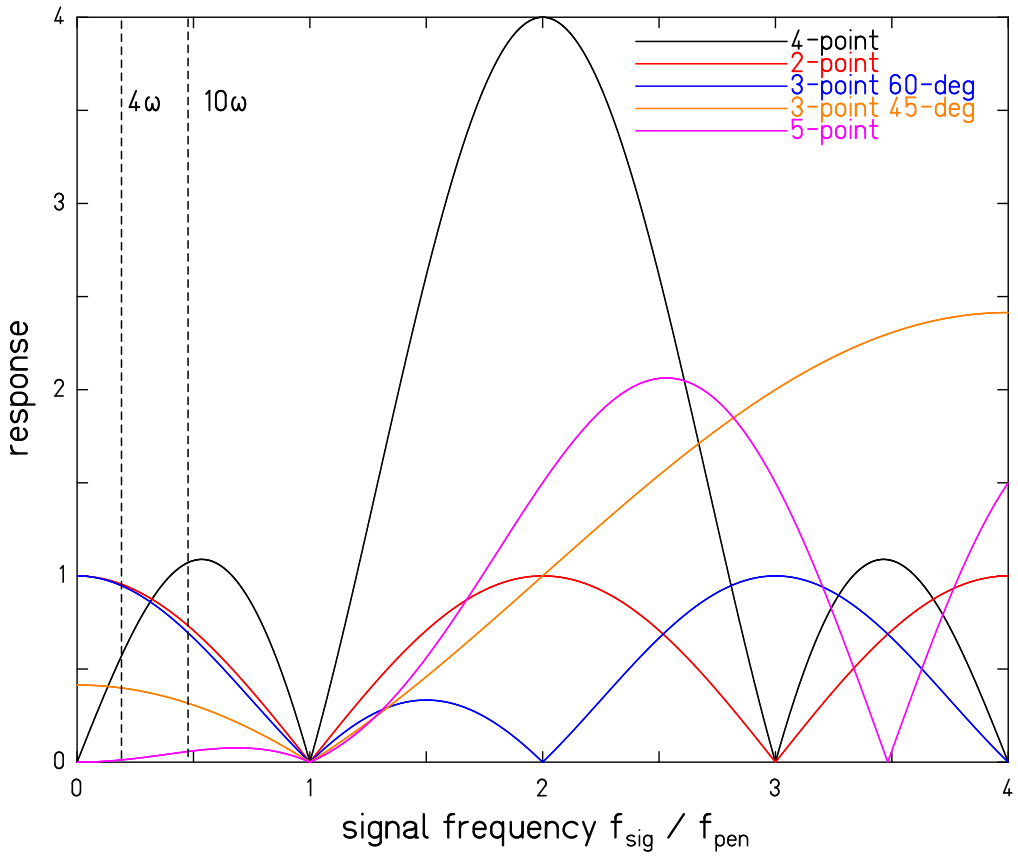

Figure 4.6: Effect of various torsion filters on our signal harmonics, 4ω and 10ω.

expansion to calculate the expected gravitational torques due to each attractor. We checked our calculations against the torques measured using the mass attractor, and at multiple pendulum to attractor distances to separate gravitational torques from other sources of 10ω pendulum twist.

4.3.2 Magnetic Systematics and Broadband Systematics

Residual magnetic fields on the spin-attractor and spin-pendulum could generate magnetic torques on the pendulum correlated with the attractor rotation. The 10ω component of this torque would be at the same frequency as a new spin-spin interaction and constitute an important background. Measurements (described in Section 3.3.3) of the shielded pendulum and attractor showed the leakage field to be fairly constant across all higher ($> 4\omega$) harmonics (see Fig. 4.7).

Apparatus based background effects, such as temperature fluctuations, can also produce twists or apparent twists of the pendulum at a broad range frequencies including the science frequency.

A new spin-signal, in contrast to magnetic and broadband effects, would produce torques only at 10ω and its higher harmonics. We used this feature to estimate the magnetic torque and broadband twist at our science frequency from the measured torques of neighboring harmonics.

Since amplitudes are always positive, data that are sampled from a distribution statistically consistent with zero will still have a non-zero average amplitude. Specifically, if we started from a distribution that has a variance of σ and mean of zero and randomly selected N points we would expect their amplitudes to be

$$< A_{\mathrm{rand}} >= \sigma(\sqrt{\pi/2} \pm 1/\sqrt{N}).$$

We checked if the average amplitude of torques measured at harmonics near 10ω , $A_{\mathrm{high}-\omega}$ was consistent with A_{rand}. If it was, we concluded that the error bars of our measurement sufficiently described systematic contributions to the 10ω torque from sources that would also affect all of the neighboring harmonics. If $A_{\mathrm{high}-\omega}$ was significantly larger than A_{rand},

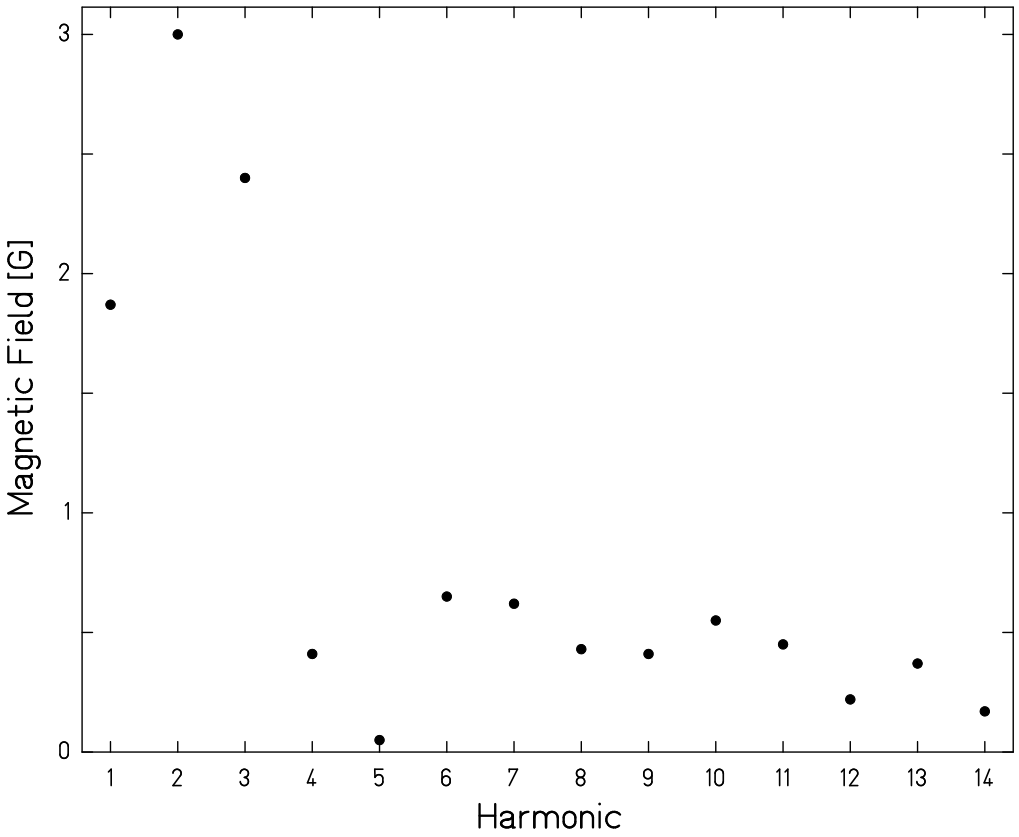

Figure 4.7: Magnetic leakage field outside the pendulum can, showing roughly equal contributions from all high harmonics

then the zero lower-bound on amplitudes has little effect on the central value, and we included a magnetic/broadband systematic equal to $A_{\mathrm{high}-\omega}$.

Chapter 5

RESULTS FROM OUR MARK I EXPERIMENTS

5.1 mass attractor, 2014 Data

5.1.1 Measured Torques

We took data with the pendulum at four different heights above the mass attractor. The distance between the bottom of the pendulum spin-rings and the top of the copper on the attractor, which we call $Z_{\rm sep}$, ranged between 2.26 and 5.29 mm. Table 5.1 contains details about the runs making up this data set. The power spectrum of our closest run, Fig. 5.1, shows that we reached the thermal noise limit of our fiber in these measurements with the 4ω, 10ω and free torsional peaks clearly visible. Table 5.2 lists some of the relevant torque amplitudes extracted from our runs at different pendulum-attractor separations.

5.1.2 Separating Monopole-Dipole and Gravitational Signals

The measured 10ω torque on the pendulum reflected the combined effects of gravitational and monopole-dipole interactions with the mass attractor. To set a limit on a new monopole-dipole interaction we must separate the measured 10ω torque into its gravitational and monopole-dipole components

$$A_{10\omega}e^{i\phi_{10\omega}}e^{i\omega t} = (|A_{\rm g}|e^{i\phi_g} + |A_{\rm s}|e^{i\phi_s})e^{i\omega t} \tag{5.1}$$

where A and ϕ are the amplitude and phase of the signals. The subscripts '10ω' refer to the 10ω measured torques, and the subscripts 'g' and 's' refer to the 10ω gravitational component and monopole-dipole components, respectively.

Fortunately, the $\vec{\sigma}\cdot\vec{r}$ dependence of the monopole-dipole potential (Eq. 1.1) means the monopole-dipole signal always differs in phase by $\pi/2$ in 10-ω space relative to the gravitational signal. When the copper wedges of the mass attractor are directly below the Alnico or $SmCo_5$ wedges on the pendulum (see Figure 5.2), $\vec{\sigma}\cdot\vec{r}$ averages to zero so

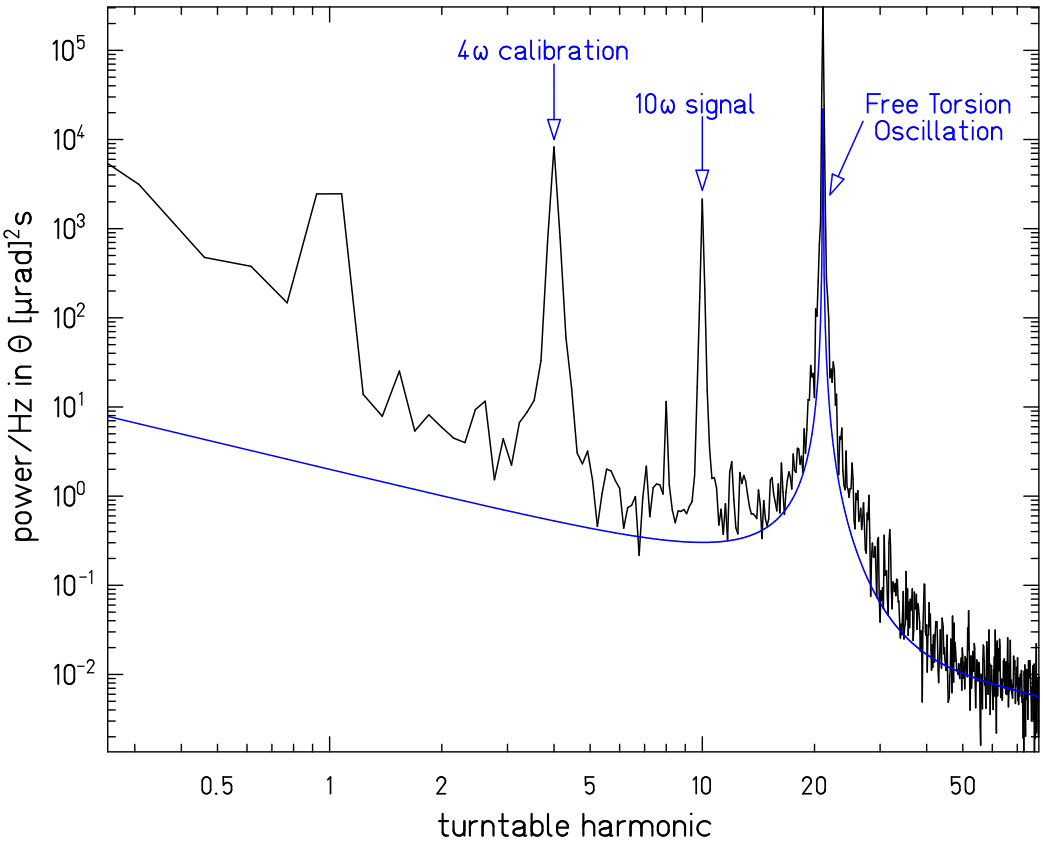

Figure 5.1: Power spectral density of the twist angle from our closest mass attractor data run, with $Z_{\rm sep} = 2.26$mm (`run4387`). The blue line shows the expected thermal noise of a fiber with torsion constant $\kappa = 0.116 \times 10^{-2}$ fN-m/nrad and a quality factor $Q = 800$. The pendulum free torsion frequency was 5.1 mHz.

Table 5.1: Parameters of the runs in the Mark I mass attractor data set. Top: Cap is the capacitance in pF, and all distances are in mm. The final column gives the calculated torque that a monopole-dipole potential with coupling constants $g_p g_s/\hbar c = 1$ would produce at that separation. Bottom: Cuts made to the data set.

Run	Cuts	Cap	Z_{mic}	Z_{screen}	Z_{sep}	Sensitivity
4387	19	53	0.18	0.26	2.25	2.89E+26
4393	17	15	1.64	1.72	3.71	1.12E+26
4389	10	13	2.11	2.19	4.18	8.33E+25
4391	10	10	3.21	3.29	5.28	4.17E+25

Run	Data dropped from run
4387	None, entire run included
4393	Cut everything after 72500 s due to a pendulum kick
4389	None, entire run included
4391	First 13 cuts dropped because of anomalously large χ^2

the monopole-dipole potential vanishes, and the monopole-dipole torque must be at its maximum. At the same attractor angle, the gravitational torque is zero by symmetry. This phase difference appears in the Fourier-Bessel expansion as the additional factor of i on the monopole-dipole integral in Eq. 2.7 and corresponds to $\delta = \pi/2 \times 1/10 = 9^\circ$ for $m = 10$. Thus, as long as we know the relative orientations of the mass attractor and the spin pendulum as a function of time, we can completely separate the measured 10ω torque into its gravitational and monopole-dipole components.

We established the relative phases of the mass attractor and the spin pendulum from the phase of the purely gravitational 4ω signal. Naturally, this approach only can only determine the attractor phase to within 90°. Since the 10ω signal repeats every 36°, the phase of the 4ω signal determines the phase of the 10ω signal, up to a sign ambiguity corresponding to a

Table 5.2: Some of the torques measured on the pendulum from the Mark I mass attractor data set. Top: Torques relevant to constraining monopole-dipole interactions and verifying the torque calibration of our data. Bottom: Torques relevant for comparing with spin attractor data on spurious, potentially magnetic, torques on the pendulum. Torque amplitudes are in fN-m. $A_{\text{high-}\omega}$ was the average of the 7, 11, 13, and 14ω torques. A_{rand} is what we expect for $A_{\text{high-}\omega}$ from statistical scatter alone.

Run	Z_{sep}	$A_{4\omega}$	$\phi_{4\omega}$	$A_{10\omega}$	$\phi_{10\omega}$
4387	2.25	9.581 ± 0.074	76.62 ± 0.12	3.937 ± 0.028	4.56 ± 0.04
4393	3.71	3.962 ± 0.063	76.79 ± 0.22	1.549 ± 0.018	4.40 ± 0.07
4389	4.18	3.037 ± 0.034	76.49 ± 0.18	1.199 ± 0.019	4.65 ± 0.1
4391	5.28	1.782 ± 0.035	76.52 ± 0.24	0.627 ± 0.210	4.26 ± 0.19

Run	Z_{sep}	$A_{1\omega}$	$A_{\text{high-}\omega}$	A_{rand}
4387	2.25	7.06 ± 0.83	0.026 ± 0.013	0.033
4393	3.71	1.25 ± 0.91	0.016 ± 0.006	0.015
4389	4.18	1.54 ± 0.22	0.009 ± 0.005	0.013
4391	5.28	0.86 ± 0.38	0.023 ± 0.008	0.020

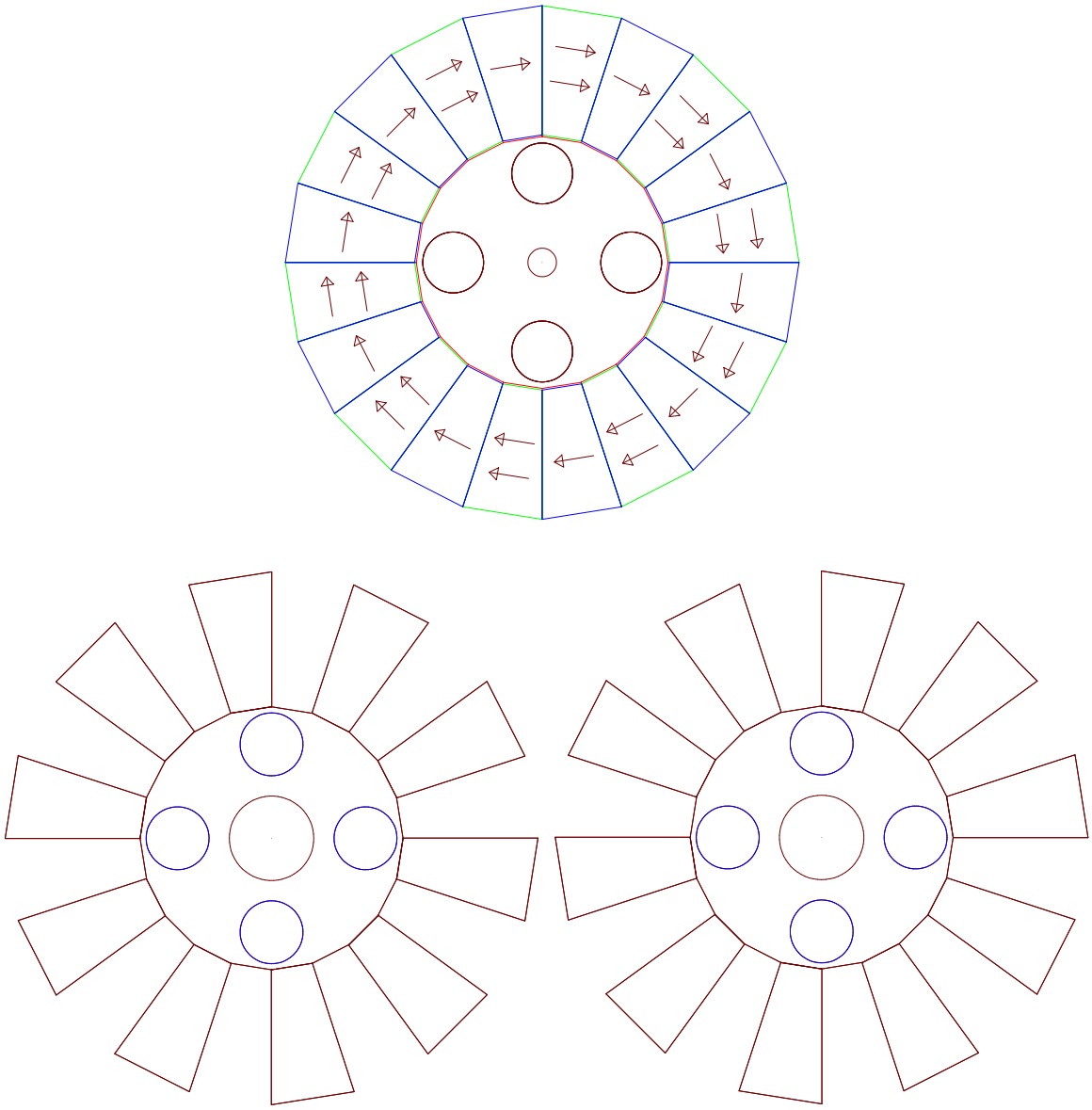

Figure 5.2: Above: Top view of the spin-ring, centering-fixture and tungsten calibration rods. Arrows indicate the spin content of the Alnico (green) and $SmCo_5$ (blue) magnets. Below: The left and right sketches of the mass attractor show the two orientations that have the same 4ω gravitational phase but opposite 10ω phases.

90° rotation of the attractor. Rotating the attractor 90° relative to the pendulum leaves the phase of the 4ω signal unchanged but shifts the 10ω phase by $90° \mod 36° = 18°$, which is the same as a sign change for a signal that repeats every 36°. Figure 5.2 helps to show this.

5.1.2.1 Formulas for the Monopole-Dipole and Gravitational Amplitudes

We measured $A_{10\omega}$ and $\phi_{10\omega}$ in our experiment, and found ϕ_g and ϕ_s from the measured phase of the 4ω gravitational torque, ϕ_4, using the expressions

$$\phi_g = \phi_4 \mod \pi/10 \tag{5.2}$$

$$\phi_s = \phi_g + \pi/(2 \cdot 10) \tag{5.3}$$

We now work out the formulas needed to determine $||A_{\rm g}||$ and $|A_{\rm s}|$ and their uncertainties such that they satisfy Eq. 5.1. Using phasor addition formulas, we can write the difference between the measured 10ω phase $\phi_{10\omega}$ and the expected gravitational phase ϕ_g as:

$$\zeta \equiv \phi_{10\omega} - \phi_g = \arctan\left(\frac{|A_{\rm s}|\sin(\delta)}{|A_{\rm g}| + |A_{\rm s}|\cos(\delta)}\right) \tag{5.4}$$

where once again $\delta = \pi/2 \times 1/10 = 9°$ is the expected phase difference between the gravitational and monopole-dipole signals. This becomes

$$|A_{\rm s}| = \frac{|A_{\rm g}|\tan(\zeta)}{\sin(\delta) - \tan(\zeta)\cos(\delta)} \equiv |A_{\rm g}|R(\zeta) \tag{5.5}$$

where the ratio of $R = |A_{\rm s}|/|A_{\rm g}|$ depends only on the measured value ζ.

Next we substitute $R = |A_{\rm s}|/|A_{\rm g}|$ into the formula for amplitude addition

$$A_{10\omega} = \sqrt{(A_{\rm g}^2 + A_{\rm s}^2 + 2|A_{\rm g}||A_{\rm s}|\cos(\delta))} \tag{5.6}$$

to find

$$|A_{\rm s}| = \frac{A_{10\omega}R}{\sqrt{1 + 2\cos(\delta)\,R + R^2}}. \tag{5.7}$$

If the gravitational signal is much larger than the monopole-dipole signal, ζ will be small and Eq. 5.7 reduces to

$$|A_{\rm s}| = A_{10\omega}\frac{\tan(\zeta)}{\sin(\delta)}. \tag{5.8}$$

If the symmetry number m is large, as it is in our case, δ is small as well and we arrive at the intuitive results

$$|A_{\rm s}| \approx A_{10\omega}\frac{\zeta}{\delta} \tag{5.9}$$

$$|A_{\rm g}| \approx A_{10\omega}\left(1-\frac{\zeta}{\delta}\right). \tag{5.10}$$

5.1.2.2 Formulas for the Monopole-Dipole and Gravitational Uncertainties

$|A_{\rm s}|$ depends on ζ and $A_{10\omega}$ and the uncertainty $\sigma_{A_{\rm s}}$ depends in turn on σ_ζ and $\sigma_{A_{10\omega}}$:

$$\sigma^2_{A_{\rm s}} = \left(\frac{\delta A_{\rm s}}{\delta R}\frac{\delta R}{\delta \zeta}\right)^2\left(\sigma^2_\zeta\right) + \left(\frac{\delta A_{\rm s}}{\delta A_{10\omega}}\right)^2\sigma^2_{A_{10\omega}} \tag{5.11}$$

ζ depends on $\phi_{10\omega}$ and ϕ_g, with ϕ_g depending on ϕ_4 and any uncertainty in the alignment of the spin-ring relative to the tungsten rods, which we call σ_{mis}.

From all sources, the error in ζ is then :

$$\sigma^2_\zeta = \sigma^2_{\phi_{10}} + \sigma^2_{\phi_4} + \sigma^2_{mis} \tag{5.12}$$

We define $u(R) \equiv \sqrt{1+2\cos(\delta)\,R+R^2}$ to simplify some of the expressions, and find the differentials needed to compute the uncertainty in $|A_{\rm s}|$:

$$\frac{\delta A_{\rm s}}{\delta R} = A_{10\omega}\left(\frac{1}{u(R)} - \frac{R(\cos(\delta)+R)}{u(R)^3}\right) \tag{5.13}$$

$$\frac{\delta R}{\delta \zeta} = \frac{\sec^2\zeta\sin(\delta)}{(\sin(\delta)-\tan\zeta\cos(\delta))^2} \tag{5.14}$$

$$\frac{\delta A_{\rm s}}{\delta A_{10\omega}} = \frac{R}{u(R)} \tag{5.15}$$

Using the same approximations $\zeta \ll \delta \ll \pi$ we have a simplified formula for the uncertainty in $|A_{\rm s}|$

$$\sigma^2_{A_{\rm s}} \approx \left(\frac{A_{10\omega}}{\delta}\right)^2\left(\sigma^2_\zeta\right) + \left(\frac{\zeta}{\delta}\right)^2\sigma^2_{A_{10\omega}} \tag{5.16}$$

and for $|A_{\rm g}|$

$$\sigma^2_{|A_{\rm g}|} \approx \left(\frac{A_{10\omega}}{\delta}\right)^2\left(\sigma^2_\zeta\right) + \sigma^2_{A_{10\omega}} \tag{5.17}$$

.

Our experiments find very small monopole-dipole interactions, so these approximate expressions are quite accurate.

5.1.3 Systematic Uncertainties

5.1.3.1 Magnetic and Broadband Systematics

The average amplitude of the 7ω, 11ω, 13ω and 14ω torques, which we called $A_{\mathrm{high}-\omega}$, was consistent with their scatter, A_{rand}, as the final two columns of the lower part of Table 5.2 show. We conclude there was no sign of magnetic or broadband systematics in Mark I mass attractor data.

5.1.3.2 Gravitational Systematics

Our largest source of error in $|A_{\mathrm{s}}|$ was not knowing exactly what phase, ϕ_g, the gravitational component of the 10ω signal *should* have been. If the alignment of the spin-ring on the centering-post were not perfect, the gravitational 10ω signal would be slightly shifted relative to the 4ω signal and ϕ_g would be incorrectly determined, producing an apparent $\vec{\sigma}\cdot\vec{r}$ signal.

To quantify the uncertainty in this alignment, we mounted the centering-post under the smartscope with the spin-ring rotated as far counterclockwise as possible and measured the angle between the spin-ring and the tungsten rods and then rotated the spin-ring as far clockwise as possible on the centering-post and measured the angle again. From this we found that the spin-ring can rotate by $\sigma_{mis} = \pm 0.17^{\circ}$ from its correctly aligned position. Alignment uncertainty between the spin-ring and the tungsten rods, σ_{mis}, and uncertainty in the measured 4ω phase, σ_{ϕ_4}, contributed similar amounts to the uncertainty in ϕ_g. For our closest data set, σ_{mis} and σ_{ϕ_4} contributed roughly 64% and 32% of the total variance of A_{s}, respectively.

5.1.4 Extracted Monopole-Dipole and Gravitational Signals

Table 5.3 gives the measured values needed to separate the measured 10ω torque into its gravitational and monopole-dipole components, along with the gravitational and monopole-

dipole amplitudes, $|A_g|$ and $|A_s|$, and their uncertainties.

Table 5.3: Separation of the 10-ω signal into gravitational and monopole-dipole components. Z_{sep} is in millimeters and all amplitudes and errors are in fN-m.

Run	$A_{10\omega}$	$\phi_{10\omega}$	ϕ_g	σ_{mis}	$\|A_g\|$	$\|A_s\|$
4387	3.937 ± 0.028	4.56 ± 0.04	4.62 ± 0.12	0.17	3.963 ± 0.097	0.026 ± 0.093
4393	1.549 ± 0.018	4.40 ± 0.07	4.79 ± 0.22	0.17	1.616 ± 0.053	0.067 ± 0.050
4389	1.199 ± 0.019	4.65 ± 0.10	4.49 ± 0.18	0.17	1.178 ± 0.040	0.021 ± 0.036
4391	0.627 ± 0.210	4.26 ± 0.19	4.52 ± 0.24	0.17	0.645 ± 0.211	0.018 ± 0.024

5.1.5 Comparison of Measured and Calculated Gravitational Torques

We validated our torque calculations by comparing the measured 4ω and 10ω gravitational torques with those we calculated using our Fourier-Bessel models (Section 2.5) of the pendulum and attractor. Figure 5.3 shows the agreement between our calculated and measured torques. The fit had no free parameters: we used independently measured values for the pendulum-attractor separation (Section 4.1.4.1); torsional spring constant (Section 4.1.5); and masses of the pendulum and attractor components (Section 3.3.2) to calculate the gravitaional torque on the pendulum. Allowing the pendulum-attractor separation to float, the best fit value of Z_0 was 0.52±.01 mm closer for the 4ω data than for the 10ω data, in good agreement with our mechanical measurements (see Section 3.2.4) of how far the tungsten rods extended above the copper attactor.

5.1.6 Constraints on Monopole-Dipole Interactions

The 10ω torques measured at our closest pendulum-attractor separation provided essentially all of our power to constrain new monopole-dipole interactions because the potential (Eq. 1.1) falls off as $1/r^2$ while the potential of our dominant systematic, gravity, falls off only as $1/r$. The final two columns of Table 5.3 show how much more quickly our sensitivity to a

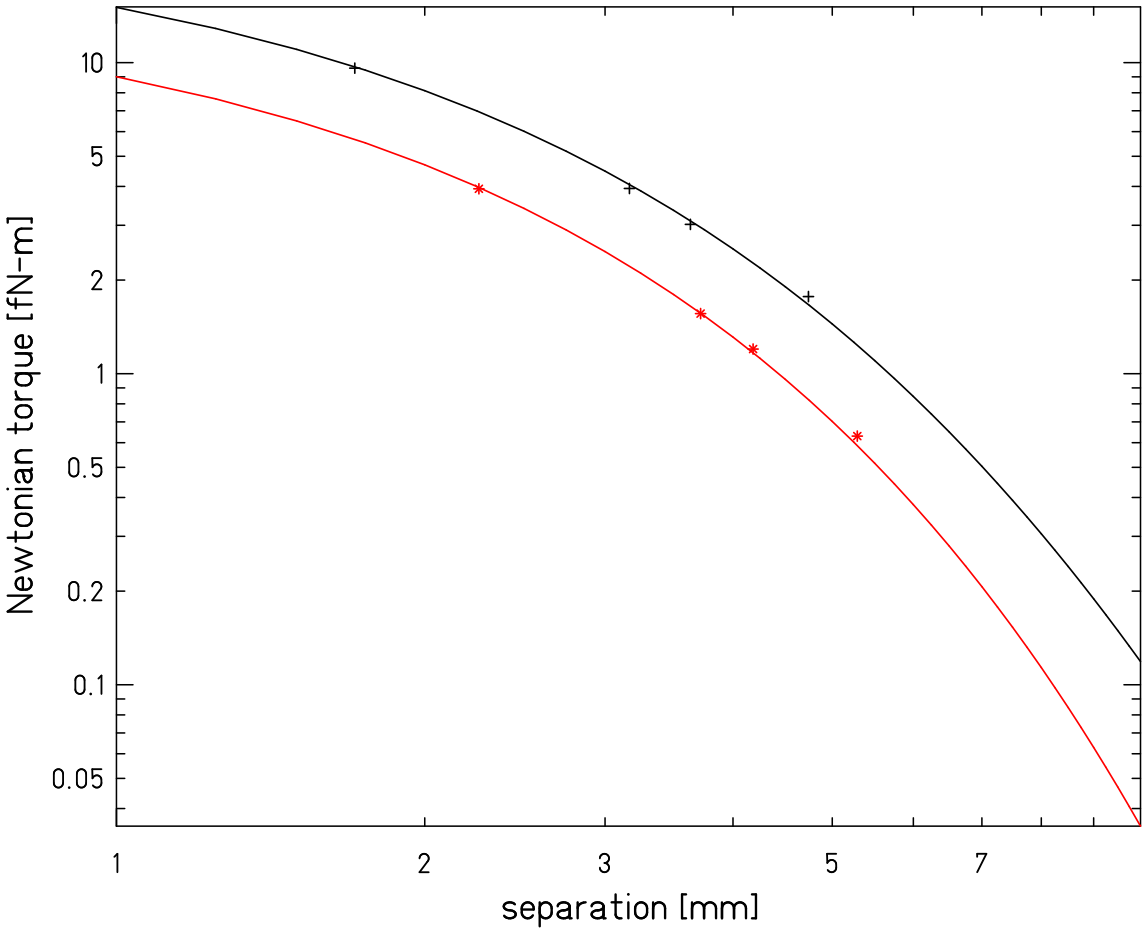

Figure 5.3: Fourier-Bessel calculations of the expected gravitational torques along with the observed torques. The upper (black) line and the crosses are the 4ω torques and the calculation of the tungsten rods in `tn1rods.fbi`. The lower (red) line and the stars are the 10ω torques and the calculations of the copper attractor in `cattr.fbi`

new monopole-dipole interaction (last column) drops compared to our ability to confidently rule out a monopole-dipole torque on the pendulum (2^{nd} to last column).

We used the Fourier-Bessel expansion to calculate the expected monopole-dipole interaction at a pendulum-attractor separation of 2.26 mm for a variety of Yukawa lengths. Figure 5.4 shows the constraints derived from requiring that the magnitude of the torque applied to the pendulum by a new monopole-dipole interaction not exceed 9.6×10^{-2}fN-m, at 68% confidence, which improves limits on a new monopole-dipole interaction for all boson masses between ~ 10 and $250\,\mu$eV.

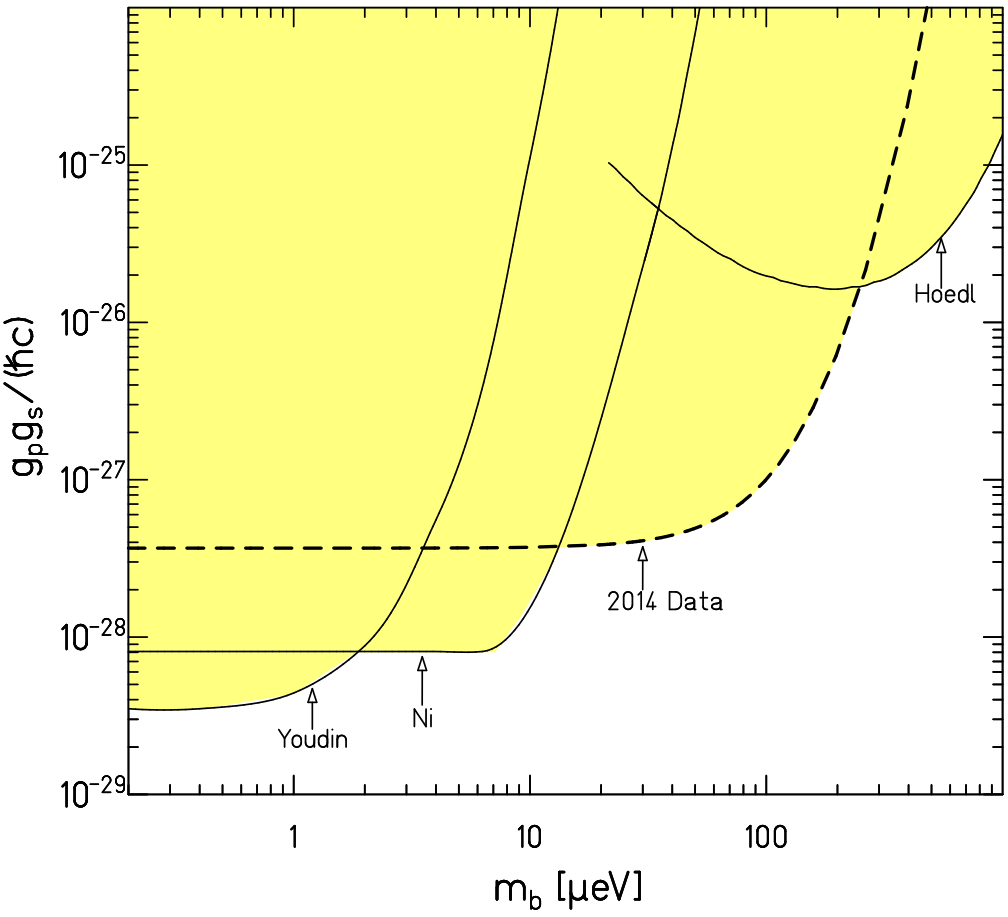

Figure 5.4: Constraints on short-range monopole-dipole interactions derived from the Mark I mass attractor data.

5.2 Mark I Spin Attractor Data Set

5.2.1 Measured Torques

We took data with the pendulum at three different heights above the spin-attractor corresponding to $Z_{\rm sep}$ distances of 6.1 mm, 6.9 mm and 7.6 mm between the top of the attractor magnet ring and bottom of the pendulum ring. Table 5.4 summarizes the data taken at each $Z_{\rm sep}$. The power spectrum, in Figure 5.5, of a run taken at our smallest $Z_{\rm sep}$ shows that we achieved the thermal noise limit of our fiber at frequencies above 6 times the rotation frequency. Tungsten fibers typically have Q-factors of ~ 3000 while we observed a Q of 600. We attribute the smaller Q of our system to magnetic eddy-current damping of the motion of the magnetic pendulum above the conducting μ-metal screen.

The complete data set at $Z_{\rm sep} = 6.1$ mm consisted of 4 days worth of data cut into 94 segments for a total uncertainty of $\sim 1 \times 10^{-2}$ fN-m on the harmonics above 6ω.

5.2.2 Systematic Errors

5.2.2.1 Gravitational Systematics

The expected gravitational torque on the pendulum at 6.1 mm was $\sim 3\times$ below our torque sensitivity (Section 3.2.3). We validated our calculations with the mass attractor data (see Section 5.1.5. Figure 5.3 shows the quality of the match between our data and the calculations. Given how well our calculations of the expected torques from the mass attractor matched our data and how insensitive the compensation quality was to a possible misalignment of the compensators (Appendix A.1) we rely on our calculations of the gravitational torque on the pendulum to assign the gravitational systematics given in Table 5.5.

5.2.2.2 Magnetic and Broadband Systematics

We used the average of the observed 7ω, 11ω, 13ω and 14ω signals to estimate the magnetic contamination at 10ω . We omitted the 6ω, 8ω, 9ω and 12ω components because there were 3,4 and 6-fold structures in the apparatus containing the spin-rings. Including all of the harmonics above 7ω would given the same estimate of the magnetic background. Figure

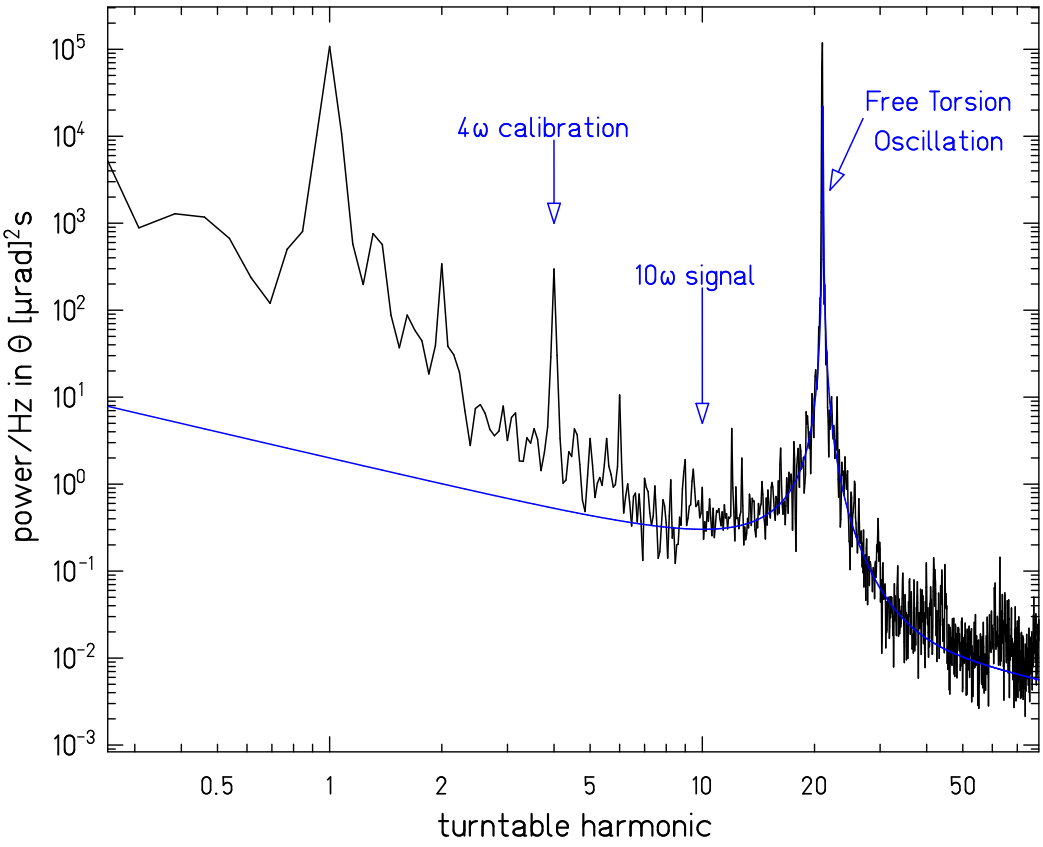

Figure 5.5: Power spectral density of the angle data from one of our closest spin attractor data runs (`run4421`). The black line shows the expected thermal noise from a fiber with $\kappa = 0.116 \times 10^{-2}$ fN-m/nrad and $Q = 600$. We chose this value of Q to match the width of the free torsion peak

Table 5.4: Summary of the Mark I spin attractor data set. Cap is the capacitance in pF and Z_{sep} is the separation between the pendulum and attractor in mm. High ω is the average of the 7, 11, 13, and 14ω signals. All signals and sensitivities are given in torques measured in fN-m. Uncertainties on the 1ω measurements are of order 1%.

Runs	File	Cuts	Cap	Z_{sep}	$A_{1\omega}$	$A_{10\omega} \cdot 10^3$	$A_{\text{high}-\omega} \cdot 10^3$	$A_{\text{rand}} \cdot 10^3$
4419-21	`close`	94	45	6.1	24.1 ± 0.4	8.9 ± 9.1	24.0 ± 4.5	11.3
4425-26	`mid`	26	20	6.9	12.7 ± 0.2	4.1 ± 17.2	19.2 ± 5.2	13.0
4422-23	`far`	27	15	7.6	8.3 ± 0.2	15.9 ± 11.8	18.6 ± 4.6	11.5

Run	Data dropped from run
4419	Cut everything after 90000 s, motor feed back lost
4420	Cut everything after 144000 s, motor feed back lost
4421	None, entire run included
4422	None, entire run included
4423	Cut everything after 29000 s, motor feed back lost
4425	Cut everything after 26000 s, motor feed back lost
4426	None, entire run included

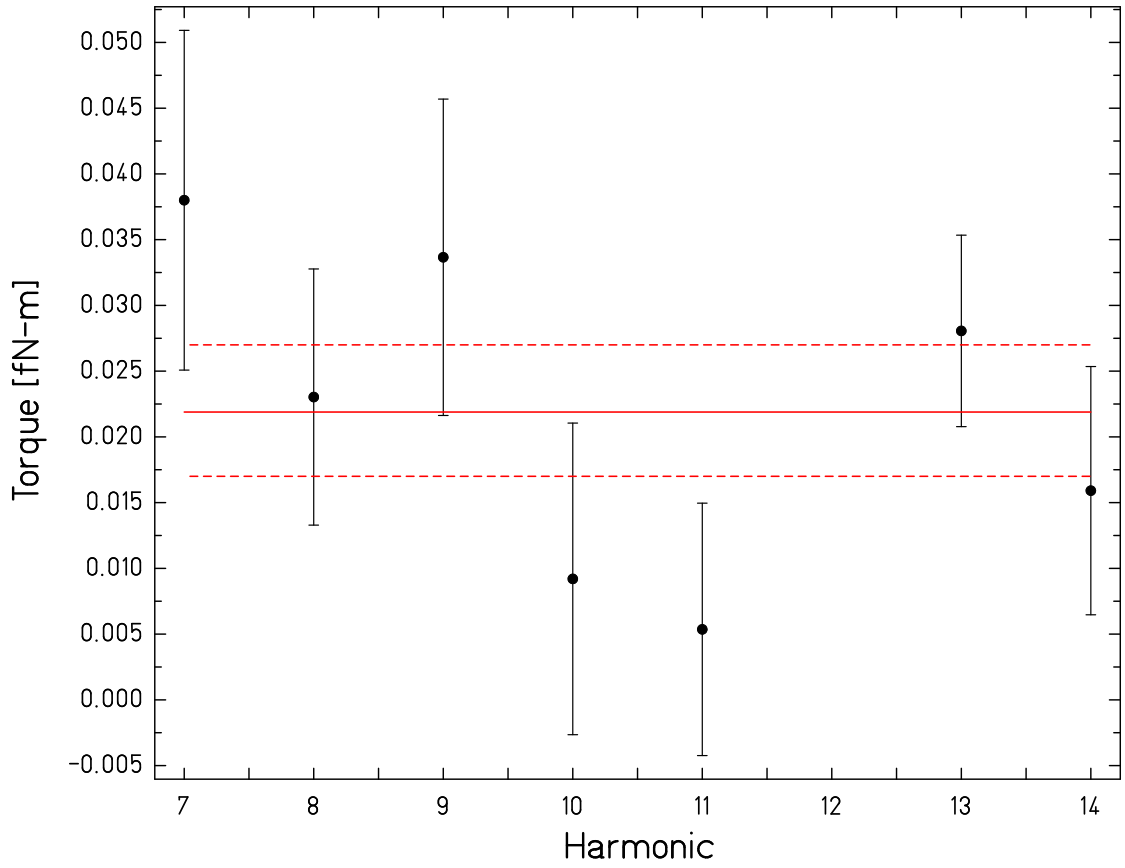

Figure 5.6: Torques measured at harmonics close to our 10ω science signal. These data came from our closest data run with the Mark I spin attractor. The red line is our estimate of the magnetic background from the measured 7, 11, 13 and 14ω torques.

5.6 shows the torques observed at the relevant harmonics in our closest data run. Table 5.4 gives the average amplitudes $A_{\text{high}-\omega}$ and the expected average amplitude from scatter A_{rand}. There was clearly a systematic background at 10ω . Since we saw no background in the Mark I mass attractor data, the background was presumably magnetic in origin. Table 5.5 gives the estimated 10ω magnetic contamination, taken to be

$$\sigma_{\text{mag}} = A_{\text{high}-\omega}.$$

Table 5.5: Error table for Mark I constraints on a new dipole-dipole interaction. $Z_{\rm sep}$ is in mm. All signals and sensitivities are torques measured in fN-m.

Runs	$Z_{\rm sep}$	$A_{10\omega}$	Stat. Error	Mag. Sys.	Grav. Sys.	Total Error
4419-21	6.1	$8.9 \cdot 10^{-3}$	$9.1 \cdot 10^{-3}$	$24.0 \cdot 10^{-3}$	$2.1 \cdot 10^{-3}$	$25.8 \cdot 10^{-3}$
4425-26	6.9	$4.1 \cdot 10^{-3}$	$17.2 \cdot 10^{-3}$	$19.2 \cdot 10^{-3}$	$1.5 \cdot 10^{-3}$	$25.9 \cdot 10^{-3}$
4422-23	7.6	$15.9 \cdot 10^{-3}$	$11.8 \cdot 10^{-3}$	$18.6 \cdot 10^{-3}$	$1.1 \cdot 10^{-3}$	$22.1 \cdot 10^{-3}$

5.2.3 Constraints on Dipole-Dipole Interactions

The rapid $1/r^3$ fall-off of the dipole-dipole potential (Eq. 1.2) meant that our sensitivity to new dipole interactions came entirely from the data taken at 6.1 mm, with the other data providing checks for systematics. We used the Fourier-Bessel expansion to calculate the expected dipole-dipole interaction at a pendulum-attractor separation of 6.1 mm for a variety of dipole-dipole Yukawa lengths. From Table 5.5 we take our measurement of the 10ω torque at 6.1 mm to be

$$\tau_{10\omega} = 8.9 \pm 25.8 \text{aN-m}$$

. There is a sign ambiguity in our data, discussed in more detail in Section 5.1.2, so we conclude at 68% confidence that a new dipole-dipole interaction can only apply torques of less than 27.3 aN-m on our pendulum. Figure 5.7 shows the resulting constraints on $g_{\rm p}^2$, probing for the first time exchange boson masses of up to $\sim 500\mu$eV.

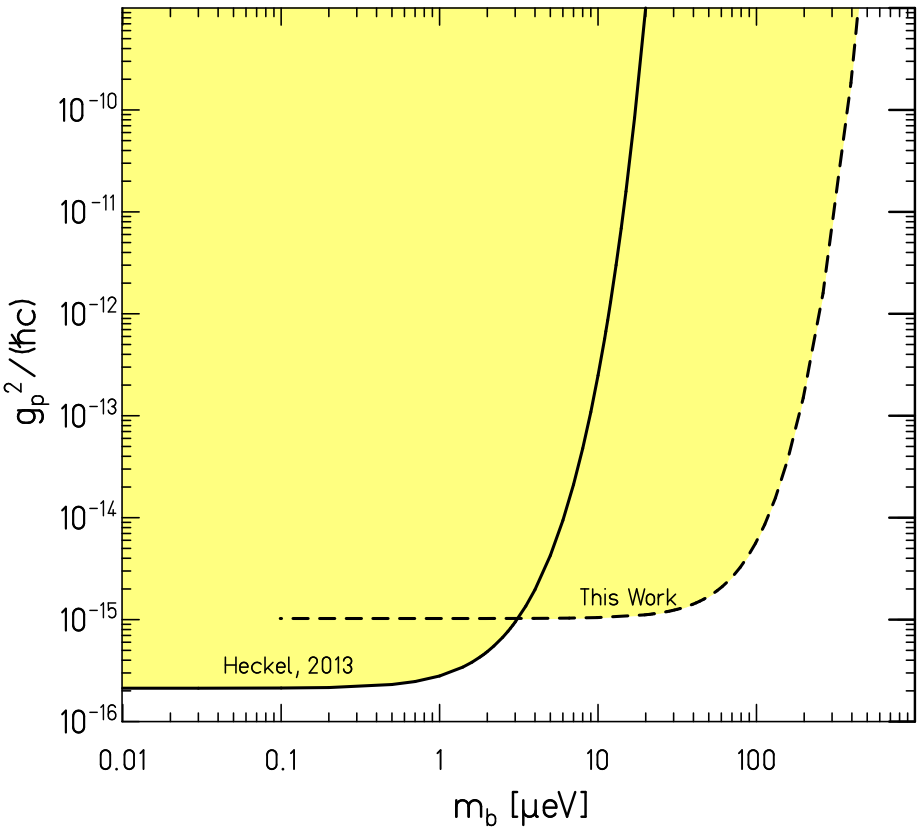

Figure 5.7: Constraints on a new short range dipole-dipole interaction derived from our closest Mark I spin attractor data.

Chapter 6

THE MARK II INSTRUMENT

6.1 Upgrades

We have upgraded the spin pendulum and the spin attractor as well as other parts of the apparatus to reach significantly greater sensitivities to dipole-dipole and monopole-dipole interactions using the existing spin-rings. The upgrades consisted of improving the magnetic shielding of the pendulum and the attractor; increasing the torque sensitivity of the instrument; improving the gravitational compensation system; and reaching smaller separations between the pendulum and attractor.

The specific changes we made in the course of these upgrades were:

- Using nested μ-metal cans on the attractor and pendulum.
- Adding a μ-metal enclosure around the attractor turntable.
- Using a thinner, 20 μm diameter torsion fiber.
- Reducing friction in the attractor rotation system to allow higher frequency operation.
- Gravitationally compensating both the attractor and pendulum
- Eliminating the compensation alignment disks
- Removing the tungsten rods from the mass attractor to simplify the gravitational model
- Using thinner μ-metal sheets and spacers in the screen separating the pendulum and spin attractor

As a side effect of our changes, the moment of inertia, I, of the pendulum increased to $134\,\mathrm{g\ cm^2}$.

6.1.1 Improvements to the Magnetic Isolation of the Pendulum

6.1.1.1 Nested Cans

The success of the multi-layered screen in reducing the magnetic feed-thru from the attractor to the pendulum, discussed in Section 3.5.1, led us to replace the 0.76 mm thick μ-metal cans enclosing the attractor and pendulum with two 0.25 mm μ-metal thick cans nested inside one another with a 25 μm thick aluminum spacer between them. The outer diameter of the outer can was 4.66 cm. Figure 6.1 shows a photograph of the upper halves of the two pendulum cans. The walls of these cans were too thin to be turned down on a lathe for a tight fit, as we did with the previous μ-metal cans. Instead the instrument makers formed the two halves onto separate dies with fit as closely as possible. The fit between the two halves of the cans was not as tight as before but the nested cans still provided a significant improvement in shielding the rings. The measured leakage fields of the rings, shown in Figure 6.2, were $\gtrsim 15$ times smaller outside the nested cans than outside the solid cans, even though the nested cans contained less μ-metal and were slimmer than the solid cans.

6.1.1.2 Shielding the Sides of the Attractor Turntable

The magnetic leakage fields of the attractor can torque the pendulum either by passing through the multi-layered μ-metal screen separating them or by leaking around the sides of the screen and through openings in the μ-metal house that surrounded the pendulum. We made a 13.34 cm diameter, 0.76 mm thick μ-metal cylinder that encloses the attractor turntable and fits tightly inside the swaged over rim of the multi-layer μ-metal screen. Figure 6.3 shows a photograph of the enclosure, which should greatly reduce the magnetic field leakage around the edges of the screen.

Figure 6.1: Photograph showing the top half of the Mark II pendulum cans, sitting nested inside one another.

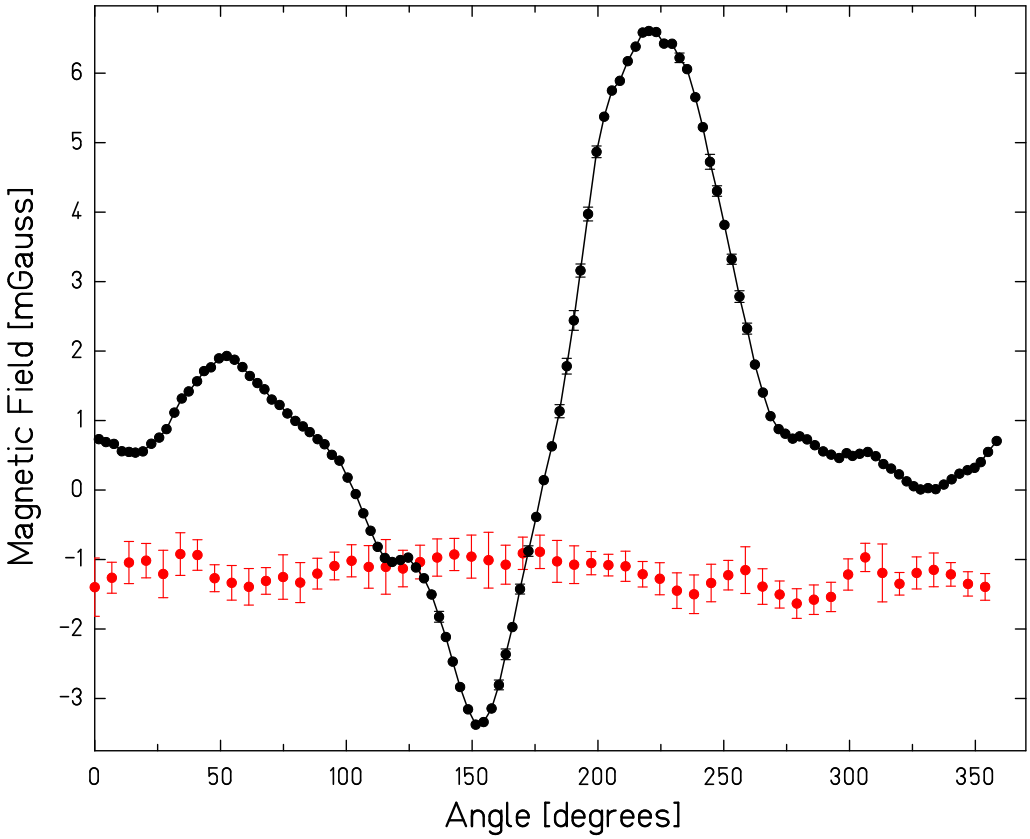

Figure 6.2: The azimuthal magnetic field just outside of the μ-metal can enclosing the pendulum spin-ring, measured while the spin-ring rotated beneath the magnetic field probe. The black circles show the measured magnetic field outside the solid can (`tst-wash run2679`) and the red circles show the measured magnetic field outside the nested cans (`tst-wash run3092`).

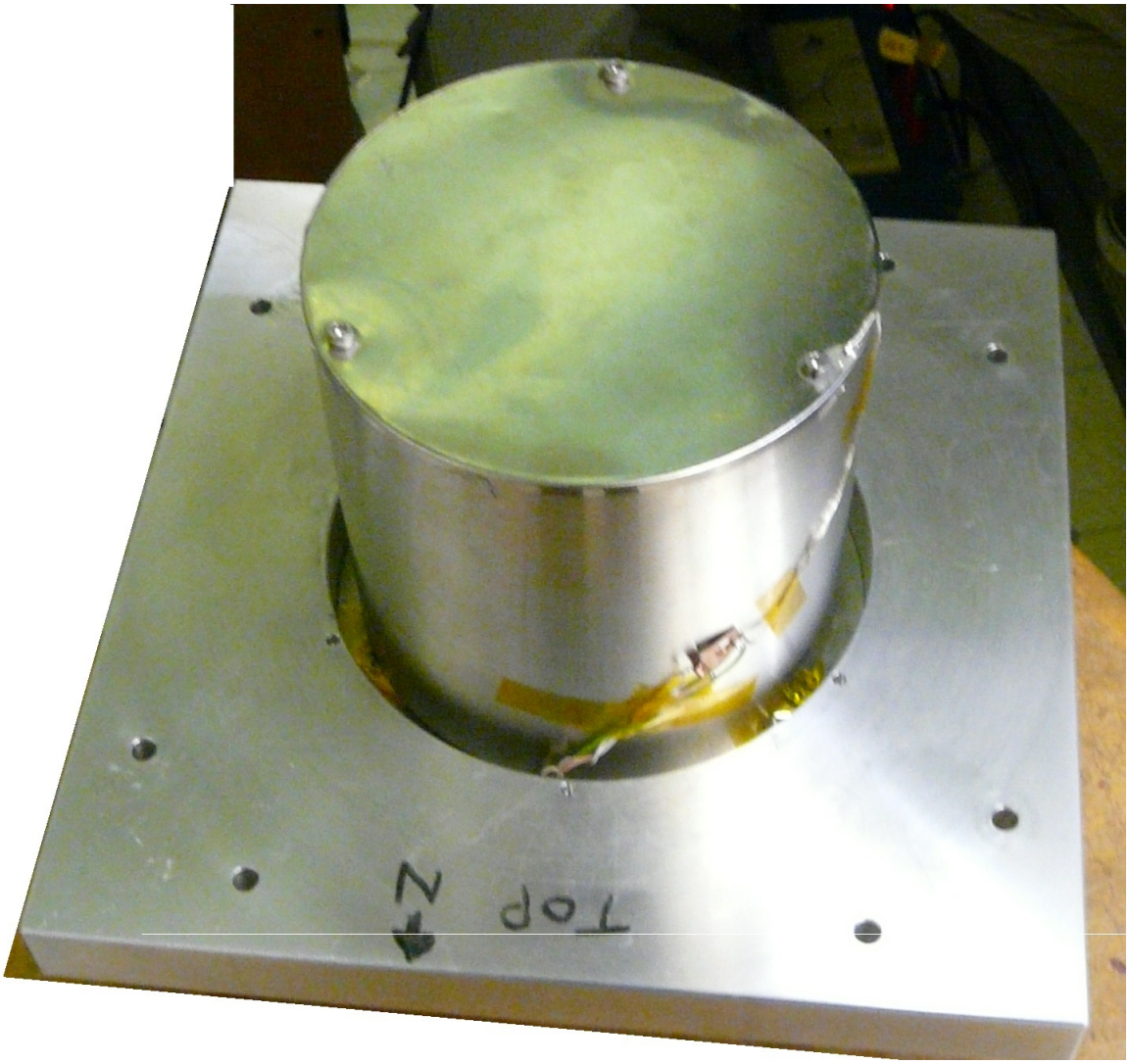

Figure 6.3: Photograph showing the μ-metal enclosure surrounding the attractor turntable.

6.1.2 Improvements in the Torque Sensitivity

The fluctuation-dissipation theorem says that the noise amplitude of a mechanical oscillator goes as $\sqrt{\kappa/(2\pi Q f)}$, as shown by Saulson[41], where κ is the restoring force of the oscillator, Q is the quality factor of the oscillator (κ/Q is the imaginary part of κ) and f is the frequency at which the noise is being measured. We have reduced the torque noise contributions of all three components of the torque noise.

6.1.2.1 Improved Pendulum Quality Factor

The motion of the pendulum above the conducting μ-metal screen produces eddy currents in the screen that can damp the pendulum. We attributed the small Q of the Mark I pendulum to this sort of eddy current damping. The nested μ-metal cans reduced the magnetic moment of the pendulum which, if the magnetic damping hypothesis holds, should improve the Q of our pendulum. With the new magnetic shields on the pendulum, the Q of our pendulum increased from $Q \sim 600$ to $Q \sim 1500$ based on the width of the torsional resonance peak. This reduction in magnetic damping should provide a factor of 1.6 improvement in torque noise.

6.1.2.2 Thinner Fiber

We switched from a 27 μm diameter torsion fiber to a 20 μm diameter torsion fiber. The torsion constant of a fiber, κ, scales with the radius of the fiber to the fourth power, r^4, so the change in the fiber should reduce κ by a factor of 3.3. The 27 μm diameter fiber had a measured κ of 0.116×10^{-3} fN-m/nrad, and the measured κ of the 20 μm fiber was $\kappa = I(2\pi/T)^2 = 134(2\pi/407.1)^2 \mathrm{g\,cm^2/s^2} = 0.031 \times 10^{-3}$ fN-m/nrad, where I represents the calculated moment of inertia of the pendulum with the new shields and T represents the measured free torsion period of the pendulum. The smaller κ of the fiber should reduce the torque noise of our instrument by a factor of 2.

6.1.2.3 Faster Turntable Rotation

In the Mark I apparatus, the maximum attractor turntable rotation rate we could reliably hold in feed-back was about 4000 s/rev, due to friction in the sliding contact that provided electrical connection to the attractor turntable. An improved electrical contact, designed by Andreas Kraft, allowed turntable rotation rates up to 1000 s/rev. Autocollimator noise becomes increasingly important at frequencies above the free torsion frequency of the pendulum, so in practice our best over-all noise comes at a signal frequency of roughly 4.5mHz or a turntable rotation rate of 2200 s/rev. Taking data at the higher frequency improved our torque noise by a factor of 1.4 relative to our previous operating frequency. Figurefig: atten 2 shows the attenuation corrections from the torsion filter at the faster turntable speeds. Section 4.2.2 contains further discussion of the torsion filter.

6.1.2.4 Measured Reduction in Torque Noise

Power spectra, in Figure 6.5, show a factor of $\sim$ 20 improvement in the noise power at the signal frequency as compared to our previous data. This corresponds to a reduction of ~ 4.5 in the amplitude of the torque noise, very close to the cumulative improvement we expected from all of our upgrades: $1.6 \times 2 \times 1.4 = 4.5$.

6.1.3 Improved Gravitational Compensation System

In the Mark II experiment we compensated the gravitational moments of both the pendulum and the attractor. Given the existing spin-rings and commercially available shim-stock, the optimal compensation consisted of 0.076 mm thick trapezoidal shims placed above and below each magnet segment, with tungsten (19.3 g/cc) shims on the Alnico magnets and titanium (4.54 g/cc) shims on the $SmCo_5$ magnets.

We placed the compensators on the magnets segments by hand, aligning them under the magnifying camera of the Smartscope and fixing them in place with epoxy. The alignment error of placing each shim was $\sim 25\mu$m or $\sim 0.15^\circ$. The effect of such a misalignment on the quality of the compensation is negligible. Fig. 6.6 shows calculations of the expected gravitational torques on the pendulum due the spin attractor with this compensation system

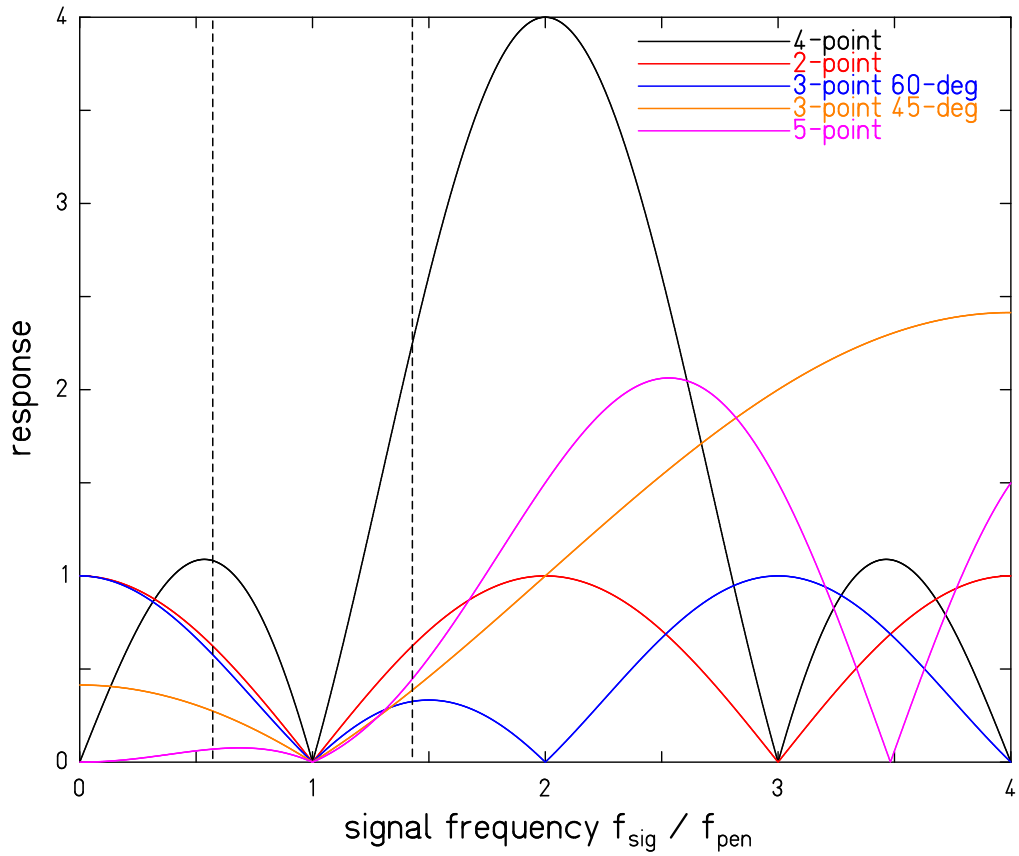

Figure 6.4: Effect of various torsion filters on the 4ω and 10ω signal harmonics.

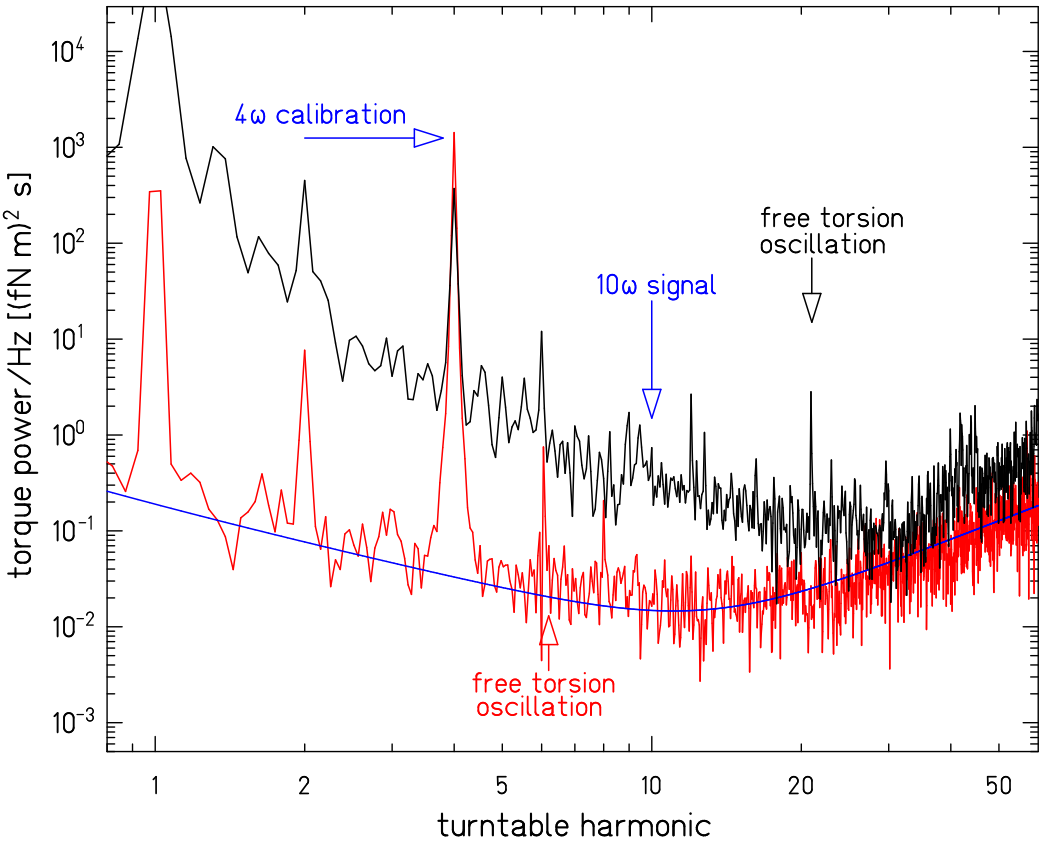

Figure 6.5: Power spectral densities of the torque on the pendulum before (black curve `run4421`) and after (red curve `run4897`) the upgrades to the instrument. The data taken after the upgrades shows a factor of 20 reduction in the torque noise power at the signal frequency compared to the earlier data. The rising noise at high frequencies is the angle readout noise folded into the inertial response of the pendulum above resonance. The weaker torsion fiber lowered the torsional frequency and with it the frequency at which angle readout noise becomes important.

in place.

Compensating the pendulum also reduced the gravitational 10ω torque due to the mass attractor, directly reducing the leading systematic in our monopole-dipole experiments.

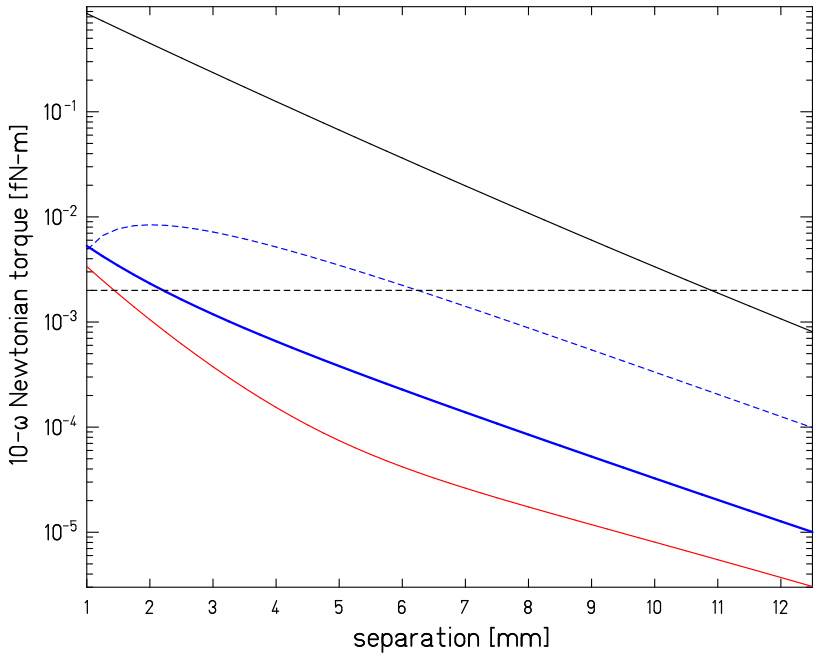

Figure 6.6: Calculations of the gravitational torque applied to the pendulum by the spin attractor. The horizontal dashed line shows the target torque sensitivity of our second data run, with data taken between 3 mm and 5 mm. The heavy blue line shows the calculated gravitational torques on the compensated pendulum using the measured masses for all the magnets and shims. The red line shows what the torque would have been if all the components had their expected densities and dimenions. The black line shows the predicted gravitational torque with out any compensation, and the dashed blue line shows the gravitational torque using the first, attractor only, compensation system.

6.1.4 Reduction in Pendulum-Attractor Minimum Separation

The energy of the dipole-dipole interaction drops off as $1/r^3$, so reducing the distance between the spin elements of the attractor and pendulum greatly increases our sensitivity to new physics. We made several changes to the apparatus to reduce the minimum possible separation, $Z_{\min}$, between the spin elements of the pendulum and the attractor.

6.1.4.1 Eliminating the Compensator Alignment Disks

Gluing the compensation wedges directly on the magnets eliminated the need for the alignment disks and reduced $\mathrm{Z_{min}}$ of the spin sources by 1.12 mm.

6.1.4.2 Thinner Magnetic Shields

Each set of nested cans had a total thickness of 0.53 mm between the pendulum and the attractor, down from 0.76 mm of material for each solid can, for a total reduction in $Z_{\min}$ of 0.46 mm.

The thickness of the μ-metal in the screen and the size of the gaps between them had no noticeable effect on the magnetic shielding of the screen, so we made the multi-layer screen from thinner magnetic sheets with less space between them. The screen contained from 10 layers of 0.05 mm thick μ-metal foils laminated together using Ecobond-22 adhesive and separated by 0.025 mm thick aluminum foils, with a top layer that was 0.25 mm thick so it could be swaged over to form a good fit with the new μ-metal cylinder surrounding the attractor turntable. The total screen thickness decreased by 1.04 mm from 2.03 mm to .99 mm.

We reduced $Z_{\min}$ to 2.42 mm by eliminating passive space and using the improved nested μ-metal cans and multilayer screen, for a total reduction of 2.62 mm in the material separating the spin rings.

6.2 Alignments and Calibrations of the Mark II Instrument

We used the procedures detailed in Chapter 4 to align the instrument for data taking and to establish the distance between the pendulum and attractor for each attractor. Z separations

refer to the average Z distance between the surfaces, i.e. Z_{sep} is the distance between the center of the bottom surface of the pendulum magnets and the center of the top surface of the mass attractor or the magnets of the spin attractor.

6.2.1 Spin Pendulum

We leveled the pendulum above the split-capacitor, described in Section 4.1.3.1, and calibrated the residual tilt by placing a 0.20 g nut first on one side of the pendulum and then on the other `[runs 4803 - 4806]`.The bottom surface of the pendulum and the torsion axis of the pendulum were perpendicular to 6.5 mrad.

We centered the pendulum horizontally above the attractor rotation axis by finding the phi-top position that maximized the 4ω torque applied to the pendulum by the mass attractor. Fitting the torques measured at various x & y positions to parabolas showed that the pendulum and attractor axes coincided to 22 μm.

6.2.2 Mass Attractor

6.2.2.1 Alignment

We aligned the mass attractor by mounting it under the SmartScope and tuning the kinematic mounts to center and level the attractor to the bearing rotation axis. In the end the symmetry axis of the mass attractor and the rotation axis of the bearing were parallel to within 2 mrad and offset by 20 μm horizontally, as measured optically on the SmartScope. Additional SmartScope data, analyzed in `gattr_screen2_15.nb` shows the top surfaces of the mass attractor and the μ-metal screen were 0.77 mm apart and 1.4 mrad from parallel. A burr on the mass attractor limited our ability to bring the attractor and screen closer together.

6.2.2.2 Pendulum to Mass Attractor Distance

We determined the pendulum to mass attractor distance by fitting the capacitance scan `sp4dscrz.dat` to the electrostatic model of capacitance as a function of distance contained in `spfoil.ans`. Section 4.1.4 contains more detail about the procedure. The capacitance

scan had a kink at 70 pF, which we interpreted as being the point at which the edge of the pendulum touched the screen. At 70 pF the center of the pendulum would be 0.27 mm above the screen, so we used the pendulum tilt to fix the "bounce correction" in `FITCAP32` to 135 μm.

We determined the distance from the bottom of the μ-metal can on the pendulum to the top of the screen, Z_{screen}, for our closest runs, `run4775 & run4784`, by comparing the capacitances measured during those runs to the fit of our capacitance scan. The capacitance was a very weak function of distance for the farther away runs, so we established Z_{screen} for `run4778, run4780, run4782` by comparing their measured Z_{mic} values with the Z_{mic} measured in runs `4775` and `4784`. The total distance from the bottom of the pendulum magnets to the top of the attractor, denoted Z_{sep}, was Z_{screen} plus the 0.77 mm gap from the screen to the attractor plus 0.74 mm of magnetic shielding and compensation shims on the pendulum for a final $Z_{\text{sep}} = Z_{\text{screen}} + 1.51$ mm. Table 6.1 shows the measurements we used to determine the distance from the bottom of the μ-metal can on the pendulum to the bottom of the pendulum magnets.

6.2.3 Spin Attractor

6.2.3.1 Alignment

We aligned the spin attractor to the bearing rotation axis using SmartScope measurements of the alignment. After adjusting the kinematic mount holding the attractor, the symmetry axis of the spin attractor and the rotation axis of the bearing were within 5 mrad of parallel and offset by 8 μm horizontally, so the spin attractor was in essentially the same position relative to the bearing mount as the mass attractor. The top surface of the μ-metal screen was an average of 2.32 mm above the top surface of the spin attractor, with a deviation from parallel of 10 mrad. `Mathematica` notebook `sattr_screen4_15.nb` contains the SmartScope measurements spin attractor to screen alignment.

Table 6.1: Measurements relevant to establishing Z_{sep} and the positions of the magnets from Z_{pucks}, the distance between centers of the closest surfaces on the pendulum and attractor. We assume the magnets were vertically centered relative to their respective assemblies and shims, so half of the additional thickness measured was above and below each of the spin rings. Dimensions are in mm and uncertainties are all ± 0.03 mm.

Pendulum	
Thickness of magnets:	3.00
Thickness with shims:	3.25
Thickness of assembly:	4.47
Distance from bottom of magnets to bottom of shims:	0.13
Distance from bottom of magnets to bottom of assembly:	0.74
Spin Attractor	
Thickness of magnets:	4.17
Thickness of assembly:	5.33
Thickness with shims:	4.32
Distance from top of magnets to top of shims:	0.076
Distance from top of magnets to top of assembly:	0.58

6.2.3.2 Pendulum to Spin Attractor Distance

We determined the pendulum to spin attractor distance by fitting capacitance scans to electrostatic models of the capacitance computed in `COMSOL`. Section 4.1.4 contains more details about the fitting procedure. We estimated the robustness of our results by doing scans both to the screen and directly to the attractor and fitting the scans in several ways, for a total of 6 estimates of the position at which the pendulum would lie flat on the attractor. Appendix D contains specifics about the scans and fits. The average $Z_{\rm mic}$ at which the pendulum would lie flat on the attractor was -3.48 $\pm$ 0.01 mm, using the standard deviation of the 6 estimates as the uncertainty. We then found $Z_{\rm sep}$ from the $Z_{\rm mic}$ of the data and the difference between the thicknesses of the spin rings and the thicknesses of the assemblies.

6.3 Results from the Mark II mass attractor Data Set

6.3.1 Measured Torques

We took data with the pendulum at five different heights above the mass attractor, with $Z_{\rm sep}$ between 2 and 8 mm, with the attractor rotating at 2849 s so that each attractor revolution contained 7 free torsion oscillations of the pendulum. Table 6.2 has details about the run parameters of this data set. Our χ^2 tests eliminated no data from this data set. The power spectrum of our closest data with the mass attractor, Fig. 6.7, shows that the statistical uncertainty of these measurements was due to the thermal noise of the fiber. The 4ω, 8ω, 10ω and free torsional peaks stand out clearly above the noise with the 10ω peak reduced by 200 times in torque power compared to the Mark I data. Table 6.3 lists some relevant torque amplitudes extracted from our data.

6.3.2 Separating Monopole-Dipole and Gravitational Signals

We used the formulas worked out in Section 5.1.2 to determine the monopole-dipole and gravitational components of the observed 10ω torque. Removing the 4 tungsten rods from the mass attractor rotated the extrema of the gravitational energy by 45°, and with it the 4ω signal by $45^\circ \mod 36 = 9^\circ$ relative to the 10ω signal. The expected phases of the gravitational signal, ϕ_g, and monopole-dipole signal, ϕ_s, become

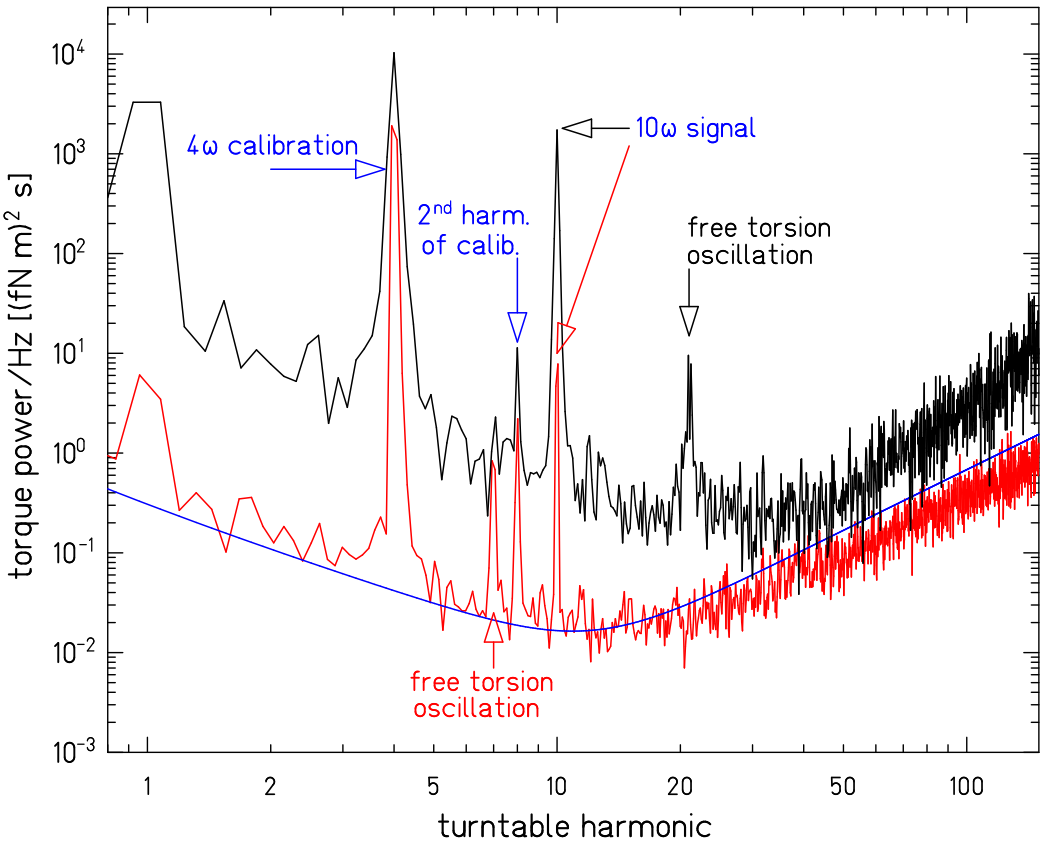

Figure 6.7: Power spectral densities of the torque on the pendulum at similar Z_{sep} above the mass attractor, taken before (black curve [run4387]) and after (red curve [run4775]) the upgrades to the instrument. Compared to the earlier data, the data taken after the upgrades has 20 times less torque noise power at the 4ω and 10ω signal frequencies. The power in the 10ω peak decreased by two orders of magnitude because we gravitationally compensated the pendulum. The rising noise at high frequencies is the angle-readout noise folded into the inertial response of the pendulum above resonance. The weaker torsion fiber lowered the torsional frequency and with it the frequency at which angle readout noise becomes important.

Table 6.2: Parameters of the runs making up the Mark II mass-attractor data set. Cap and Z_{mic} are the measured pendulum-screen capacitance and Z-micrometer value respectively for each run. Z_{screen} is the distance between the top of the μ-metal screen and the bottom of the pendulum assembly. Z_{pucks}, Z_{shims}, and Z_{sep} are the distances from the top of the mass attractor to the bottom of the pendulum, as defined by the μ-metal cans, compensation shims and magnets, respectively. All distances are in mm. The final column gives the calculated torque that a new monopole-dipole potential with coupling constants $g_p g_s/\hbar c = 1$ would produce at that separation.

Run	Cuts	Cap	Z_{mic}	Z_{screen}	Z_{pucks}	Z_{shims}	Z_{sep}	Sensitivity
4775	48	40	-2.14	0.85	1.24	1.85	1.98	3.1E+26
4784	29	37	-2.09	0.93	1.29	1.90	2.03	2.9E+26
4782	26	18	-1.112	1.89	2.268	2.88	3.00	1.6E+26
4780	33	13	-0.08	2.91	3.3	3.91	4.04	8.2E+25
4778	25	9	3.87	6.8	7.25	7.86	7.99	7.5E+24

$$\phi_g = (\phi_4 + \pi/4) \mod \pi/10 \tag{6.1}$$

$$\phi_s = \phi_g + \pi/(2 \cdot 10) \tag{6.2}$$

Our measured $\phi_{10\omega}$ was very close to ϕ_g, so we used the approximate expressions given in Equations 5.9 and 5.10 for the amplitudes of the monopole-dipole and gravitational signals, respectively, and Equations 5.16 and 5.17 for their respective uncertainties. Table 6.4 summarizes the results of this analysis.

6.3.3 Comparison of Measured and Calculated Gravitational Torques

6.3.3.1 4ω Gravitational Torques as a Function of Separation

We compared the measured and calculated 4ω torques using `FITTOR32`. Figure 6.8 shows the data and calculation, using independently determined normalizatons and separations.

Table 6.3: Measured torques at five different separations between the pendulum and mass attractor from our 2^{nd} data set. Amplitudes A are in fN-m and phases ϕ are in degrees. Uncertainties in the final digit follow in parentheses

Run	$A_{4\omega}$	$\phi_{4\omega}$	$A_{10\omega}$	$\phi_{10\omega}$	$A_{8\omega}$	$\phi_{8\omega}$	$A_{1\omega}$	$A_{\mathrm{high}-\omega}$
4775	5.611 (8)	37.03 (2)	0.344 (4)	27.56 (8)	0.157 (4)	14.6 (2)	0.28 (2)	0.004 (2)
4784	5.471 (9)	37.04 (2)	0.327 (5)	27.62 (7)	0.151 (6)	14.5 (3)	0.24 (3)	0.009 (2)
4782	3.036 (6)	37.08 (3)	0.158 (4)	27.3 (1)	0.054 (5)	15.4 (7)	0.31 (5)	0.006 (2)
4780	1.69 (15)	36.9 (1)	0.081 (7)	27.6 (8)	0.013 (9)	21 (7)	0.32 (8)	0.01 (3)
4778	0.19 (14)	36.2 (9)	0.007 (7)	22 (6)	0.005 (9)	1 (12)	0.26 (9)	0.01 (3)

Table 6.4: Separation of the 10ω signal into gravitational and monopole-dipole components. Z_{sep} is in mm, all amplitudes are in fN-m and angles are in degrees. Table 6.5 lists the contributions to the uncertainty in $|A_{\mathrm{s}}|$ at the 1.98 mm separation.

Run	Z_{sep}	$A_{10\omega}$	$\phi_{10\omega}$	ϕ_{g}	—A_{g}—	$\lvert A_{\mathrm{s}}\rvert$
4775	1.98	0.344 ± 0.004	9.56 ± 0.08	10.03 ± 0.02	0.326 ± 0.004	0.018 ± 0.013
4784	2.03	0.327 ± 0.005	9.62 ± 0.07	10.04 ± 0.02	0.312 ± 0.005	0.015 ± 0.013
4782	3.00	0.158 ± 0.004	9.34 ± 0.14	10.08 ±0.03	0.145 ± 0.004	0.013 ± 0.006
4780	4.04	0.081 ± 0.007	9.6 ± 0.8	9.9 ± 0.1	0.078 ± 0.007	0.003 ± 0.008
4778	7.99	0.007 ± 0.007	3.8 ± 6.1	9.2±0.9	0.003 ± 0.007	0.004 ± 0.006

Table 6.5: Error budget for the Mark II monopole-dipole constraints

Statistical uncertainty from error in measured 10ω phase:	0.003 fN-m
Statistical uncertainty from error in measured 4ω phase:	0.0008 fN-m
Systematic uncertainty from orientation of shims and magnets:	0.012 fN-m
Combined uncertainty:	0.013 fN-m

We calculated the torques with `FBESSELN` and our model (`c2rods.fbi`) was the same as for the Mark I experiment but without the tungsten rods in the attractor.

6.3.3.2 10ω Gravitational Torques as a Function of Separation

The 10ω gravitational torques applied to the pendulum by the mass attractor directly measured the gravitational field of our pendulum. The net gravitational 20-pole of the pendulum was the residual from the cancelation between the 20-pole of the spin-rings and the 20-pole of the compensator shims and was therefore very sensitive to imperfections in the cancelation. Measuring the thickness of the pendulum spin ring with the compensation shims in place indicates that there was 60 μm of glue between the magnets and the shims. We fitted our torque calculations of the compensated pendulum with the 60μm gap to the measured 10ω gravitational torque using `FITTOR32`, with the results shown in Figure 6.9. Scaling the calculated 10ω torques by 1.34 ± 0.01 gives a reasonable fit to the data with a χ^2 of 7.6 for 4 degrees of freedom. We attribute the difference between the predicted and measured torques to additional misalignments of the compensator shims.

6.3.4 Constraints on Monopole-Dipole Interactions

Our constraints on new monopole-dipole interactions come entirely from the data taken with the smallest pendulum to attractor separation. From the our measurements (Table 6.4) we set an upper limit at 68% confidence that a new monopole-dipole interactions produce torques on the pendulum of less than 0.023 fN-m.

We calculated the torque that a new monopole-dipole interaction would produce on the pendulum using the Fourier-Bessel expansion of the model contained `c2bare.fbi` and $Z_{\rm sep}$ = 1.98 mm We repeated the calculation for a number of Yukawa lengths, and ruled out any monopole-dipole interactions that would produce a torque greater than 0.023 fN-m at that separation. Figure 6.10 shows the constraints derived from this work, which improves the limits on a new monopole-dipole interaction coupled to electron spins for all boson masses between ~ 1.5 and $400\,\mu$eV.

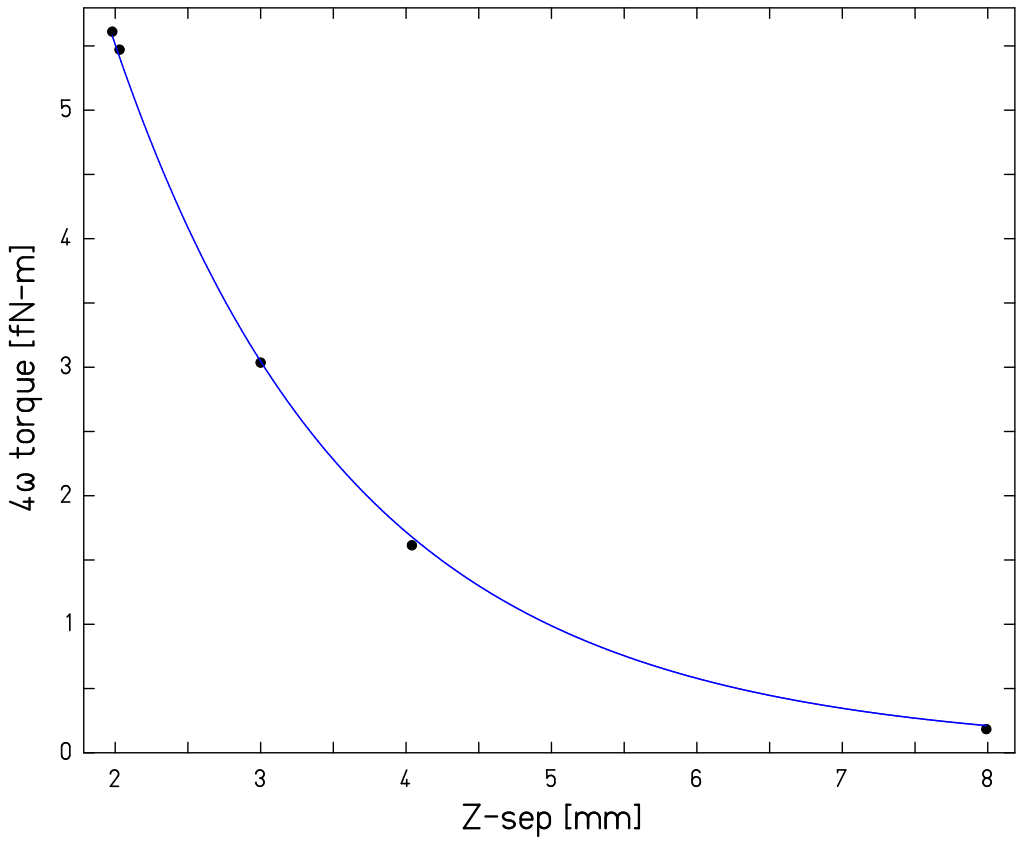

Figure 6.8: Comparison of measured and calculated 4ω torques on the pendulum applied by the mass attractor. The line show the calculated torques with no free parameters: the normalization comes from moment of inertia of the pendulum and its period, and the Z-scale comes from the SmartScope measurements and capacitance scans discussed in Section 6.2.2

.

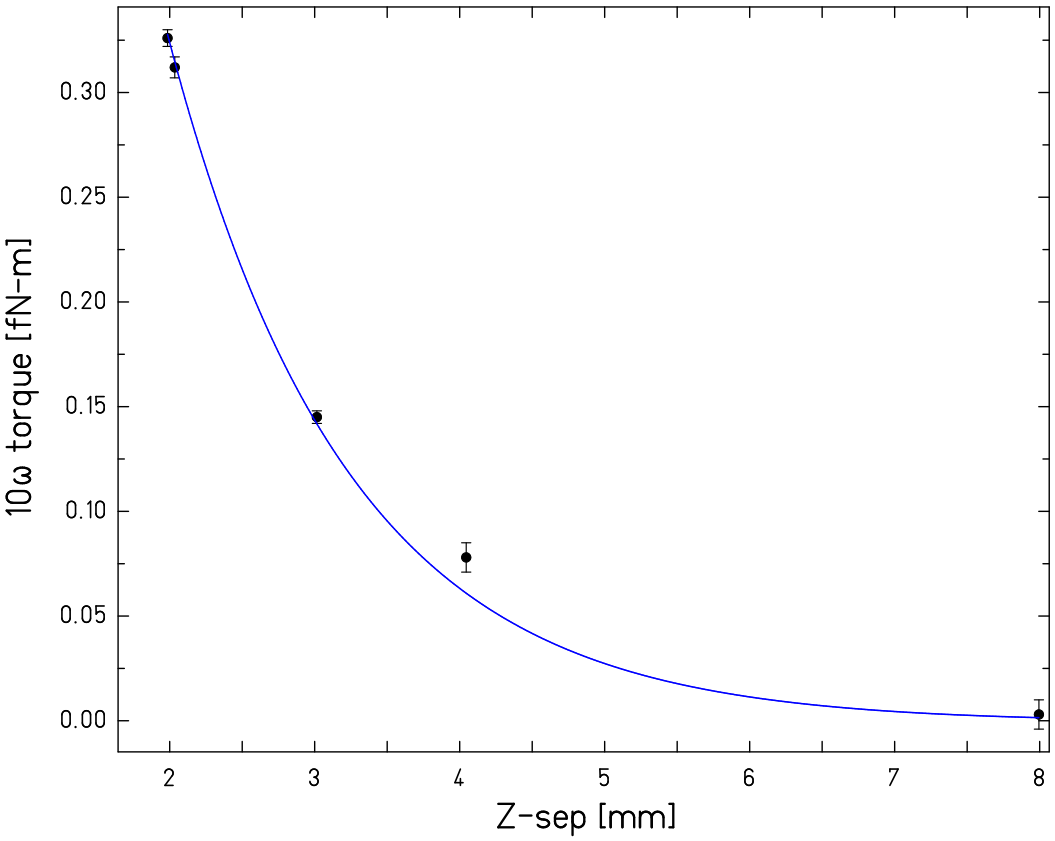

Figure 6.9: Comparison of measured and calculated 10ω gravitatonal torques applied to the pendulum by the mass attractor. The line shows the calculated torques multiplied by 1.335 to produce the best fit to the measured torques with the Z-scale fixed by the SmartScope and capacitance scan measurements discussed in Section 6.2.2

.

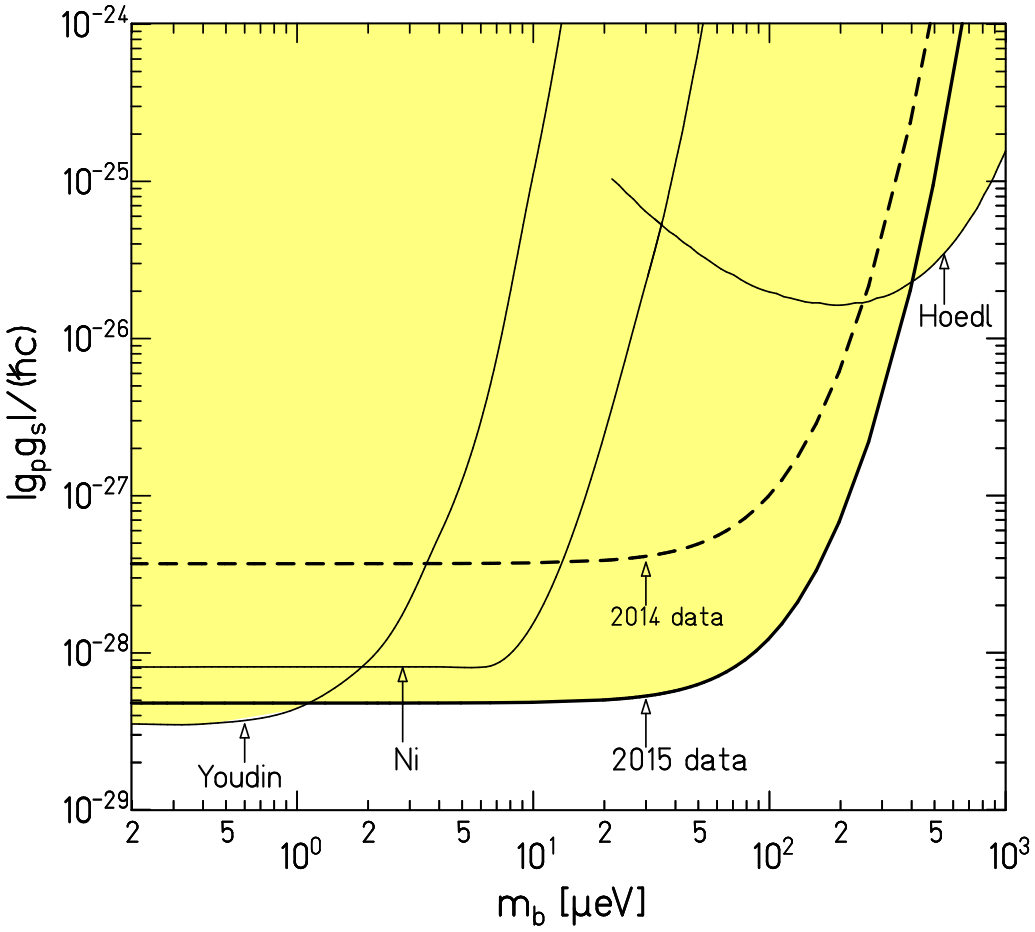

Figure 6.10: Constraints on short-range monopole-dipole interactions showing those derived from the data in this thesis along with previously published constraints. At very long ranges (low masses) limits from Heckel et. al. [38] are the most stringent, reaching 1.2×10^{-36} for infinite range interactions towards the sun.

6.4 Results from the Mark II Spin Attractor Data Set

6.4.1 Measured Torques

We took data with the pendulum at three different distances above the spin attractor, with $Z_{\rm sep}$ between 4.1 mm and 8.2 mm. At our closest separation we took significant amounts of data at two different attractor rotation periods, 2442 s and 2849 s corresponding to 6 and 7 times the pendulum free torsion period, respectively and reached an ultimate sensitivity of 1.8 a-Nm. The power spectrum 6.5 shows we reached the thermal noise limit of a 20 μm tungsten fiber with a Q of 1500. Table 6.6 summarizes the measured torques. Our χ^2 cut did not reject any data. We dropped two runs (`run4890 and run4892`) due to poor quality calibrations.

Table 6.6: Details of the runs making up the spin-attractor data set. The speed column refers to the number of free torsional periods of the pendulum per attractor revolution. Cap and $Z_{\rm mic}$ are the measured pendulum to screen capacitance in pF and Z-micrometer value respectively for each run. $Z_{\rm pucks}$, $Z_{\rm shims}$, and $Z_{\rm sep}$ are the distances from the top of the spin attractor and the bottom of the pendulum as measured between the μ-metal cans, compensation shims and magnets, respectively. All distances are in mm. The final column gives the expected torque in fN-m on the pendulum at that position, assuming an infinite range dipole-dipole interaction with dimensionless coupling constant $g_{\rm p}^2/\hbar c = 1$.

Run list	Runs	Speed	Cuts	Cap	$Z_{\rm mic}$	$Z_{\rm shims}$	$Z_{\rm sep}$	Sensitivity
zd7n6	4882c,97c	n=6	118	41.1	-0.68	3.93	4.12	$9.23 \cdot 10^{13}$
zd7n7	4879c,81c,86c	n=7	104	41.1	-0.68	3.93	4.12	$9.23 \cdot 10^{13}$
zd7com	zd7n6,n7	n=6&7	222	41.1	-0.68	3.93	4.12	$9.23 \cdot 10^{13}$
run4901	4901j	n=6	33	17.9	0.33	4.94	5.13	$4.84 \cdot 10^{13}$
run4907	4907c	n=6	44	10.4	3.35	7.96	8.15	$7.47 \cdot 10^{12}$

Table 6.7: Measured torques at three different separations between the pendulum and spin attractor from our Mark II data set. All amplitudes and their errors are in fN-m. All phases and their errors are in degrees. Top: Signal torques. Bottom: Diagnostic torques. $A_{\text{high}-\omega}$ is the average amplitude of all the harmonics from 5ω to 14ω excluding the the free torsion frequency and 8ω, the first harmonic of the gravitational calibration. A_{rand} is what we would expect for $A_{\text{high}-\omega}$ if the high harmonics were scattered around zero with a variance given by their weighted uncertainty.

Run list	$A_{4\omega}$	$\phi_{4\omega}$	$A_{10\omega} \times 10^3$	$\phi_{10\omega}$
zd7n6	2.863 ± 4	55.77 ± 0.02	2.9 ± 2.8	11.8 ± 5.5
zd7n7	2.855 ± 5	55.81 ± 0.03	0.7 ± 2.9	23 ± 24
zd7com	2.860 ± 3	55.79 ± 0.02	1.3 ± 2.0	13.7 ± 8.6
run4901	1.583 ± 8	55.87 ± 0.07	4.2 ± 5.9	0.4 ± 5.6
run4907	0.334 ± 6	55.94 ± 0.26	5.6 ± 3.4	23.3 ± 3.3

Run list	$A_{1\omega}$	$\phi_{1\omega}$	$A_{\text{high}-\omega} \times 10^3$	$A_{\text{rand}} \times 10^3$
zd7n6	1.77 ± 0.02	273.1 ± 0.5	5.2 ± 1.2	3.6
zd7n7	1.73 ± 0.02	270.4 ± 1.3	4.5 ± 1.2	3.6
zd7com	1.74 ± 0.02	272.8 ± 0.5	3.8 ± 0.8	2.7
run4901	0.69 ± 0.04	284.3 ± 3.0	7.9 ± 2.0	6.2
run4907	0.29 ± 0.04	288.5 ± 4.5	5.9 ± 1.5	4.6

6.4.2 Gravitational Background

We calculated the 10ω gravitational torque on the pendulum using the measured 60μm gap between the magnets and shims on the pendulum and no gap on the attractor and found it to be 0.6 aN-m at a $Z_{\rm sep}$ of 4.12 mm. From the measurements in Section 6.3.3.2, the gravitational field of the pendulum was 30% larger than calculated with our model. We assume the same compensation error on the spin attractor and scale our calculated gravitational 10ω torques by $(1.32)^2$ to estimate the gravitational background at 4.12 mm to be 1.05 aN-m.

6.4.3 Magnetic and Broadband Backgrounds

We characterize magnetic and other attractor-correlated backgrounds at our signal frequency using the measured torques of nearby harmonics from 6ω to 14ω that should not experience any gravitational or spin-related torques. We omit 8ω as the first harmonic of our calibration signal, as well as the harmonic corresponding to the free torsion period of the pendulum.

The average of the measured high-ω amplitudes was 3.8 ± 0.8 aN-m, consistent with the expected value of 2.7 ± 0.8 aN-m assuming no background and scatter described by the 2.1 aN-m weighted variance of the high harmonics.

Based on this, the error bars describe the distribution of our data well and we do not add any additional systematic uncertainty to our measurement from "broad-band" sources like magnetic cross-talk.

6.4.4 Constraints on Dipole-Dipole Interactions

The dipole-dipole interaction drops off rapidly with distance, as shown in the final column of Table 6.6, so our constraints on a new dipole-dipole interaction come entirely from our closest data. Table 6.8 summarizes the uncertainties in the data set we took at 4.12 mm.

We calculated the torque that a new dipole-dipole interaction would produce on the pendulum using the Fourier-Bessel expansion of the model contained `s2mag.fbi` and $Z_{\rm sep}$ = 4.12 mm We repeated the calculation for a number of Yukawa lengths, and ruled out

any dipole-dipole interactions that would produce a torque greater than 2.6 aN-m at that separation. Figure 6.11 shows the constraints derived from this work, which improves the limits on a new dipole-dipole interaction for all interaction ranges, down to $g_p^2 = 2.8 \times 10^{-17}$ at 1σ.

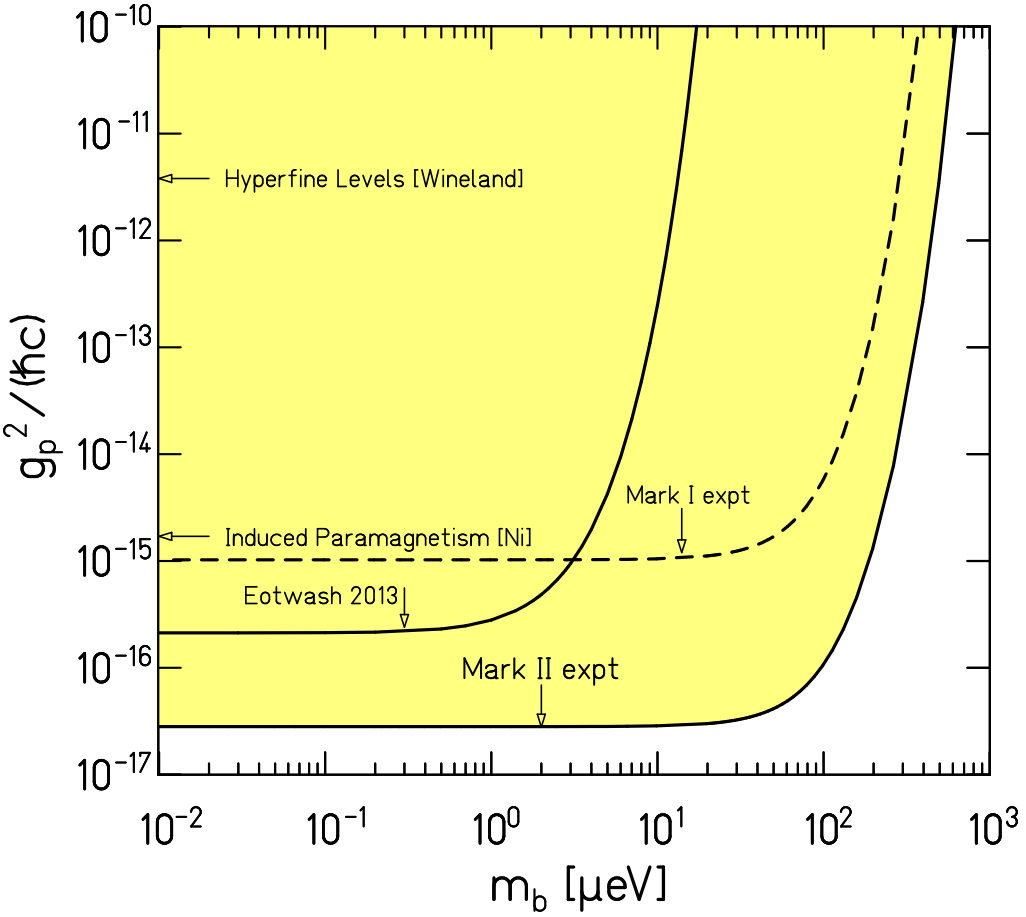

Figure 6.11: Constraints on new electron dipole-dipole interactions from the experiments described in this thesis, along with the best previous constraints that we are aware of. All of the constraints are given at the 1-σ level

6.4.5 Constraints on Hidden High-Energy Symmetries

These results also contrain hidden high energy symmetruies. We can interpret the limits on a new dipole-dipole interaction as excluding new pseudo-Goldstone bosons according to the equation $g_{\rm p} = \frac{m_\psi}{F}$ where in our set up m_ψ is the electron mass and F is the scale at which the hidden symmetry is broken. This allows us to rule out hidden symmetries with symmetry breaking scales up to 100 TeV, the highest symmetry breaking scales ever probed in the laboratory.

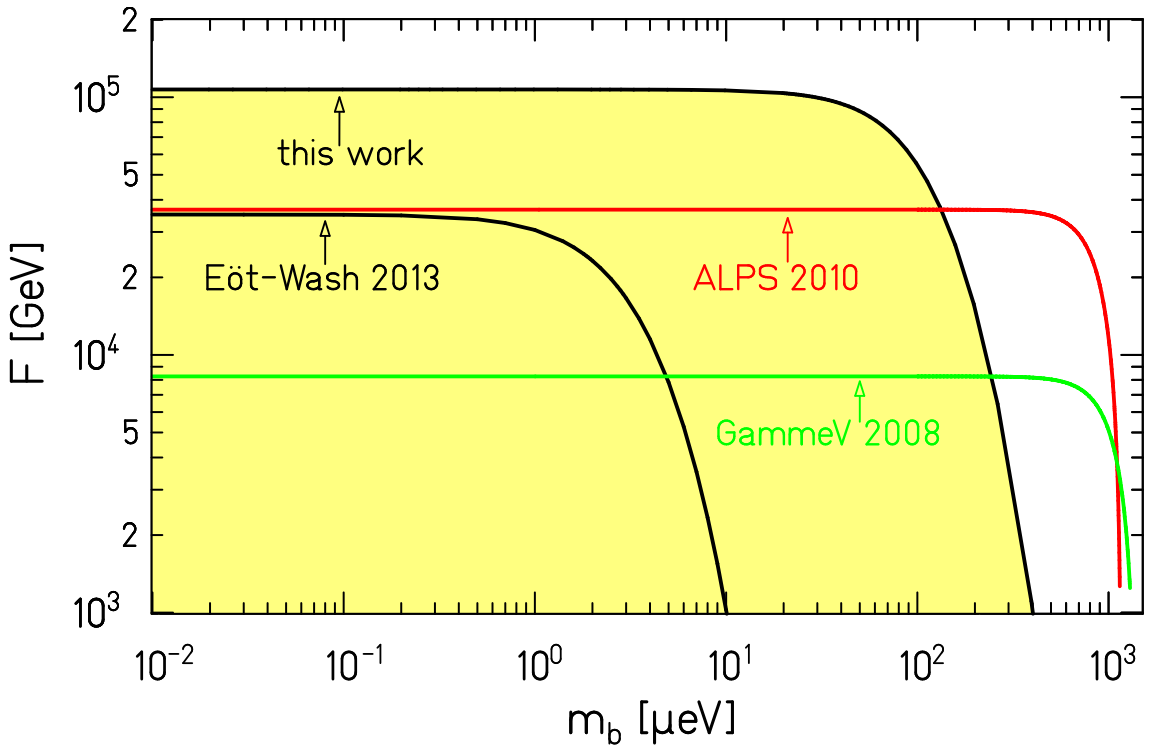

Figure 6.12: 1σ constraints on high-energy hidden symmetries that are spontaneously broken at an energy scale F. ALPS and GammeV are "light shining through walls" experiments looking for a new pseudoscalar through its coupling to electromagnetic fields.

Table 6.8: Error budget for the Mark II dipole-dipole constraints

Statistical uncertainty:	0.002 fN-m
Gravitational systematic:	0.001 fN-m
"Broad-band" backgrounds:	well described by statistical errors
Combined uncertainty:	0.0022 fN-m
Measured monopole-dipole torque:	0.0013 fN-m
Upper limit at 68% confidence:	0.0026 fN-m
Upper limit at 95% confidence:	0.0051 fN-m

Appendix A

DETAILS OF OUR GRAVITATIONAL MODEL

A.1 Spin Rings

All of the gravitational calculations were performed using the fourier-bessel expansion as implemented in `fbesseln.for`. All of the `.fbi` files are contained on `Npl-wt\\C:\mpc\shortr`.

- `sbarek.fbi` has the uncompensated pendulum.

- `snomk.fbi` contains the "design" version with the first version of the compensation (0.076 cm of Ta sitting 0.025 cm above and below each Alnico magnet and 0.076 cm Al sitting 0.025 cm above and below each $SmCo_5$ magnet) with nominal dimensions and densities.

- `smeas.fbi` has densities and thicknesses adjusted to match the measured masses of the components:

  The average mass of the Alnico magnets was 1.4270 (1.0452) g for the attractor (pendulum), while the average mass of the $SmCo_5$ magnets was 1.6226 (1.1900) g. The magnet segments have cross-sectional areas of 0.478 cm^2 and thicknesses of 0.409 (0.300) cm so for the gravitational calculation we use densities of 7.32 (7.29) g/cm^3 for the Alnico and 8.32 (8.30) g/cm^3. For the gravitational shims we used a thickness of 0.79 mm so that the modeled shim mass matches the measured average mass.

- `smisa.fbi` has the compensators misaligned by 0.3° relative to the magnets.

- For the second compensation setup the equivalent `.fbi` files are

  - `s2nom.fbi`
  - `s2meas.fbi` and

– `s2misa.fbi`

Figure A.1: Effect on gravitational signal if the compensators are maximally misaligned. This is for the first version of the compensation with only the attractor compensated.

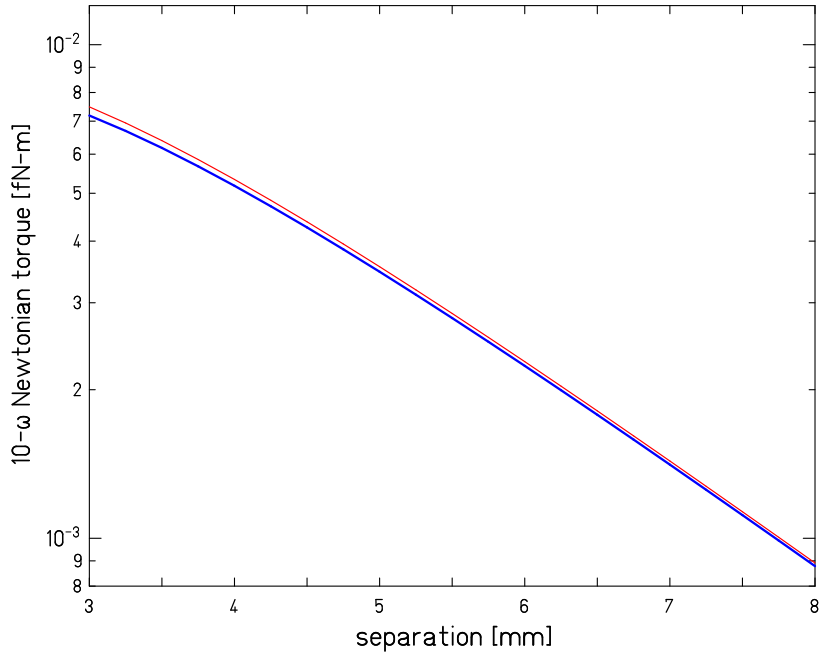

A.2 Tungsten Rods

We computed the torques from the tungsten calibration rods using the same Fourier-Bessel expansion. This required approximating the cylindrical rods as sectors of annuli. A range of inner and outer radii and angular widths (β) can all match the mass and center of mass of the rods (Figure A.2 inset). We used a direct numerical integration routine written by Charles Hagedorn to calculate the torque between sets of cylinders and determine the best geometry for the Fourier-Bessel approximation (Figure A.2). For this comparison we calculated the maximum torque exerted between two sets of 4 tungsten "slugs" at a series of vertical separations between 0.5 mm and 12.5 mm. One set contained "slugs" 0.3 cm tall

embedded into an aluminum disc on a 1.4 cm bolt-circle while the "slugs" in the other set were 4.5 cm tall and embedded on a 1.4 cm bolt-circle in a copper disc. The best match to the real 0.476 cm diameter cylinders were the 31.6° wide sectors. All of the various attractor configurations we used had 0.476 cm diameter rods on a 1.4 cm bolt circle, so we calculated all of the expected 4ω torques using this approximation.

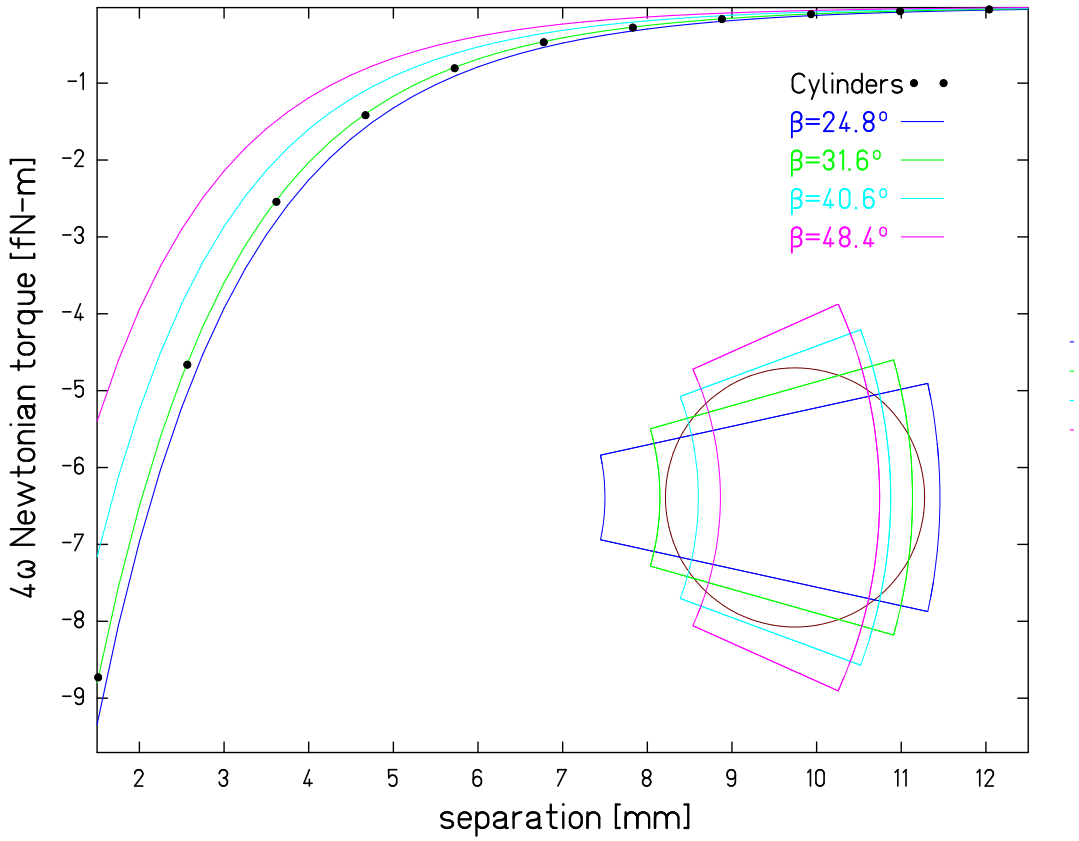

Figure A.2: Torque curves comparing various Fourier-Bessel approximations to a direct numerical integration. The inset shows the "slug" geometries corresponding to each curve. The wedge with an angular width of 31.6° (shown in green) was the best match.

Appendix B

CALCULATION OF THE PENDULUM'S MOMENT OF INERTIA

We calculated the moment of inertia of the pendulum with `TPL`. The `.tpc` files are stored in `NEWALBERT\\C:\tpl\spinspin`. The results were checked using `M2CAD`, with the `.scr` files on `gravity-daq\\C:\scr\spinspin`. Table B.1 in Appendix C lists the mass and moment of inertia for each component of the pendulum. The TPC file is rescales to match the measured mass listed here and improve the moment of inertia calculation. The total calculated moment of inertia for the Mark I pendulum was 114 g-cm^2; for the Mark II pendulum 134 g-cm^2

Table B.1: List of masses and moments of inertia for each component of the pendulum

Component	Mass [g]	Moment of Inertia [g-cm^2]	`.tpc` file
Lower Shield v. 1	9.315	25.9	`lshield.tpc`
Upper Shield v. 1	8.74	22.8	`ushield.tpc`
Lower Shield v. 2	9.84*	33.5	`lshields.tpc`
Upper Shield v. 2	10.1*	35.0	`ushields.tpc`
Central Alignment Post	1.9	0.9	`scenter.tpc`
Tungsten Calibration Rods	4.0	2.1	`tungsten.tpc`
Magnet Ring	22.3	55.5	`smagnets.tpc`
Mirror Post	2.8	1.2	`mirpost.tpc`
Lower Cube Attachment	0.2	0.04	`calow.tpc`
Mirror Cube	2.5	1.0	`cube.tpc`
Pin Thru Mirror	0.3	0.003	`pin.tpc`
Leveling Plate	2.45	1.9	`caup.tpc`
Leveling Screws	0.19	0.19	`levscrew.tpc`
Wave Washer	0.4	0.2	`washer.tpc`
Top Hat	4.1	2.2	`top.tpc`
Fiber Screw	0.5	0 .05	`fscrew.tpc`
Total No Shields	**41.7**	**65.3**	
Total v. 1 Shields	**59.8**	**114**	`pend.tpc`
Total v. 2 Shields	**61.7**	**133.8**	`pend2.tpc`

Appendix C

PROPERTIES OF MAGNETIC SEGMENTS OF THE SPIN-RINGS

C.1 Magnets used in the attractor

The 15 $SmCo_5$ attractor magnets we cut had an average mass of 1.6224 g, with a standard-deviation of 0.0015 g and a total spread of 0.0050 g. The 11 Alnico attractor magnets we cut had an average mass of 1.426 g, with a standard-deviation of 0.004 g and a total spread of 0.014 g. Details about the magnets we used in our instrument are given in Table C.1 and Figure C.1.

Table C.1: Attractor magnet properties. The values listed for the magnetic field are the peak-peak magnetic fields seen as each segmented rotated about its center. The Hall-probe was 1.27 cm away in the plane of rotation.

Alnico Number	Mass [g]	$SmCo_5$ Number	Mass [g]	B-Field [G]
Alnico 1	1.4327 g	$SmCo_5$ 1	1.6214 g	26.50
Alnico 2	1.4240 g	$SmCo_5$ 2	1.6215 g	26.56
Alnico 3	1.4245 g	$SmCo_5$ 4	1.6240 g	26.43
Alnico 4	1.4267 g	$SmCo_5$ 6	1.6239 g	26.43
Alnico 5	1.4245 g	$SmCo_5$ 7	1.6252 g	26.60
Alnico 6	1.4244 g	$SmCo_5$ 8	1.6210 g	26.47
Alnico 7	1.4258 g	$SmCo_5$ 9	1.6231 g	26.62
Alnico 8	1.4267 g	$SmCo_5$ 10	1.6220 g	26.48
Alnico 10	1.4294 g	$SmCo_5$ 11	1.6207 g	26.50
Alnico 11	1.4338 g	$SmCo_5$ 13	1.6233 g	26.42
Alnico Average	1.4270 g	$SmCo_5$ Average	1.6226 g	
Alnico Std. Dev.	0.0037 g	$SmCo_5$ Std. Dev.	0.0015 g	
Alnico Max-Min	0.0098 g	$SmCo_5$ Max-Min	0.0045 g	

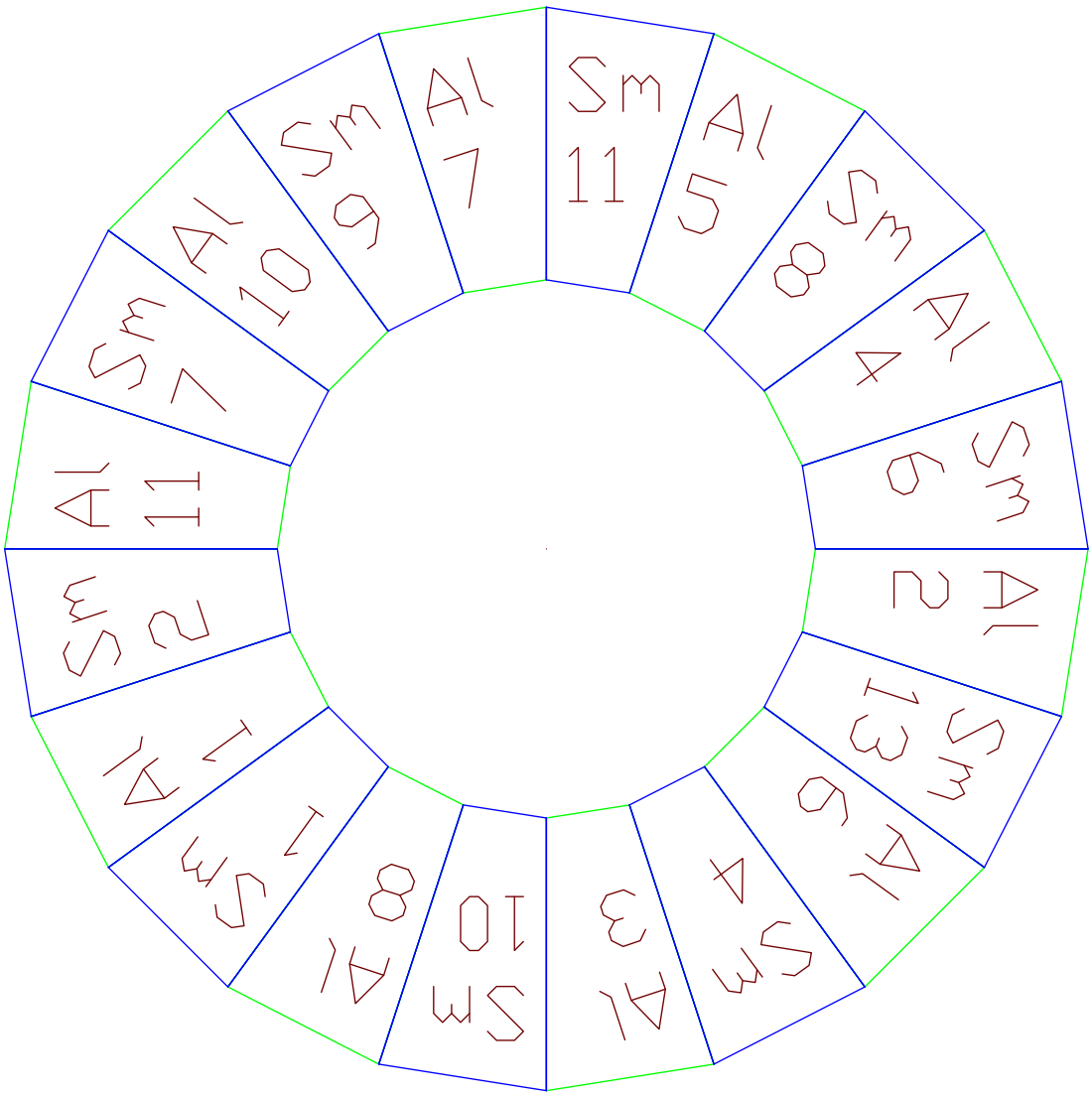

Figure C.1: The order of the magnets we used in the attractor ring, oriented with the magnetization running clockwise.

C.2 Magnets used in the pendulum

The 24 $SmCo_5$ pendulum magnets we cut had an average mass of 1.1901 g, with a standard-deviation of 0.0021 g and a total spread of 0.0066 g. The 16 Alnico pendulum magnets we cut had an average mass of 1.044 g, with a standard-deviation of 0.0019 g and a total spread of 0.0078 g. Details about the magnets we used in our instrument are given in Table C.2 and Figure C.2.

Table C.2: Pendulum magnet properties. The values listed for the magnetic field are the peak-peak magnetic fields seen as each segmented rotated about its center. The Hall-probe was 1.27 cm away in the plane of rotation.

Alnico Number	Mass [g]	$SmCo_5$ Number	Mass [g]	B-Field [G]
Alnico 3	1.0448 g	$SmCo_5$ 7	1.1906 g	19.06
Alnico 6	1.0442 g	$SmCo_5$ 9	1.1883 g	19.07
Alnico 7	1.0451 g	$SmCo_5$ 12	1.1928 g	19.09
Alnico 8	1.0442 g	$SmCo_5$ 14	1.18755 g	19.11
Alnico 9	1.0468 g	$SmCo_5$ 15	1.19096 g	19.13
Alnico 10	1.0440 g	$SmCo_5$ 16	1.1932 g	19.13
Alnico 11	1.0455 g	$SmCo_5$ 18	1.1906 g	19.07
Alnico 13	1.0455 g	$SmCo_5$ 19	1.1870 g	19.33
Alnico 14	1.0443 g	$SmCo_5$ 20	1.1885 g	19.08
Alnico 15	1.0474 g	$SmCo_5$ 23	1.1904 g	19.06
Alnico Average	1.0452 g	$SmCo_5$ Average	1.1901 g	
Alnico Std. Dev.	0.0011 g	$SmCo_5$ Std. Dev.	0.0022 g	
Alnico Max-Min	0.0034 g	$SmCo_5$ Max-Min	0.0063 g	

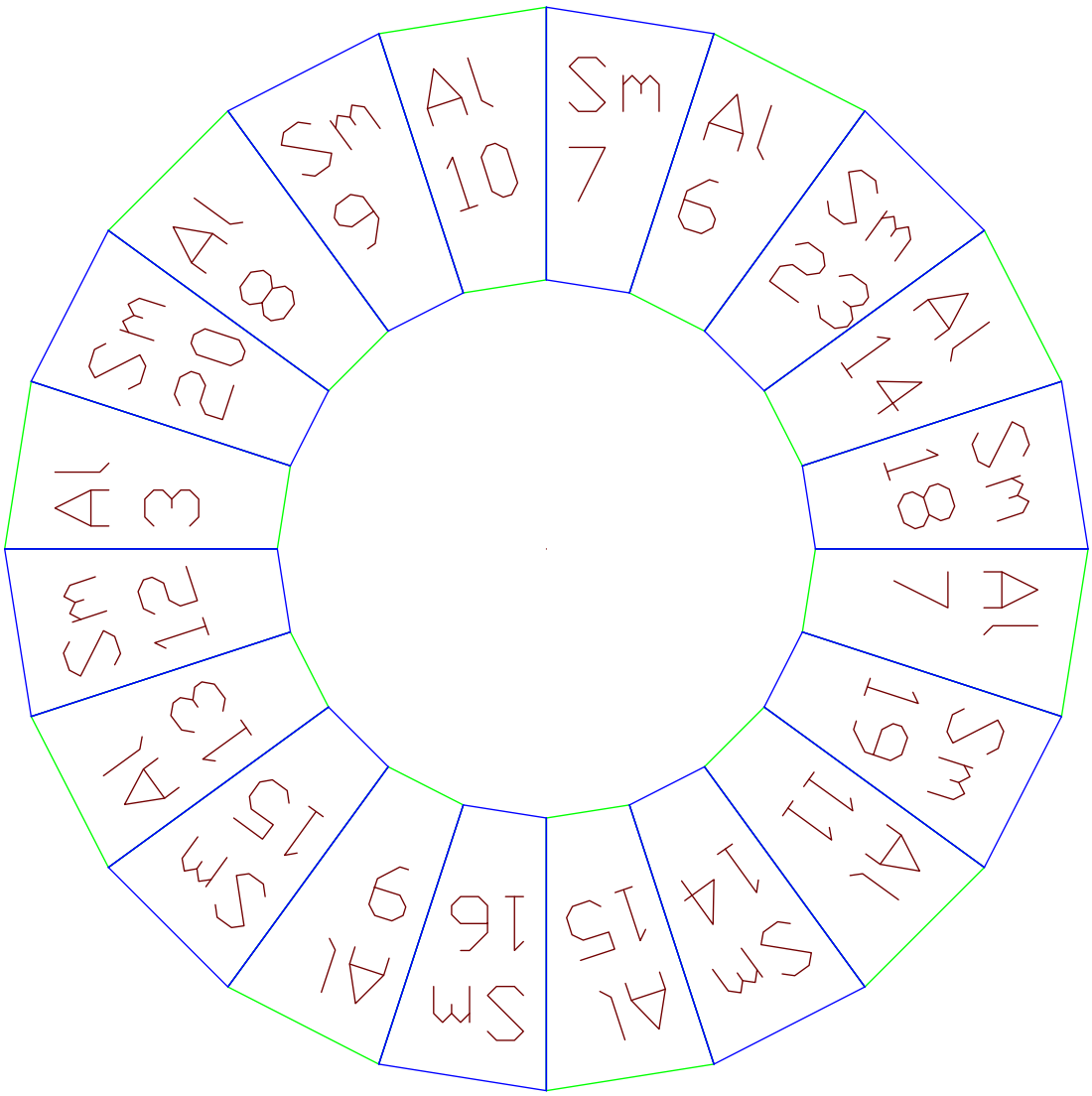

Figure C.2: The order of the magnets we used in the pendulum ring, oriented so the magnetization runs clockwise.

Table C.3: All of the weight measurements taken of the pendulum $SmCo_5$ magnets, in grams. In the columns labeled Low, the magnets were 3.91 cm above the balance. In the columns labeled High, the magnets were 7.62 cm above the balance. In Low 2 and High 2, the magnets we turned the magnets upside down relative to Low 1 and High 1. The average weight difference between flips (|L1-L2| or |H1-H2|) or in average weight at different heights are less than 100μg which is comparable to our instruments sensitivity of 50μg.

Magnet	Low 1	Low 2	High 1	High 2	Average	|L1-L2|	|H1-H2|	High-Low
PS1	1.1912	1.1912	1.19117	1.19117	1.19119	0.0E+00	0.0E+00	-3.0E-05
PS2	1.19272	1.19282	1.19272	1.19267	1.19273	1.0E-04	5.0E-05	-7.0E-05
PS3	1.1872	1.1874	1.1872	1.18732	1.18728	2.0E-04	1.2E-04	-4.0E-05
PS4	1.18882	1.1889	1.1886	1.18862	1.18874	8.0E-05	2.0E-05	-2.5E-04
PS5	1.18685	1.1868	1.1867	1.18682	1.18702	5.0E-05	7.8E-04	3.8E-04
PS6	1.1925	1.19242	1.19235	1.19247	1.19244	8.0E-05	1.2E-04	-5.0E-05
PS7	1.1913	1.1914	1.19142	1.19132	1.19136	1.0E-04	1.0E-04	2.0E-05
PS8	1.19022	1.1902	1.19015	1.19015	1.19018	2.0E-05	0.0E+00	-6.0E-05
PS9	1.1884	1.18835	1.18825	1.18825	1.18831	5.0E-05	0.0E+00	-1.2E-04
PS10	1.18785	1.18775	1.1877	1.18782	1.18778	1.0E-04	1.2E-04	-4.0E-05
PS11	1.1894	1.1893	1.1893	1.1893	1.18933	1.0E-04	0.0E+00	-5.0E-05
PS12	1.19277	1.19272	1.19277	1.19275	1.19275	5.0E-05	2.0E-05	2.0E-05
PS13	1.19357	1.1935	1.19345	1.19355	1.19352	7.0E-05	1.0E-04	-4.0E-05
PS14	1.1877	1.1876	1.1875	1.18742	1.18756	1.0E-04	8.0E-05	-1.9E-04
PS15	1.191	1.191	1.19092	1.19092	1.19096	0.0E+00	0.0E+00	-8.0E-05
PS16	1.1933	1.19322	1.19318	1.1932	1.19323	8.0E-05	2.0E-05	-7.0E-05
PS17	1.18902	1.1892	1.18897	1.189	1.18905	1.8E-04	3.0E-05	-1.2E-04
PS18	1.19062	1.19072	1.19055	1.1905	1.1906	1.0E-04	5.0E-05	-1.4E-04
PS19	1.187	1.1871	1.1868	1.18695	1.18696	1.0E-04	1.5E-04	-1.8E-04
PS20	1.18857	1.18857	1.18832	1.1884	1.18847	0.0E+00	8.0E-05	-2.1E-04
PS21	1.1893	1.18925	1.1892	1.18922	1.18924	5.0E-05	2.0E-05	-6.0E-05
PS22	1.1908	1.19072	1.19062	1.19065	1.1907	8.0E-05	3.0E-05	-1.3E-04
PS23	1.19047	1.19037	1.1904	1.1905	1.19044	1.0E-04	1.0E-04	3.0E-05
PS24	1.19305	1.1931	1.193	1.19297	1.19303	5.0E-05	3.0E-05	-9.0E-05
Ave	1.19015	1.19015	1.19009	1.19008	1.19012	**8.0E-05**	**8.0E-05**	**-7.0E-05**
StdDev	0.00212	0.00211	0.00211	0.00213	0.00212	**5.0E-05**	**1.6E-04**	**1.2E-04**

Appendix D

DETAILS OF CAPACITANCE SCANS

D.1 Variation in Z from Multiple Capacitance Scans

1. We took capacitance scans between the pendulum and the screen (`sp4lscrz.dat`) and between the pendulum and the spin attractor with the screen removed (`sp4nscrz.dat`). We fitted these scans to the electrostatic models `spfoil.ans` and `pendattr.ans`, respectively.

2. We varied the fit parameters to study they affected the outputs of the fit. The fits were most sensitive to the "bounce correction" so we used two different reasonable choices of "bounce correction" in fitting each of our capacitance scans:

   (a) Letting the "bounce correction" float to give the best possible fit to the electrostatic model.

   (b) Setting the "bounce correction" based on the tilt of the pendulum as explained in Section 4.1.4. We estimated tilt of the pendulum from the kink in the capacitance scan, interpreted as the corner of the pendulum first touching the screen. Figure 4.3 illustrates how we estimated the tilt.

3. There are two ways to determine the Z-position of the pendulum during data taking from the capacitance scan to the screen:

   (a) Based on the Z_{mic} value for the run. We compare this to the fit, which gives us the value of Z_{mic} where the pendulum would just lie flat on the screen.

   (b) Based on the pendulum to screen capacitance during the run. The fit to the capacitance scan tells us distance at which the capacitance between the pendulum and screen matches the capacitance measured during data taking.

Table D.1: Capacitance scans and fit parameters used in determining the pendulum to spin attractor separation. Distances are in mm. All of the fits used a Z-micrometer uncertainty of 1 μm and a capacitance uncertainty of 0.3 pF. Z_0 is the $Z_{\rm mic}$ at which the bottom of the pendulum μ-metal cans would lie flat on the relevant surface. The Z-offset from the top of the screen to the top of the attractor came from our SmartScope measurements. The $Z_{\rm mic}$ highlighted in bold indicate the numbers used to make the final estimate of the pendulum to spin attractor separation.

Scanned to:	Attractor		Screen	
Capacitance data file:	sp4nscrz.dat		sp4lscrz.dat	
Z-range included in fit:	-3.1 $\rightarrow$ 0.1 mm		-0.8 $\rightarrow$ 3.9 mm	
Electrostatic model:	pendattr.ans		spfoil.ans	
Choice of bounce correction:	float	from tilt	float	from tilt
Bounce term [μm]:	92$\pm$ 30	125	137 $\pm$ 21	110
χ^2/ν:	5.5	8.7	2.3	3.8
Stray capacitance:	-0.88 $\pm$ .47	-1.1 $\pm$ .4	1.08 $\pm$ .04	1.06 $\pm$ .02
Normalization:	1.03 $\pm$ .04	1.06 $\pm$ .06	1.08 $\pm$ .04	1.06 $\pm$ .02
Z_0 of surface, fitted [mm]:	-3.47	-3.48	-1.16	-1.14
Z offset to top of attractor:	—		-2.32	-2.32
$Z_{\rm mic}$ pendulum flat on attractor:	**-3.47**	**-3.48**	**-3.47**	**-3.46**
Average by surface scanned to:	-3.48 $\pm$ 0.01		-3.47 $\pm$ 0.01	
Distance above screen at 41.1 pF:	—		0.494	0.477
$Z_{\rm mic}$ during data taking:	—		-0.678	-0.678
$Z_{\rm mic}$ pendulum flat on attractor:	—		**-3.492**	**-3.475**
Average based on 41.1 pF distance:	—		-3.48 $\pm$ 0.01	

BIBLIOGRAPHY

[1] Bogdan A. Dobrescu and Irina Mocioiu. Spin-dependent macroscopic forces from new particle exchange. *Journal of High Energy Physics*, 2006(11):005, 2006.

[2] Andrei D Sakharov. Violation of cp in variance, c asymmetry, and baryon asymmetry of the universe. *Soviet Physics Uspekhi*, 34(5):392, 1991.

[3] J. H. Christenson, J. W. Cronin, V. L. Fitch, and R. Turlay. Evidence for the 2π decay of the k_2^0 meson. *Phys. Rev. Lett.*, 13:138–140, Jul 1964.

[4] A. Alavi-Harati, I. F. Albuquerque, T. Alexopoulos, M. Arenton, K. Arisaka, S. Averitte, A. R. Barker, L. Bellantoni, A. Bellavance, J. Belz, R. Ben-David, D. R. Bergman, E. Blucher, G. J. Bock, C. Bown, S. Bright, E. Cheu, S. Childress, R. Coleman, M. D. Corcoran, G. Corti, B. Cox, M. B. Crisler, A. R. Erwin, R. Ford, A. Glazov, A. Golossanov, G. Graham, J. Graham, K. Hagan, E. Halkiadakis, K. Hanagaki, S. Hidaka, Y. B. Hsiung, V. Jejer, J. Jennings, D. A. Jensen, R. Kessler, H. G. Kobrak, J. Ladue, A. Lath, A. Ledovskoy, P. L. McBride, A. P. McManus, P. Mikelsons, E. Monnier, T. Nakaya, U. Nauenberg, K. S. Nelson, H. Nguyen, V. O'dell, M. Pang, R. Pordes, V. Prasad, C. Qiao, B. Quinn, E. J. Ramberg, R. E. Ray, A. Roodman, M. Sadamoto, S. Schnetzer, K. Senyo, P. Shanahan, P. S. Shawhan, W. Slater, N. Solomey, S. V. Somalwar, R. L. Stone, I. Suzuki, E. C. Swallow, R. A. Swanson, S. A. Taegar, R. J. Tesarek, G. B. Thomson, P. A. Toale, A. Tripathi, R. Tschirhart, Y. W. Wah, J. Wang, H. B. White, J. Whitmore, B. Winstein, R. Winston, J.-Y. Wu, T. Yamanaka, and E. D. Zimmerman. Observation of Direct CP Violation in $K_{S,L} \to \pi\pi$ Decays. *Physical Review Letters*, 83:22–27, July 1999.

[5] V. Fanti and S. Palestini. A new measurement of direct CP violation in two pion decays of the neutral kaon. *Physics Letters B*, 465:335–348, November 1999.

[6] B. Aubert, D. Boutigny, I. de Bonis, J.-M. Gaillard, A. Jeremie, Y. Karyotakis, J. P. Lees, P. Robbe, V. Tisserand, A. Palano, and et al. Measurement of CP-Violating Asymmetries in B^0 Decays to CP Eigenstates. *Physical Review Letters*, 86:2515, March 2001.

[7] K. Abe, K. Abe, R. Abe, I. Adachi, B. S. Ahn, H. Aihara, M. Akatsu, G. Alimonti, K. Asai, M. Asai, and et al. Observation of Large CP Violation in the Neutral B Meson System. *Physical Review Letters*, 87(9):091802, August 2001.

[8] A. Djouadi and G. Moreau. The couplings of the higgs boson and its cp properties from fits of the signal strengths and their ratios at the 7+8 tev lhc. *European Physical Journal C*, 73(9):1–12, 2013. cited By 13.

[9] Neil D. Christensen, Tao Han, and Yingchuan Li. Testing {CP} violation in {ZZH} interactions at the {LHC}. *Physics Letters B*, 693(1):28 – 35, 2010.

[10] M. Pepe Altarelli. CP violation in charm and beauty decays at LHCb. *Nuclear Physics B Proceedings Supplements*, 241:43–48, August 2013.

[11] M. D. Swallows, T. H. Loftus, W. C. Griffith, B. R. Heckel, E. N. Fortson, and M. V. Romalis. Techniques used to search for a permanent electric dipole moment of the ^{199}hg atom and the implications for *CP* violation. *Phys. Rev. A*, 87:012102, Jan 2013.

[12] C. A. Baker, D. D. Doyle, P. Geltenbort, K. Green, M. G. D. van der Grinten, P. G. Harris, P. Iaydjiev, S. N. Ivanov, D. J. R. May, J. M. Pendlebury, J. D. Richardson, D. Shiers, and K. F. Smith. Improved experimental limit on the electric dipole moment of the neutron. *Phys. Rev. Lett.*, 97:131801, Sep 2006.

[13] The ACME Collaboration, J. Baron, W. C. Campbell, D. DeMille, J. M. Doyle, G. Gabrielse, Y. V. Gurevich, P. W. Hess, N. R. Hutzler, E. Kirilov, I. Kozyryev, B. R. OLeary, C. D. Panda, M. F. Parsons, E. S. Petrik, B. Spaun, A. C. Vutha, and A. D. West. Order of magnitude smaller limit on the electric dipole moment of the electron. *Science*, 343(6168):269–272, 2014.

[14] Klaus Ehret, Maik Frede, Samvel Ghazaryan, Matthias Hildebrandt, Ernst-Axel Knabbe, Dietmar Kracht, Axel Lindner, Jenny List, Tobias Meier, Niels Meyer, Dieter Notz, Javier Redondo, Andreas Ringwald, Gnter Wiedemann, and Benno Willke. New {ALPS} results on hidden-sector lightweights. *Physics Letters B*, 689(45):149 – 155, 2010.

[15] A. Ringwald. Axions and Axion-Like Particles. July 2014.

[16] Paola Arias, Davide Cadamuro, Mark Goodsell, Joerg Jaeckel, Javier Redondo, et al. WISPy Cold Dark Matter. *JCAP*, 1206:013, 2012.

[17] R. Hammond. Spin, the classical theory. *Journal of Modern Physics*, 3(1):1–8, 2012.

[18] Richard T. Hammond. The necessity of torsion in gravity. *General Relativity and Gravitation*, 42(10):2345–2348, 2010.

[19] Friedrich W. Hehl, Paul von der Heyde, G. David Kerlick, and James M. Nester. General relativity with spin and torsion: Foundations and prospects. *Rev. Mod. Phys.*, 48:393–416, Jul 1976.

[20] M. Kalb and P. Ramond. Classical firect interstring action. *Physical Review*, 9:2273–2284, 1974.

[21] J. Scherk and J. H. Schwarz. Dual models and the ge-ometry of space-time. *Physics Letters*, B52:347–350, 1974.

[22] G. G. Raffelt. Axions - motivation, limits and searches. *Journal of Physics A Mathematical General*, 40:6607–6620, June 2007.

[23] H. Schlattl, A. Weiss, and G. Raffelt. Helioseismological constraint on solar axion emission. *Astroparticle Physics*, 10:353–359, May 1999.

[24] J. N. Bahcall, A. M. Serenelli, and S. Basu. New Solar Opacities, Abundances, Helioseismology, and Neutrino Fluxes. *The Astrophysical Journal Letters*, 621:L85–L88, March 2005.

[25] G. G. Raffelt, J. Redondo, and N. V. Maira. The meV mass frontier of axion physics. *Physical Review D*, 84(10):103008, November 2011.

[26] P. Jain and S. Mandal. Evading the astrophysical limits on light pseudoscalars. *International Journal of Modern Physics D*, 15(12):2095–2103, 2006.

[27] R. N. Mohapatra and S. Nasri. Reconciling the CAST and PVLAS Results. *Physical Review Letters*, 98(5):050402, February 2007.

[28] I. Antoniadis, A. Boyarsky, and O. Ruchayskiy. Axion alternatives. *ArXiv High Energy Physics - Phenomenology e-prints*, June 2006.

[29] E. Massó and J. Redondo. Compatibility of Cast Search with Axionlike Interpretation of PVLAS Results. *Physical Review Letters*, 97(15):151802, October 2006.

[30] E. Massó and J. Redondo. Evading astrophysical constraints on axion-like particles. *Journal of Cosmology and Astroparticle Physics*, 9:15, September 2005.

[31] Norman F. Ramsey. The tensor force between two protons at long range. *Physica A: Statistical Mechanics and its Applications*, 96(12):285 – 289, 1979.

[32] G. Vasilakis, J. M. Brown, T. W. Kornack, and M. V. Romalis. Limits on new long range nuclear spin-dependent forces set with a **K**-^{3}He comagnetometer. *Phys. Rev. Lett.*, 103:261801, Dec 2009.

[33] D. J. Wineland, J. J. Bollinger, D. J. Heinzen, W. M. Itano, and M. G. Raizen. Search for anomalous spin-dependent forces using stored-ion spectroscopy. *Phys. Rev. Lett.*, 67:1735–1738, Sep 1991.

[34] T. C. P. Chui and Wei-Tou Ni. Experimental search for an anomalous spin-spin interaction between electrons. *Phys. Rev. Lett.*, 71:3247–3250, Nov 1993.

[35] Michael G. Harris. *A Search for Macroscopic CP Violating Interactions, Using a Spin-Polarized Torsion Pendulum.* PhD thesis, University of Washington, 1998.

[36] C.D. Hoyle. *Sub-millimeter Tests of the Gravitational Inverse-Square Law.* PhD thesis, University of Washington, 2001.

[37] Claire E. Cramer. *A Torsion Balance Search for Spin-Coupled Forces.* PhD thesis, University of Washington, 2007.

[38] B. R. Heckel, E. G. Adelberger, C. E. Cramer, T. S. Cook, S. Schlamminger, and U. Schmidt. Preferred-frame and *cp*-violation tests with polarized electrons. *Phys. Rev. D*, 78:092006, Nov 2008.

[39] Ted S. Cook. *A test of the gravitational inverse-square law at short distance.* PhD thesis, University of Washington, 2013.

[40] Daniel J. Kapner. *A Short-Range Test of Newton's Gravitational Inverse-Square Law.* PhD thesis, University of Washington, 2005.

[41] Peter R. Saulson. Thermal noise in mechanical experiments. *Phys. Rev. D*, 42:2437–2445, Oct 1990.